UPPSALA
UNIVERSITET

Computational Studies of Electron Transport in Nanoscale Devices

HENRIK LÖFÅS

ACTA
UNIVERSITATIS
UPSALIENSIS
UPPSALA
2013

Dissertation presented at Uppsala University to be publicly examined in Häggsalen, Ångströmlaboratoriet, Lägerhyddsvägen 1, Uppsala, Friday, November 29, 2013 at 10:15 for the degree of Doctor of Philosophy. The examination will be conducted in English.

Abstract

Löfås, H. 2013. Computational Studies of Electron Transport in Nanoscale Devices. Acta Universitatis Upsaliensis. *Digital Comprehensive Summaries of Uppsala Dissertations from the Faculty of Science and Technology* 1090. i-x, 89 pp. Uppsala. ISBN 978-91-554-8781-2.

In this thesis, a combination of density functional theory (DFT) based calculations and nonequilibrium Green's functions are employed to investigate electron transport in molecular switches, molecular cords and nanoscale devices.

Molecular electronic devices have been proposed as an approach to complement today's silicon based electronic devices. However, engineering of such miniature devices and design of functional molecular components still present significant challenges.

First, the way to connect a molecule to conductive electrodes has to be controlled. We study, in a nanoelectrode-nanoparticle platform, how structural changes affect the measured conductance and how current fluctuations due to these structural changes can be decreased. We find that, for reproducible measurements, it is important to have the molecules chemically bonded to the surfaces of adjacent nanoparticles. Furthermore, we show by a combination of DFT and theoretical modeling that we can identify signals from single-molecules in inelastic electron spectroscopy measurements on these devices.

Second, active elements based on molecules, some examples being switches, rectifiers or memory devices, have to be designed. We study molecular conductance switches that can be operated by light and/or temperature. By tuning the substituents on the molecules, we can optimize the shift of the most conducting molecular orbital and increase the effective coupling between the molecule and the electrodes when going from the OFF to the ON-state of the switches, giving high switching ratio (up to three orders of magnitude). We also study so called mechanoswitches that are activated by a mechanical force elongating the molecules, which means that these switches could operate as sensors.

Furthermore, we have studied two different classes of compounds that may function either as rigid molecular spacers with a well-defined conductance or as molecular cords. In both cases, we find that it is of great importance to match the conjugation of the anchoring groups with the molecular backbone for high conductance.

The last part of the thesis is devoted to another interesting semiconductor material, diamond. We have accurately calculated the band structure and effective masses for this material. Furthermore, these results have been used to calculate the Hall coefficient, the resistivity and the Seebeck coefficient.

Keywords: Density functional theory, Molecular electronics, Organosilicon chemistry, Diamond, Molecular switches, Nanoelectrode bridge platform, Molecular cords

Henrik Löfås, Uppsala University, Department of Physics and Astronomy, Materials Theory, Box 516, SE-751 20 Uppsala, Sweden.

To my family

List of papers

This thesis is based on the following papers, which are referred to in the text by their Roman numerals.

I **Assessment of a nanoparticle bridge platform for molecular electronics measurements**
S. H. M. Jafri, T. Blom, K. Leifer, M. Strømme, H. Löfås, A. Grigoriev, R. Ahuja and K. Welch
Nanotechnology 21, 435204 (2010)

II **Realization of highly reproducible molecular junctions in a nanoparticle-alkanedithiol-nanoelectrode bridge platform**
S. H. M. Jafri, H. Löfås, T. Blom, A. Wallner, A. Grigoriev, R. Ahuja, H. Ottosson and K. Leifer
Manuscript

III **Identification of vibrational signatures from short chains of interlinked molecule-nanoparticle junctions obtained by inelastic electron tunnelling spectroscopy**
S. H. M. Jafri, H. Löfås, J. Fransson, T. Blom, A. Grigoriev, A. Wallner, R. Ahuja, H. Ottosson and K. Leifer
Nanoscale, 5, 4673-4677 (2013)

IV **New Class of Molecular Conductance Switches Based on the [1,3]-Silyl Migration from Silanes to Silenes**
H. Löfås, A. Orthaber, B. O. Jahn, A. M. Rouf, A. Grigoriev, S. Ott, R. Ahuja and H. Ottosson
J. Phys. Chem. C, 117 (21), 10909-10918 (2013)

V **Molecular Conductance Switches Exploiting Baird's Rule on Excited State Aromaticity and Antiaromaticity**
H. Löfås, R. Emanuelsson, R. Ahuja, A. Grigoriev and H. Ottosson
Manuscript

VI **Configuration and Conformation Dependent Electronic Coupling Variations of 1,4-Dialkynyl Substituted Cyclohexasilanes Allowing for Potential Single-Molecule Conductance Mechanoswitches**
R. Emanuelsson, H. Löfås, A. Wallner, D. Nauroozi, J. Baumgartner, C. Marschner, R. Ahuja, S. Ott, A. Grigoriev and H. Ottosson
Submitted

VII Conductance Through Carbosilane Cage Compounds: A Computational Investigation
H. Löfås, R. Emanuelsson, R. Ahuja, A. Grigoriev and H. Ottosson
J. Phys. Chem. C, (2013), DOI: 10.1021/jp407485n

VIII Towards Flexible Molecular Wires with Near Conformer-Independent Conjugation and Conductance
R. Emanuelsson, H. Löfås, J. Zhu, R. Ahuja, A. Grigoriev and H. Ottosson
Submitted

IX Effective masses and electronic structure of diamond including electron correlation effects in first principles calculations using the GW-approximation
H. Löfås, A. Grigoriev, J. Isberg and R. Ahuja
AIP Advances 1, 032139 (2011)

X Transport coefficients in diamond from *ab-initio* calculations
H. Löfås, A. Grigoriev, J. Isberg and R. Ahuja
Appl. Phys. Lett. 102, 092106 (2013)

Reprints were made with permission from the publishers.

Papers not included in the Thesis
- **Hybrid density functional study of electronic and optical properties of phase change memory material: $Ge_2Sb_2Te_5$**
  T. Kaewmaraya, M. Ramzan, H. Löfås and R. Ahuja
  J. Appl. Phys. 113, 033510 (2011)
- **Double-functionalized nanopore-embedded gold electrodes for rapid DNA sequencing**
  B. Pathak, H. Löfås, J. Prasongkit, A. Grigoriev, R. H. Scheicher and R. Ahuja
  Appl. Phys. Lett. 100, 023701 (2012)
- **Understanding Coupling Strengths and Level Alignments from Conductance Histograms**
  P. Berggren, H. Löfås, A. Grigoriev, R. Ahuja and J. Fransson
  Manuscript
- **Cooperative Gold Nanoparticle Stabilization by Acetylenic Phosphaalkenes**
  A. Orthaber, H. Löfås, E. Öberg, A. Grigoriev, A. Wallner, H. Jafri, M.-P. Santoni, R. Ahuja, K. Leifer, H. Ottosson and S. Ott
  Manuscript

Details of my contributions

In all included papers I have performed the transport calculations and analyzed the results. I have also done the implementation of the method for approximate conductance traces adjusted for the systems studied here. Furthermore, I have developed the analysis tool for plotting the local currents. I have been involved in the writing of all papers included, and for those where I am the first author I have had the main responsibility for the writing. For paper IV - X, I have also been involved in the design and coordination of the projects.

Contents

1. Introduction

Nanotechnology has become one of the fastest growing fields in science today. A nanometer (nm) is one thousand millionth of a meter, which can be compared with a red blood cell, which is 7000 nm wide, or a water molecule that is of the order 0.3 nm. Nanoscience is the study of phenomena and manipulations that occur on the atomic or molecular scale (from 0.1 nm up to 100 nm), where the properties often differ significantly from those on the macro scale. At the nanoscale, quantum effects can dominate, which is manifested in the optical, electrical and magnetic behavior of these systems.

During the last decade, electronic devices have undergone a rapid development becoming faster and smaller, the feature sizes have been reduced greatly and have reached the nanometer scale. The base of the integrated circuit is the silicon-based complementary metal-oxide-semiconductor (CMOS), with feature sizes as small as 22 nm (soon to be 14 nm) [1]. The shrinking of these devices has, so far, followed what is called Moore's law, which states that the transistor density on integrated chips will double every two years [2]. This prediction was made in 1965 [3] and has been correct, probably in large part, due to the fact that it now is used in the semiconductor industry as a roadmap for research and development [4]. The end of Moore's law has been predicted several times [5], but it is still valid and for the last 30 years it has been predicted that Moore's law would last at least another decade. Now, P. Gelsinger, who is leading the research at Intel, sees no limit and thinks it will hold until at least 2029. However, they can not rely simply on today's silicon CMOS devices, instead other types of structures and materials have to be incorporated [6]. Even if the prediction of the roadmap is possible only for the coming ten to fifteen years, sooner or later we will reach the end of today's CMOS devices, when sufficiently small feature sizes mean that the nanoscale quantum effects will introduce tunneling in the transistor making it unreliable.

To circumvent the difficulties in miniaturization of the CMOS some other ideas have been proposed, for example to replace some parts in the CMOS with molecules, or build complete electronic devices with molecules as the active elements [7]. This has emerged as what is now known as molecular electronics [8–12], where the idea is to build electronic components where the active element is provided by single-, or assemblies of, molecules that can act as switches, gate-operated transistors and wires. The first such device was a molecular rectifier proposed by Aviram and Ratner in 1974, where they showed a structure that could function as a rectifier and at the same time introduced a theoretical discussion of transport through single molecules [13].

The next big step came about a decade later when the scanning tunneling microscopy (STM) was developed at IBM, which turned out to be an important tool for measuring the conductance of molecules. However, the first actual measurement on single-molecule transport was done by Reed et al. in 1997, where they were able to measure the conductance (G) of benzene-1,4-dithiol (BDT) molecules in a mechanically controllable break junction (MCBJ) experiment [14].

Molecular electronics is an interdisciplinary field with its cornerstones in physics, chemistry and materials science which faces several challenges. For a physicist or a theoretician the main question is "how does current flow through molecules?". The method used in this thesis to describe electron transport through molecules is based on the non-equilibrium Green's functions techniques (NEGF), which is a more powerful and formally rigorous approach to studying quantum transport in nanosystems [15] compared to the first mesoscopic models proposed by Landauer, Büttiker, et al. [16]. A brief introduction to this theory together with an introduction to density functional theory (DFT) used to obtain the ground state electronic structure, and information about the implementation for computational purposes are all given in **Chapter 2**.

The challenge an experimentalist mostly faces is that measurements on single-molecules most often result in data with very large fluctuations. This is due to the fact that the local contact geometries in a nanoscale junction are never identical, and that it is very difficult to control the interface between the molecules and the electrodes. There are several methods that can be used for measurements on single-molecules [17], *e.g.*, STM and MCBJ, and most methods produce large sets of data. A statistical analysis encompassing these large datasets is necessary to find the conductance as an average over all the different local geometries. A drawback with many of these methods is that they need to be undertaken in a laboratory environment, in **Chapter 3** we study fluctuations and how to decrease them in a nanoparticle bridge molecular junction, which can be used for single-molecule measurements and is easily transported.

And finally from the view of a synthetic chemist, the challenge lie first in designing the central core of the molecule to show the desired characteristics, and second the sometime greater challenge of attaching substituents to the core that bind effectively to electrodes. For electrodes, noble metals such as gold are preferred, where mostly thiol (-SH) or amino ($-NH_2$) groups are used as anchoring groups. Herein we also propose that the silyl-group ($-SiH_3$) may show potential as an anchoring group for certain classes of compounds. Furthermore, in **Chapter 4** and **Chapter 5**, from a synthetic point of view we design and study a set of molecular conductance switches, molecular wires and rigid molecular spacers.

In standard electronics the bits are carried by the electron charge. Moving a charge requires energy, hence causes Joule heating in the material and also sets the fundamental limit for the switching rate. Instead of the charge of the

electron it is possible to utilize other properties to transfer information. One well studied field is "spintronics" [18, 19] where the spin of the electron is used to carry information. An alternative and novel concept proposed is to use the wave quantum number of an electron in a crystalline material. For example it is possible to use the valley degree of freedom in diamond to enable valleytronic information processing. This may lead to ultrafast computing with less power consumption [20, 21]. For this purpose accurate knowledge about the electronic structure, the effective masses of the charge carriers, as well as the transport properties are important, and we study these properties of diamond in **Chapter 6**.

To summarize, the interest in using molecular structures in nanoscale electronic devices is based on four major advantages [8] over silicon based devices:

- *Size*. Molecular structures are in the range between 1 and 100 nm. Smaller comes with lower cost (identical molecules can easily be produced in huge numbers), higher efficiency (only few electrons needed to transport a signal) and lower power dissipation (ultra-dense devices possible with molecules as active elements).
- *Assembly and recognition*. Molecules self-assemble to form regular structures that can be used to build devices. Molecular recognition can be used to modify electronic behavior on the single-molecule scale, creating both molecular switches and sensors.
- *Dynamical stereochemistry*. Many molecules have multiple stable structures or isomers, which can have distinct different electronic and optical properties for possible use as switching devices.
- *Synthetic tailorability*. Chemical synthesis is a highly developed field and it is possible to engineer organic molecules with specific electronic properties changing the transport or optical characteristics of the molecule.

To be sure, there are also drawbacks, including instability at higher temperatures, noise due to low current density and slow switching speeds due to low transmission probabilities through contacts. But overall, the advantages could pave the way for molecules as active elements in future electronic applications.

2. Theoretical framework

In this chapter, a brief overview of the theoretical framework used in this thesis is given. This work is based on density functional theory (DFT). The electronic structure of an atomic system is described from first principles (*ab initio*), that means without parameters derived from experiments. In the first part of this chapter, an overview of the main theorems starting from the many-body problem will be given.

In the following section, a brief overview of important aspects of implementation of DFT for the atomic-scale simulations is given, as employed for the electronic structure calculations in this thesis.

In the last part of the chapter, theory describing electron transport through a scattering region is introduced. This is based on nonequilibrium Green's functions (NEGF) theory and the description of both the elastic and inelastic current is introduced.

2.1 The many body problem

To describe a material we need to understand how a great number of atoms interact with each other, hence we are dealing with a many body problem. The properties we are interested in can be determined from the Schrödinger equation

$$\hat{H}\Psi = E\Psi, \tag{2.1}$$

where the Hamiltonian, $\hat{H}$, describing the system is

$$
\begin{aligned}
\hat{H} =\ & -\frac{\hbar^2}{2}\sum_k^{N_{nucl}}\frac{\nabla^2}{M_k} - \frac{\hbar^2}{2}\sum_i^{N_{el}}\frac{\nabla^2}{m_e} \\
& + \frac{1}{2}\sum_{k\neq l}^{N_{nucl}}\frac{Z_k Z_l e^2}{|\boldsymbol{R}_k - \boldsymbol{R}_l|} + \frac{1}{2}\sum_{i\neq j}^{N_{el}}\frac{e^2}{|\boldsymbol{r}_i - \boldsymbol{r}_j|} - \sum_{i,k}^{N_{el},N_{nucl}}\frac{Z_k e^2}{|\boldsymbol{r}_i - \boldsymbol{R}_k|}.
\end{aligned}
\tag{2.2}
$$

The first two terms are the kinetic operators for the nuclei and electrons. The three terms on the second row describe the interaction between nuclear-nuclear, electron-electron and nuclear-electron respectively. This problem is extremely difficult to solve, and can only be solved exactly in the simplest case, the hydrogen atom. For more complicated systems, such as solids where a large number of particles are considered, approximations have to be made.

2.1.1 Born-Oppenheimer approximation

The first approximation made to solve the problem is the Born-Oppenheimer (BO)-approximation [22], where the motion of the electrons is separated from the nuclei. This can be made since the masses of the nuclei are much greater than the mass of the electrons, hence the nuclei can be considered to be static at their equilibrium position and interact with the electrons via an external potential, V_{ext}. The electronic Hamiltonian can now be written as

$$\hat{H} = -\frac{\hbar^2}{2} \sum_i^{N_{el}} \frac{\nabla^2}{m_e} + \frac{1}{2} \sum_{i \neq j}^{N_{el}} \frac{e^2}{|\boldsymbol{r}_i - \boldsymbol{r}_j|} + \hat{V}_{ext}. \tag{2.3}$$

In the potential $\hat{V}_{ext}$, other external effects such as electromagnetic fields can also be included. Even if the Hamiltonian is simplified now, the electron-electron interaction is still there, which makes the problem still too complicated to solve. One approach to handle this is with DFT, which will be considered in following section.

2.2 Density functional theory

The basic idea of DFT is to replace the more complicated many-body problem described in Eq. 2.2 and Eq. 2.3 with another system that is more easily solved. DFT is an exact theory, but in practice, since the exact functional describing the interactions between electrons in the system is not known, some approximations to the Hamiltonian have to be made. The main foundation of DFT are the Hohenberg-Kohn theorems [23, 24], which state

Theorem 2.2.1 *If two systems of electrons have the same ground state density $\rho(\boldsymbol{r})$ while one is trapped in the potential $V(\boldsymbol{r})$ and the other in potential $V'(\boldsymbol{r})$ then,*

$$V'(\boldsymbol{r}) - V(\boldsymbol{r}) \equiv \text{const} \tag{2.4}$$

This implies since $V(\boldsymbol{r})$ is a unique functional of $\rho(\boldsymbol{r})$ (up to a constant), and $V(\boldsymbol{r})$ fixes H (Eq. 2.3), the many-particle ground state is a unique functional of the density $\rho(\boldsymbol{r})$.

Since the wave-function Ψ is a functional of the density, $\rho(\boldsymbol{r})$, it is possible to define a universal functional $F[\rho]$ valid for any number of particles and any external potential. With this functional, it is possible to define the energy functional for the system as

$$E[\rho(\boldsymbol{r})] \equiv \int V(\boldsymbol{r})\rho(\boldsymbol{r})d\boldsymbol{r} + F[\rho(\boldsymbol{r})] \tag{2.5}$$

and show that

Theorem 2.2.2 *The global minimum of the energy functional (Eq. 2.5) is the true ground-state energy, E_0, for the system and the density that minimizes the functional is the ground-state density, $\rho_0(\boldsymbol{r})$*

This implies that if we knew $F[\rho]$ and it was a sufficiently simple functional of ρ, it would be an easy task to determine the ground-state density and energy of the system for a given external potential. However, for the majority of problems the universal functional is not known and has to be approximated in some way. Still, the two theorems show the strength of DFT, mapping the many-body problem to the electron density.

To further simplify the problem, a first approximation was proposed by Kohn and Sham [24] where they assumed that instead of the interacting electrons we have a system of non-interacting electrons moving in an effective potential. Thus, reducing the many-body problem to a single-particle problem of electrons described by the Kohn-Sham equations,

$$H\Phi_j(\boldsymbol{r}) = \varepsilon_j\Phi_j(\boldsymbol{r}) \tag{2.6}$$

with $\Phi_j(\boldsymbol{r})$ as the Kohn-Sham (KS)-wavefunction with the eigenvalue ε_j and where the Hamiltonian for the system is

$$H = -\frac{\nabla_i^2}{2} + V_{\text{eff}}(\boldsymbol{r}) \tag{2.7}$$

and

$$V_{\text{eff}}(\boldsymbol{r}) = V_{\text{ext}} + \int \frac{\rho(\boldsymbol{r}')}{|\boldsymbol{r}-\boldsymbol{r}'|} d\boldsymbol{r} + \frac{\delta E_{xc}[\rho(\boldsymbol{r})]}{\delta\rho(\boldsymbol{r})}. \tag{2.8}$$

The effective potential is described by three terms, first the external potential that includes the interaction between the ion cores and the valence electrons, and the second term is the Coulomb potential. The third term, the exchange-correlation functional, is the most complicated and can not be evaluated exactly but has to be approximated in some way.

The Kohn-Sham wavefunctions in Eq. 2.6 are not the true wavefunctions for the system, but they can be used to calculate the electron density as

$$\rho(\boldsymbol{r}) = \sum |\Phi_i(\boldsymbol{r})|^2 \tag{2.9}$$

To obtain the ground-state density, the Kohn-Sham equations can be solved iteratively until self-consistency (difference between input and output density less than some convergence criteria) is reached as follows

1. Make an initial guess of the electron density $\rho(\mathbf{r})$.
2. Construct the effective potential from Eq. 2.8
3. Solve Eq. 2.6 to obtain the KS-wavefunctions $\Phi_j(\mathbf{r})$
4. Calculate the density according to 2.9
5. Compare the input density and the new density obtained in the previous step, if the difference is less than the convergence criteria the problem of finding the ground-state density is solved. Otherwise use the new density as input to step 1 and iterate until convergence.

2.2.1 Exchange-correlation functionals

To be able to solve the Kohn-Sham equations in the previous section, we have to specify some expression for the exchange-correlation functional $E[\rho(\mathbf{r})]$. But since the exact form of this functional is unknown, it is necessary to find an approximate form. In the original work of Kohn and Sham [24], they introduced an expression for the functional which has later been called the local density approximation (LDA).

$$E_{xc}[\rho] = \int \rho(\mathbf{r})\varepsilon_{xc}(\rho(\mathbf{r}))d\mathbf{r}, \tag{2.10}$$

where $\varepsilon_{xc}(\rho)$ is the exchange-correlation energy per electron of a uniform electron gas of density $\rho(\mathbf{r})$, which is known from the theories of the homogenous electron gas. It can be shown that this functional is more or less exact in two limiting cases:

(a) **Slowly varying density** In this limit, the condition $r_s/r_0 \ll 1$ holds, where r_s is the Wigner-Seitz radius and r_0 is the length scale of the density variation. It is possible to show that the above expression (2.10) is then exact if terms of $|\nabla|^2$ and higher order in the energy are neglected, giving the density with even higher accuracy with errors of the order $|\nabla|^4$.

(b) **High density** This limit is characterized by the condition $r_s/a_0 \ll 1$, where a_0 is the Bohr radius. This implies that energy from exchange and correlation effects is significantly smaller (by a factor of r_s/a_0) than the kinetic energy of the electrons, hence the inaccuracy in the exchange-correlation energy is negligible.

Correspondingly, atoms and molecules can be divided into three regions. Firstly, we have the region close to the atomic nuclei, where the electronic density will be high, hence LDA should be acceptable from (b). Secondly, far away from the nucleus the electronic density can be expected to vary slowly, and LDA should perform well according to (a). Thirdly, we have the interstitial region between atoms in molecules and solids. Here LDA can not be expected

to work and this should be the main source of errors in the calculations using LDA, hence the description of chemical bonding should not be accurate. Supringsly, LDA works very well for solids, even for solids with properties far from the homogenous electron gas, but in most cases the binding energy is overestimated.

There have been many attempts after the first LDA functional to develop something better. Maybe the most well-known and well-used of these is the generalized gradient approximation (GGA), where the exchange-correlation energy per atom ε_{xc} is not just calculated from the density but also the gradient of the density, $\nabla\rho(r)$. There exist many forms of this functional, probably the Perdew-Wang (PW92) [25] and Perdew-Burke-Ernzerhof (PBE) [26] are the most widely used. There is no general result as to which of the functionals is most accurate, instead they have to be evaluated from problem to problem and compared with experiments. Still, it is known that GGA always gives a smaller exchange-correlation energy, hence it decreases the binding energy and corrects the LDA over-binding. This often improves the agreement with experiments, but can also lead to under-binding.

In this thesis, both GGA and LDA have been used, and when investigating transport the choice between the functionals should not be as important as dealing with the structure, since the difference between the functionals will be small compared to approximations in the transport calculations.

2.3 Computational methods

In order to use DFT for numerical calculations, many technical details and further approximations have to be made. In this work, the SIESTA (Spanish Initiative for Electronic Simulations with Thousands of Atoms) and Abinit codes will be used, some of the main aspects of the implementation of DFT in SIESTA are briefly described below, a full description of the codes are available in Refs. [27, 28] (SIESTA), Refs. [29, 30] (Abinit) and references therein. The main difference between the two codes are that in SIESTA the valence electrons are expanded in basis sets of local orbitals, making it suitable for transport calculations while Abinit uses a plane-wave basis set, thus making it more suitable for calculations of periodic crystals.

2.3.1 Pseudopotentials

To make the calculations computationally inexpensive it is possible to replace the effect of the the motion of the core electrons of an atom and its nucleus with some effective potential. The pseudopotential is an effective potential used to describe the chemically inert core, while the valence states active in chemical bonding are treated explicitly[31]. This is possible since the core-electron

wave function of an atom remains almost unchanged in different chemical environments, and the major role of the core-electron wave functions in chemical bonding is to constrain the valence states to be orthogonal to the core states. With just this constraint, the possibilities to generate a pseudopotential are infinite, therefore there has been a lot of work to find a way to generate suitable pseudopotentials that both reproduce the all-electron behavior and at the same time are computationally efficient.

The pseudopotentials used in these calculations are generated from all-electron atomic calculations, which is done in DFT by solving the radial Kohn-Sham equation [24]

$$\left(\frac{-1}{2}\frac{d^2}{dr^2} + \frac{l(l+1)}{2r^2} + V[\rho;r]\right)rR_{nl}(r) = \varepsilon_{nl}R_{nl}(r) \qquad (2.11)$$

where $V[\rho;r]$ is the self-consistent one-electron potential

$$V[\rho;r] = \frac{-Z}{r} + V_H[\rho;r] + V_{xc}^{func}(\rho(r)), \qquad (2.12)$$

where $\rho(r)$ is the sum of electron densities for the occupied wavefunctions $R_{nl}(r)$, $V_H[\rho;r]$ is the Hartree potential and $V_{xc}^{func}(\rho(r)$ is the exchange-correlation potential for the used functional (func=GGA,LDA). Further, the pseudopotentials are constructed to satisfy four general conditions:

- The pseudo-wave-functions generated from the pseudopotential should contain no nodes.
- The normalized atomic radial pseudo-wave-function (PP), with angular momentum l, is equal to the normalized radial all-electron wave-function (AE) beyond a chosen cutoff radius r_{cl},

$$R_l^{PP}(r) = R_l^{AE}(r) \qquad \text{for} \qquad r > r_{rcl}. \qquad (2.13)$$

- The charge inside the cutoff-radius must be the same for the two wave-functions (PP and AE)

$$\int_0^{r_{cl}} |R_l^{PP}(r)|^2 r^2 dr = \int_0^{r_{cl}} |R_l^{AE}(r)|^2 r^2 dr. \qquad (2.14)$$

- The AE and PP eigenvalues should be equal

$$\varepsilon_l^{PP} = \varepsilon_l^{AE}. \qquad (2.15)$$

The pseudopotentials constructed and fulfilling these criterias are usually referred to as "norm-conserving pseudopotentials"[32] and it is this type that are commonly used in SIESTA calculations. These pseudopotentials can be constructed in several ways, in SIESTA usually the parametrization by Troullier and Martin [31] is used, where the semilocal form of the pseudopotential is transformed to the fully nonlocal form by the method of Kleinman and Bylander [33].

2.3.2 Basis set

In the SIESTA method, the valence electrons are described by a basis set consisting of linear combination of localized numerical atomic orbitals (LCAO). This means that the basis functions are composed of a spherical harmonic and a radial function

$$\Phi_{lmn}(r,\theta,\varphi) = R_{n,l}(r)Y_{l,m}(\theta,\varphi), \qquad (2.16)$$

where $R_{n,l}$ and $Y_{l,m}$ are the radial functions for orbital n and the real spherical harmonic for orbital angular momentum l and magnetic quantum number m, respectively. The use of a localized basis set has an advantage over the more commonly used plane-wave basis sets, especially when dealing with transport in open quantum systems due, to the finite radius, r_c, of the basis orbitals, making them strictly zero beyond this radius. Further, the shape and size of the basis set must be chosen and there is a lot of freedom in how to build them. This includes the center (not necessarily atom centered), how many angular momentum channels around each center, how many radial functions per angular momentum channel and last, the cut-off, r_c, and shape for each radial function. These parameters should be chosen wisely to optimize efficiency and accuracy. There are methods to obtain optimized basis sets variationally [34], but there is still no systematic way to obtain "the optimal" basis set and check the convergence. SIESTA comes with some preset algorithms and criteria defining basis sets automatically [35].

In SIESTA, the nomenclature of the basis sets follows the quantum chemistry (QC) standards, ranging from basis sets of single ζ (SZ) type to multiple ζ including polarization and diffuse orbitals, giving results from fast calculations with poor convergence to highly converged and more computationally demanding calculations. The minimal basis set is the SZ which has one radial function per angular momentum channel, the number of angular functions are determined by electronic population of the valence states in the free atom. To obtain flexibility in the radial part, it is possible to add one more radial function to get a double-ζ (DZ) basis. In SIESTA, this is done in a similar fashion as the split-valence scheme in QC, but with a modification to make sure that the finite range of the basis is kept [36], where the new radial function is equal to the first one outside a matching radius, only changing the part close to the core. In this fashion, it is also easy to extend to even more radial functions and obtain a multiple-ζ basis. To introduce more flexibility in the angular part, polarization orbitals can be added. The first choice for this would be to use the first unoccupied orbital of the free atom, but it has been found that this is not a good choice since they are generally too extended. Instead, another route has been found where a small electric field is used to polarize the atom resulting in the (l+1) orbital.

The methods described here have been thoroughly tested and the results have shown that for structural and energetic properties most often a DZ plus

one polarization orbital (DZP) basis set gives results within the accuracy of the LDA and GGA approximation.

2.4 Nuclear vibrations

If we now have solved Eq. 2.1 within the BO-approximation, we know the energy-eigenvalues for our system and have something called the Born-Oppenheimer total energy surface $E(\boldsymbol{R})$. From this, it is possible to investigate the vibrational modes in the system, i.e phonons [37], via the forces. If the system is in the equilibrium geometry ($\boldsymbol{R}_0$) all forces on the nuclei should be zero

$$\boldsymbol{F}(\boldsymbol{R}_0) = - \left. \frac{\partial E_0(\boldsymbol{R})}{\partial \boldsymbol{R}_I} \right|_{\boldsymbol{R}=\boldsymbol{R}_0} = 0. \tag{2.17}$$

If a small perturbation is introduced as a displacement away from the equilibrium geometry, the matrix of interatomic force constants called the Hessian matrix is obtained

$$C_{I\nu;J\mu} \equiv \left. \frac{\partial^2 E_0(\boldsymbol{R})}{\partial R_{I\nu} \partial R_{J\mu}} \right|_{\boldsymbol{R}=\boldsymbol{R}_0}, \tag{2.18}$$

where μ, ν represent the different spatial directions. Assuming a harmonic displacement of the coordinates and using Newtons's second law of motion the eigenvalue problem

$$(\omega^2 \mathbf{1} - \mathbf{W})\mathbf{v} = 0 \tag{2.19}$$

is obtained where $\mathbf{W}$ is the mass-scaled matrix of interatomic force constants

$$W_{I\nu;J\mu} \equiv \frac{C_{\nu;J\mu}}{\sqrt{M_I M_J}}. \tag{2.20}$$

The solution of Eq. 2.19 gives the vibrational frequency ω_λ and vibrational mode vector $\mathbf{v}^\lambda$ for our system.

The nuclear forces $\boldsymbol{F}_I$ are readily available during the solution of the DFT-problem and when the SIESTA package is used they are a direct output. These can then be used to approximate the Hessian matrix via finite differences in what is called the "frozen phonons method", more on how this can be done and the implications can be found in [27, 38].

2.5 Quantum transport in the non-equilibrium Green's functions formalism (NEGF)

In this section, the basic equations describing the stationary electron transport through a region in space in the NEGF formalism are given.

So far in the previous sections, we dealt with the DFT-method for electronic structure, the strength of DFT is that it can, from first-principles, describe a wide range of materials without material-dependent parameters. Still, if we want to consider electron transport, we need to go beyond DFT due to its restrictions; firstly, it can only treat small, finite or periodic systems; and secondly, the system has to be in its equilibrium ground state. Here, when an atomic or molecular system is connected to bulk electrodes we need to be able to treat infinite and non-periodic systems. Further, to drive a current through this system, a bias voltage needs to be added to the electrodes, hence the molecular system will no longer be in thermal equilibrium and we must be able to treat this non-equilibrium system.

The starting point when using the NEGF approach is the partition of the system into a central coupling region (which can include interactions) and two noninteracting electrodes, a sketch of the system is given in Fig. 2.1. In the following, we assume that the system, as in the case of DFT, can be described by a single-particle mean-field Hamiltonian describing electrons moving in a static potential from the frozen atomic nuclei. For simplicity, the presentation will be given for spin-independent problems, but the generalization to include spin-polarization is straightforward.

2.5.1 System setup
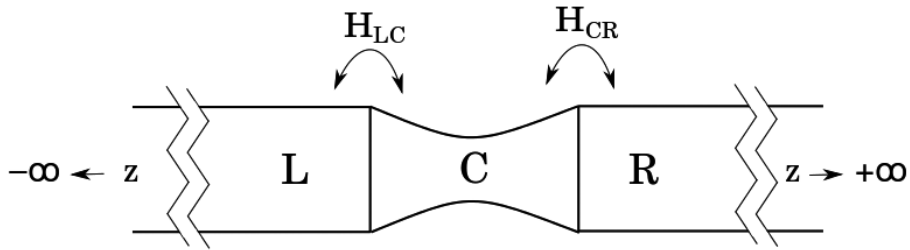
Figure 2.1. We model the contact C region coupled to two semi-infinite left L and right R electrodes. The direction of transport is denoted by z. There is no direct coupling between the two electrodes

The physical system we are interested in is sketched in Fig. 2.1, consisting of two semi-infinite electrodes coupled via a contact region. Since we are working in a framework of a localized basis set, the finite range of the orbitals implies that all matrix elements of the Hamiltonian or overlap integrals between atoms situated on the two different electrodes are zero, hence the only coupling between the left and the right electrode is via the contact region (provided that the contact region is large enough). The electronic Hamiltonian

$\mathbf{H} \equiv \{\{H_{ij}\}\}$ and overlap matrix $\mathbf{S} \equiv \{\{S_{ij}\}\}$ can thus be written as

$$\mathbf{H} = \begin{pmatrix} \boldsymbol{H}_L & \boldsymbol{H}_{LC} & 0 \\ \boldsymbol{H}_{CL} & \boldsymbol{H}_C & \boldsymbol{H}_{CR} \\ 0 & \boldsymbol{H}_{RC} & \boldsymbol{H}_R \end{pmatrix} \tag{2.21}$$

$$\mathbf{S} = \begin{pmatrix} \boldsymbol{S}_L & \boldsymbol{S}_{LC} & 0 \\ \boldsymbol{S}_{CL} & \boldsymbol{S}_C & \boldsymbol{S}_{CR} \\ 0 & \boldsymbol{S}_{RC} & \boldsymbol{S}_R \end{pmatrix}. \tag{2.22}$$

Further, it is assumed that the Hamiltonian is converged to the bulk values in the L- and R-regions, corresponding to the left and right electrodes. Thus it is only necessary to calculate the Hamiltonian and overlap matrices in the C, C-L and C-R regions.

The transport properties can thus be described by the finite L-C-R region of the infinite system, via a series of Green's function matrices. The retarded electronic single-particle Green's function $\boldsymbol{G}^r(\varepsilon)$ describing the infinite system can be defined as the inverse of $[(\varepsilon + i\eta)\boldsymbol{S} - \boldsymbol{H}]$ where $\eta = 0^+$[39]. For the contact region (C) this will then yield the retarded Green's function

$$\boldsymbol{G}_C^r(\varepsilon) = [(\varepsilon + i\eta)\boldsymbol{S}_C - \boldsymbol{H}_C - \boldsymbol{\Sigma}_L^r(\varepsilon) - \boldsymbol{\Sigma}_R^r(\varepsilon)]^{-1} \tag{2.23}$$

where the self-energy due to the coupling to the left lead is $\boldsymbol{\Sigma}_L^r(\varepsilon) = (\boldsymbol{H}_{CL} - \varepsilon\boldsymbol{S}_{CL})\boldsymbol{g}_L^r(\varepsilon)(\boldsymbol{H}_{LC} - \varepsilon\boldsymbol{S}_{LC})$ and similarly for the right lead. The $\boldsymbol{g}_\alpha^r(\varepsilon)$ is the retarded surface Green's function of the $\alpha = L, R$ lead.

2.5.2 Elastic transport

In the following section, we will consider a two-terminal setup without interactions in the central region (C), for this situation the current through this region can be described by a Landauer-Büttiker like formula[16]

$$I(V) = G_0 \int_{-\infty}^{\infty} d\varepsilon \left[n_F(\varepsilon - \mu_L) - n_F(\varepsilon - \mu_R) \right]$$
$$\times \text{Tr} \left[\boldsymbol{\Gamma}_L(\varepsilon) \boldsymbol{G}_C^r(\varepsilon) \boldsymbol{\Gamma}_R(\varepsilon) \boldsymbol{G}_C^a(\varepsilon) \right] \tag{2.24}$$

where $G_0 = 2e^2/h$, $n_F = 1([exp(\varepsilon/k_BT) + 1]$ is the Fermi-Dirac distribution, μ_α the chemical potential of lead α, and

$$\boldsymbol{\Gamma}_\alpha(\varepsilon) \equiv i \left[\boldsymbol{\Sigma}_\alpha^r(\varepsilon) - \boldsymbol{\Sigma}_\alpha^a(\varepsilon) \right] \tag{2.25}$$

describes the broadening of the states in the central region by the coupling to the electrodes. This expression can be derived from the fluctuation-dissipation theorem[16]. The expression for the current is not general but only valid for a mean-field theory like the KS-DFT, furthermore since we are dealing with

steady-state transport the advanced and retarded Green's function can be related via time-reversal symmetry as $G_C^a(\varepsilon) = G_C^r(\varepsilon)^\dagger$. Thus, from Eq. (2.24) the expression for the transmission T can be identified.

$$T(\varepsilon) = \text{Tr}\left[\mathbf{\Gamma}_L(\varepsilon)G_C^r(\varepsilon)\mathbf{\Gamma}_R(\varepsilon)G_C^a(\varepsilon)\right] \qquad (2.26)$$

2.5.3 Inelastic transport due to electron-phonon interaction

To investigate inelastic effects in the junction, excitations of phonons have to be taken in account. This can be done by the mass scaled dynamic matrix $\mathbf{W}$ (Eq. 2.20), and since interatomic forces are short ranged, it can be partitioned in the same way as $\mathbf{H}$ and $\mathbf{S}$.

$$\mathbf{W} = \begin{pmatrix} \mathbf{W}_L & \mathbf{W}_{LC} & 0 \\ \mathbf{W}_{CL} & \mathbf{W}_C & \mathbf{W}_{CR} \\ 0 & \mathbf{W}_{RC} & \mathbf{W}_R \end{pmatrix} \qquad (2.27)$$

In the same way as we defined the electronic Green's function (Eq. 2.23) earlier, we can now define the retarded phonon Green's function $\mathbf{D}^r(\omega)$ as the inverse of $[(\omega + i\eta)^2\mathbf{1} - \mathbf{W}]$, for the contact region this gives

$$\mathbf{D}_C^r(\omega) = [(\omega + i\eta)^2\mathbf{1} - \mathbf{W}_C - \Pi_L^r(\omega) - \Pi_R^r(\omega)]^{-1} \qquad (2.28)$$

where $\Pi_{R(L)}^r(\omega)$ are the phonon self-energies due to the coupling to right (left) regions. Since we are only interested in interactions between the electronic current and vibrations localized in the central region, to a first approximation, it is possible to disregard the phonon self-energies[38] resulting in

$$\mathbf{D}_C^r(\omega) \approx [(\omega + i\eta)^2\mathbf{1} - \mathbf{W}_C]^{-1} \qquad (2.29)$$

Lowest order expansion of the current

To fully take into account the electron-phonon interactions when calculating the current is a very daunting task, where the full Green's functions $G_C^{\gtrless}(\varepsilon)$ including all relevant interactions are needed[38, 40, 41]. Even if this can be done, for systems with a weak electron-phonon coupling and where the density of states varies slowly with energy (which is the cases considered in this thesis) another approximation can also be made, called the lowest order expansion (LOE) of the current, for the applicability of LOE see [40, 42]

The assumptions of LOE is that the retarded(advanced) single-particle Green's functions $G_C^{r(a)}$ and lead self-energies $\Sigma_\alpha^{r(a)}$ are energy independent. Thus expanding the current to second order in the electron-phonon couplings $\mathbf{M}^\lambda$[38], the energy integrals can be done analytically, still preserving the Pauli exclusion principle for fermonic particles necessary for blocking of phonon emission processes at low bias.

The current in LOE approximation can be written as[38, 43]

$$I^{LOE} = G_0 V \text{Tr}[\boldsymbol{G}\boldsymbol{\Gamma}_R\boldsymbol{G}^\dagger\boldsymbol{\Gamma}_L]$$

$$+ \sum_\lambda \mathscr{I}_\lambda^{sym}(V,T,\langle n_\lambda\rangle)\text{Tr}\left[\boldsymbol{G}^\dagger\boldsymbol{\Gamma}_L\boldsymbol{G}\left(\boldsymbol{M}^\lambda\boldsymbol{A}_R\boldsymbol{M}^\lambda + \frac{i}{2}(\boldsymbol{\Gamma}_R\boldsymbol{G}^\dagger\boldsymbol{M}^\lambda\boldsymbol{A}\boldsymbol{M}^\lambda - H.C)\right)\right]$$

$$+ \sum_\lambda \mathscr{I}_\lambda^{asym}(V,T)\text{Tr}\left[\boldsymbol{G}^\dagger\boldsymbol{\Gamma}_L\boldsymbol{G}\left(\boldsymbol{\Gamma}_R\boldsymbol{G}^\dagger\boldsymbol{M}^\lambda(\boldsymbol{A}_R-\boldsymbol{A}_L)\boldsymbol{M}^\lambda + H.C\right)\right],$$

$$(2.30)$$

$$\mathscr{I}_\lambda^{sym} = \frac{e}{\pi\hbar}\left(2eV\langle n_\lambda\rangle + \frac{\hbar\omega_\lambda - eV}{e^{(\hbar\omega_\lambda - eV)/k_B T} - 1} - \frac{\hbar\omega_\lambda + eV}{e^{(\hbar\omega_\lambda + eV)/k_B T} - 1}\right), \quad (2.31)$$

$$\mathscr{I}_\lambda^{asym} = \frac{e}{\hbar}\int_{-\infty}^\infty \frac{d\varepsilon}{2\pi}[n_F(\varepsilon) - n_F(\varepsilon - eV)]\mathscr{H}_{\varepsilon'}\left(n_F(\varepsilon' + \hbar\omega_\lambda) - n_F(\varepsilon' - \hbar\omega_\lambda)\right)(\varepsilon)$$

$$(2.32)$$

where $eV = \mu_R - \mu_L$ is the bias, $\mathscr{H}$ the Hilbert transform and $\langle n_\lambda\rangle$ the expectation value of the occupation of phonon mode λ. Here $\boldsymbol{G} = \boldsymbol{G}_C^r(\varepsilon_F)$ is the retarded Green's function and $\boldsymbol{A} = i(\boldsymbol{G} - \boldsymbol{G}^\dagger)$ the spectral function, which, together with the electrode couplings $\boldsymbol{\Gamma}_{L,R} = \boldsymbol{\Gamma}_{L,R}(\varepsilon_F)$, are evaluated at the Fermi energy.

The current in the LOE representation contains three main parts, first is the Landauer-Büttiker term (cf. Eq. 2.24) for elastic conductance, secondly there is a "symmetric" term that gives symmetric conductance steps at vibrational energies, third and last is the "asymmetric" term which gives peaks and dips in the conductance that are asymmetric with respect to voltage inversion. Often the asymmetric contribution is small compared with the symmetric, and for symmetric junctions it can be shown that the asymmetric contribution is strictly zero. The symmetric term is also responsible for the sign of the conductance change, and the rule of thumb is that it gives a conduction increase for low conducting systems (and a decrease for high conducting systems), hence phonons help electrons tunnel through not so well conducting molecules and introduce scattering centers in metallic wires with close to ballistic conduction. A more comprehensive discussion of these features can be found in [43–45]

2.6 Method for approximate conductance traces

The conductance of organic molecules at ambient temperature is believed to be a subtle and highly dynamic process which requires information about several molecular conformations [46–53], but so far in standard DFT-NEGF based methods, this dynamical behavior is not included. Here we show a method where these effects can be included in a first-principle way. Several methods exist where geometries obtained from classical or ab initio molecular dynamics (MD) are used as input to simple transport models (e.g. tight-binding
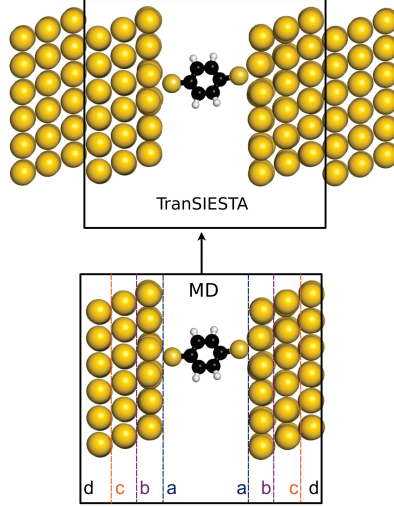
Figure 2.2. Schematic picture of how the combination of the MD and TS calculations are performed. Hamiltonian $\boldsymbol{H}_l$ and overlap $\boldsymbol{S}_l$ are copied as indicated in the lower part of the figure (where a-d symbolizes different sub-regions), and pasted into corresponding $\hat{\boldsymbol{H}}_m$ and overlap $\hat{\boldsymbol{S}}_m$ obtained from the TS calculations.

(TB)), to calculate transport for realistic situations. This method goes one step further, and to our knowledge is the first, where the Hamiltonian- and overlap-matrices obtained from the MD-simulations are used as input to *ab initio* DFT-NEGF transport calculations.

Our method is based on standard *ab initio* Born-Oppenheimer MD simulations for the dynamical behavior and DFT-NEGF to calculate the transport properties, by a combination of the results from the SIESTA[27, 28] and TranSIESTA[39] computer codes. The MD simulations are performed using SIESTA, which uses a local basis set and periodic boundary conditions to solve the Kohn-Sham DFT problem. TranSIESTA is built on SIESTA and has the capability to self-consistently solve the Kohn-Sham DFT equations for the non-equilibrium electron density in the presence of a current flow. In this case the assumption of periodicity in the transport direction is removed and the full atomistic structure of both the device and the electrodes are treated. In the following we will describe how the SIESTA and TranSIESTA methods can be used to obtain conductance traces including dynamical effects, which includes (i) a full MD simulation of the time evolution of the junction (w/wo stretching), (ii) transport calculations for a set of geometries obtained from the MD simulation, and (iii) calculation of the non self-consistent conductance traces.

MD simulations using SIESTA
The MD simulations are done in the framework of DFT as implemented in the SIESTA package as described in section 2.3.

The valence electrons in SIESTA are described by a localized basis set, this is very suitable when dealing with transport calculations since the partitioning into L-C-R region as described in the previous section become easy. The orbitals $\{|i>\}$ in the basis set are approximations to atomic orbitals and are centered at the positions of the nuclei in the structure, with a given cutoff radius which make them strictly localized inside this radius. The basis set used here is nonorthogonal where $S_{ij} = <i|j>$ is the matrix element describing the overlap between two basis functions.

The main idea now is to use the MD simulation to obtain an unbiased set of geometries that can model an organic molecule under ambient conditions in a metal junction. Initially a periodic supercell (example of setup in lower part of Fig. 2.2) is constructed as an approximation to the full transport setup (upper part of Fig. 2.2) to be used in the MD simulations. The junction with the molecule is temporally evolved for some arbitrary time, a longer time will sample a larger part of the geometrical phase space, probing a larger part of the energy surface. After each MD simulation the Hamiltonian $\boldsymbol{H}_l$ and overlap $\boldsymbol{S}_l$ matrices are saved, where the index l represents which MD-run it is. Also the final geometries for each run are saved. If several MD simulations are done on the same cell, temperature effects can be probed. The cell can also be stretched or compressed between each MD simulation thus simulating the formation of junctions in a mechanically controlled break junction (MCBJ) experiment.

Self-consistent conductance calculations with TranSIESTA

Starting from some of the geometries saved from the MD simulations fully self-consistent elastic transport calculations are performed with the TranSIESTA package. Two electrodes which are necessary for the transport calculations, are added to the structures, corresponding to the upper part of Fig. 2.2.

In the full TranSIESTA calculation, the transmission function can be calculated under finite bias conditions, *i.e.*, the chemical potential in each lead is shifted by $V/2$, where V is the applied voltage, and a electrostatic voltage drop over the central region is induced. In the self-consistent cycle these effects are fully treated in TranSIESTA leading to the electrodes self-energies and the Hamiltonian depending on the external bias voltage V. Even though a electric field could be induced in the MD simulations it is not so straightforward to translate this to the full transport situation, hence in the following we will neglect voltage dependence and only consider the zero bias (ZB)-conductance of the different junctions.

As in the case of the MD simulations the Hamiltonian $\hat{\boldsymbol{H}}_m$ and overlap $\hat{\boldsymbol{S}}_m$ are saved from each calculation. A separate TransSIESTA electrode calculation is also necessary giving the bulk Hamiltonian and overlap matrices for the electrodes, needed to calculate the self-energies $\hat{\boldsymbol{\Sigma}}_\alpha^{r,a}(\varepsilon)$ when connecting the electrodes to the central region. The self-energies are calculated via already available methods in the Inelastica package[38], the self-energies are

only necessary to calculate once since the electrodes do not change during the evolution of the junction.

Non self-consistent conductance traces

Now we have the $\boldsymbol{H}_l$ and $\boldsymbol{S}_l$ matrices from the MD simulation and $\hat{\boldsymbol{H}}_m$, $\hat{\boldsymbol{S}}_m$ and $\hat{\boldsymbol{\Sigma}}_\alpha^{r,a}$ matrices from the TranSIESTA calculations, and they are combined into a non self-consistent transmission T_{lm}.

   To combine them, differences between TranSIESTA and MD simulations need to be corrected: The MD simulations are done under the assumption of periodic boundary conditions, which are changed into open boundary conditions under the transport simulation. Furthermore, the relative potential energy is changed to having the Fermi energy as reference.

Periodic boundary conditions effect

The MD simulation is done under the assumption of periodic boundary conditions, implying that there will be interactions between atoms in the "left" and the "right" electrodes across the periodic boundary, which is not the case in the transport calculations. This is easily corrected due to the finite range r_α of each basis state $|\psi_\alpha>$ describing the valence electrons in the SIESTA DFT code. The unwanted interactions are removed by setting

$$< \psi_\alpha|\boldsymbol{H}_l,\boldsymbol{S}_l|\psi_\beta >= 0 \qquad \text{if} \qquad |R_\alpha - R_\beta| > r_\alpha + r_\beta \qquad (2.33)$$

where R_α is the position of the nuclei where the basis state $|\psi_\alpha>$ is centered. This correction is only applied for the transport direction, while, perpendicular to the transport direction, the periodicity is preserved.

The potential shift

In the case of TranSIESTA the reference energy is the Fermi energy while in the SIESTA MD simulation the Fermi energy is not used as reference. Hence it is necessary to shift the MD Hamiltonians rigidly to have the same reference energy, this is done by

$$\tilde{\boldsymbol{H}}_l = \boldsymbol{H}_l - \varepsilon_l\boldsymbol{S}_l \qquad (2.34)$$

where ε_l is the Fermi energy obtained in the MD simulations.

Obtaining T_{lm}

Everything needed for the non self-consistent conductance traces is now available and it is possible to calculate the ZB transmission T_{lm} from Eq. (2.26). As indicated in Fig. 2.2, $\tilde{\boldsymbol{H}}_l$ and $\boldsymbol{S}_l$ are pasted into $\hat{\boldsymbol{H}}_m$ and $\hat{\boldsymbol{S}}_m$ and T_{lm} are calculated directly, i.e., non self-consistently, for each combination of l and m. In Fig. 2.3 an example of such a calculation is shown with the full conductance traces T_{lm} for a BDT molecule between two gold electrodes that are being stretched, corresponding to the setup in Fig. 2.2. In the figure, plotted with markers ($\circ, \triangledown, \square$), are conductance values obtained from fully self-consistent
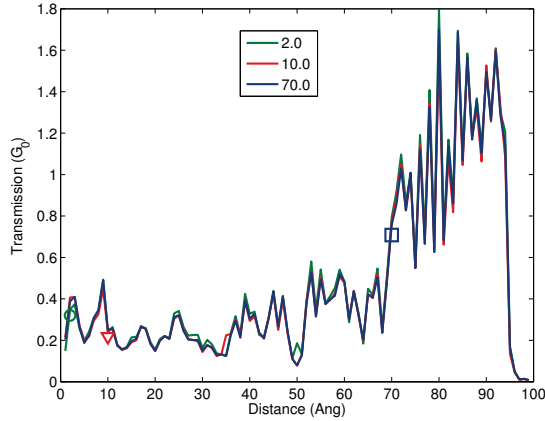
Figure 2.3. Comparison of the approximate conductance traces calculated using different sets of full TranSIESTA calculations, indicated by its m-value in the legend. Note that there are 3 overlapping lines corresponding to approximations based on the 3 different full TranSIESTA calculations. Also shown as symbols are the transmission values obtained from the full TranSIESTA calculations.

TranSIESTA calculations shown for some different stretching distances (2 Å, 10 Å, 70 Å) which are in good agreement with the approximate conductance traces. The figure contains multiple conductance traces corresponding to different m, and as can be seen, the approximation works very well and there is only minimal differences between conductance traces calculated by using different $\hat{\boldsymbol{H}}_m$ and $\hat{\boldsymbol{S}}_m$.

When combining $\tilde{\boldsymbol{H}}_l$ and $\boldsymbol{S}_l$ with $\hat{\boldsymbol{H}}_m$ and $\hat{\boldsymbol{S}}_m$ respectively into T_{lm}, there is a choice of how much of $\tilde{\boldsymbol{H}}_l$ ($\boldsymbol{S}_l$) to copy. In the calculations shown here we keep either one or two gold layers from $\tilde{\boldsymbol{H}}_l$ and $\boldsymbol{S}_l$, symbolized in Fig. 2.2 as region b or c respectively. The choice of number of gold layers has little impact on the resulting transmission as long as the choice is in accordance to the choice of constrained atoms in the MD-simulation. In Fig. 2.4, calculations of T_{lm} for different sub-regions (corresponding to those in Fig. 2.2) are shown. In the MD-simulations here, the two bottom layers of each electrode are kept fixed, hence copying one, two or three gold layers (region b,c or d) from the MD-simulation has little influence on the results. While, instead, only the molecule is kept from the MD simulations and all of the electrode layers from the TS calculations (region a) the transmission results are drastically changed (see blue line, corresponding to the calculation where only a:–:a region is kept in Fig. 2.4).

Effect of stretching the junction
To validate the MD method and to ensure that no spurious effects are introduced when the calculations are stopped and restarted, for example, to save the necessary files and stretch the junction (if wanted), we compare the results

20
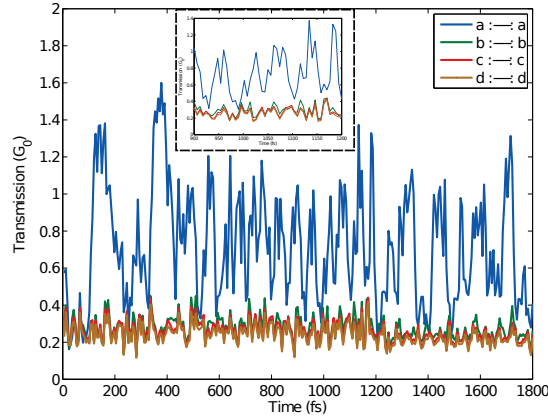
Figure 2.4. Comparison of transmission calculated by keeping different numbers of gold layers from the MD-simulations (0-3). The different curves correspond to the regions defined in Fig. 2.2 (a,b,c,d). The inset shows the same thing but zoomed in between time t=900 to t=1200 to resolve the individual curves.

with results obtained from a standard continuous MD-simulation. In Fig 2.5 are the Kohn-Sham energies and ion temperatures for each step in the continuous MD-simulation shown together with energies and temperatures from our method both without and with stretching (0.01 Å). For the results from the method presented here, the MD is restarted every 10 fs, but, as seen in the figure, the curves (energy and temperature) obtained without stretching are right on top of the results from the continuous run. For the results obtained with stretching, an increase in the potential energy is seen when the junction is elongated, indicated by a shift in the mean value of the energy towards higher values, but the shape of the curve stays intact. We don't want an increase in kinetic energy due to the stretching and, as is seen from the temperature, it stays essentially the same as without stretching.

Still, since the elongation/compression of the junction is done statically by scaling the coordinates, effectively the potential energy in the junction is changed, a sufficient time for relaxation between each stretching event is therefore necessary. The important parameter here is what can be defined as the stretching speed. The first choice was to stretch the junction 0.1 Å each 60 fs, this gives a stretching speed of roughly 167 m/s, which is orders of magnitude larger compared to actual speeds in experiments, but it is still lower than the thermal velocities of the Au atoms (roughly 194 m/s at 300 K). To further investigate the effect of the stretching speed, simulations where the speed was reduced by a factor 10 were performed (v=16.7 m/s), this can be done in two different ways, either by changing the stretch to 0.01 Å each 60 fs or by keeping the same stretching distance, 0.1 Å but changing the time between each stretching event to 600 fs. The computational cost for these two ways to do it is the same (same number of steps in the MD-simulation) but with shorter
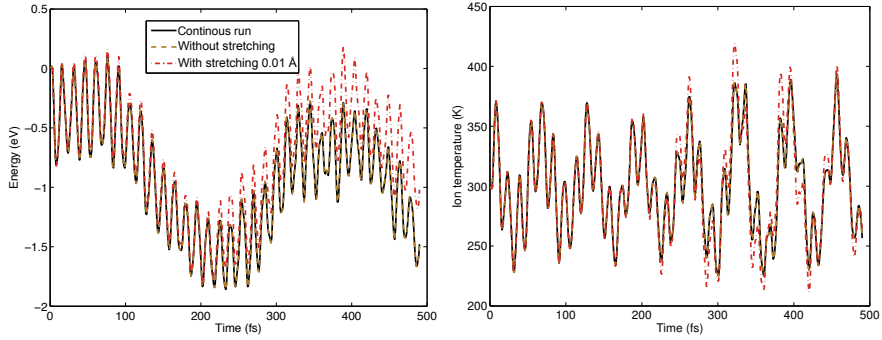
Figure 2.5. Energy vs. time (left) and ion temperature vs. time (right) for a continuos MD-simulation (full black line) compared to the presented method without stretching of the junction (dashed yellow line) and stretching of the junction with 0.01 Å every 10 fs (dashed-dotted red line)

stretching distance one saves more amount of data and get a larger number of points in the conductance curve. In Fig. 2.6 the original calculations are compared to these two methods of decreasing the stretching speed. The actual values between the three calculations differ, as these are highly dependent on the configuration in the junction used for transmission calculations, but all three calculations follow a similar general trend for the transmission, hence the choice of a stretching speed (167 m/s) should be ok, in the same time a shorter stretching distance gives better statistics.

Origin of conductance noise

The conductance traces in Fig. 2.3 show a very rapidly oscillating behavior in the conductance, and it is possible to correlate this to the thermal motion of the atoms in the junction and not to some spurious effect introduced by our approximate method. First, to show that the noise is not due to stretching of the junction, we show MD simulations without stretching of the junction for different temperatures. These simulations were done using a starting geometry close to that shown in Fig. 2.2. Several runs were performed on this geometry, shown in Fig. 2.7 are run with a Nose thermostat of 300 Kelvin (same as we used when stretching the junction), a Nose thermostat of 100 Kelvin and a Nose thermostat of 1000 K. The traces obtained with a thermostat of 300 K and 100 K show similar features, but with more rapid oscillations and also with larger amplitude for the higher temperature. The 1000 K trace shows more rapid fluctuations and with even larger amplitude of the oscillations and it is possible to conclude that the noise is from the thermal motion of the atoms in the junction and not from spurious effects, e.g., convergence problems.

The described method have a great number of applications when it comes to the study of junctions under realistic conditions, for example Paulsson et. al. studied the breaking and evolution of a MCBJ with alkanedithiols [54].
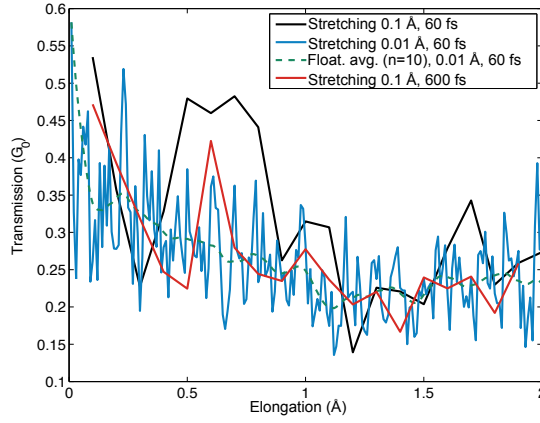
Figure 2.6. Comparison of transmission traces obtained for different stretching speeds. Full black line shows stretching at 0.1 Å/60 fs=167 m/s while full blue (0.01 Å/60 fs) and full red (0.1 Å/600 fs) have both a factor ten slower stretching speeds obtained either by shorter stretch distance (blue) or longer simulation time (red).

Figure 2.7. Comparison of the time evolution for the junction under different temperatures (black: 300 K, red: 100 K, blue: 1000K), without stretching

Further, it has been used in several papers in this thesis to study how different conformers of a molecule influence the conductance (Paper VI and VIII).

2.7 DFT as a framework for quantum transport
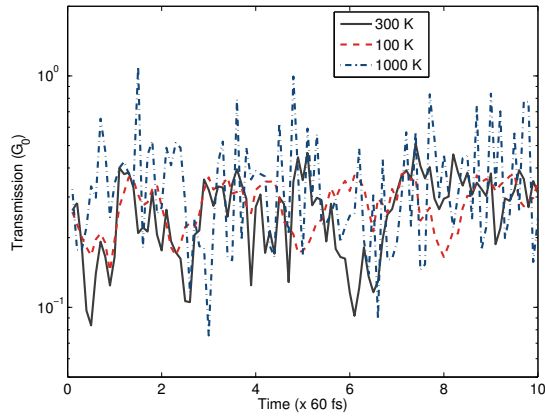
The method of Kohn-Sham DFT, described earlier, has turned out to be one of the most successful methods for describing equilibrium properties of materials. This has also made it a natural choice as a starting point for electron transport calculations. Combining the two also turned out to be very successful when describing systems with an open-boundary under non-equilibrium conditions. As in the case of DFT, where trends in relative energies are reproduced very well, here trends in the magnitude of electron transport between similar systems are reproduced very well. This makes it possible to make quantitive estimates that can be compared with experiments as well as predictions that can be used as a guide for new experiments.

Still, one needs to be cautious, since not only the approximations related to DFT described earlier, but also some less well-founded approximations are introduced when the Kohn-Sham (KS) wavefunctions are treated as the "real" single-particle wave functions and the current is calculated. This means that we assume that the KS-wavefunctions describe the true electron wavefunctions well enough (which we know is not always the case) and that the commonly used XC-functionals can describe the non-equilibrium situation we are dealing with. Since we are only using the single-particle wavefunctions, this method will not describe many-body effects, which are often present at transport processes. It is widely known, for example, that commonly used DFT-methods and functionals underestimate the gap between the highest occupied molecular orbital (HOMO) and lowest unoccupied molecular orbital (LUMO), hence conductance of many molecules weakly coupled to the electrodes are overestimated. This can often be corrected if correlation effects are included for example via GW or self-interaction correction.[39, 55–58]

As mentioned earlier, the convergence of the basis set is a delicate task, and for transport calculations it may turn out to be even harder to define what convergence is. There have been some attempts to make a benchmark of basis sets for transport calculations [59]. The main conclusion is that, as in the case of structural convergence in DFT, a DZP-basis is often enough for transport, increasing the number of basis functions can give even a "better" result when compared to plane-wave calculations. For just a qualitative result a SZ or a SZP is enough, since the shape of the transmission function is reproduced. It has also been found that the Fermi level and some molecular orbitals (MO) are very sensitive to the size of the basis set, changing the basis could shift the Fermi level in/out from the HOMO-LUMO gap or reorder MOs, hence changing the transmission by orders of magnitude[60, 61]. This could alter the interpretation of the conductance between, for example, different conformers

of a molecule significantly. Using the same basis sets, functionals and other parameters when comparing similar systems should overcome most of these difficulties.

To conclude, in this thesis, we model the electron transport with the use of the nonequilibrium Green's function method (NEGF) combined with density functional theory (DFT), which together open the possibility to describe from first principles different systems that could be used in molecular electronics devices.

# 3. Nanoelectrode platform for single-molecule electronics

For the understanding of transport through molecular junctions, techniques for measuring and characterization of molecules in a reproducible way are important. This can be achieved either as many-molecule junctions, where a molecular monolayer is sandwiched between two electrodes, or as individual-molecule junctions where a few-, down to single-, molecules are contacted. The individual-molecule junctions often use techniques which include, but are not limited to, scanning tunneling microscopy (STM) and mechanical controllable break junction (MCBJ). The STM and MCBJ techniques have achieved many significant results, but they have to operate in a laboratory environment, hence, these techniques are not suitable to build actual devices [62].

The alkane-chain, with its simple structure made up of saturated carbon atoms, often serves as a prototype when studying molecular electronic junctions either as thiolated self-assembled monolayers (SAMs) on gold surfaces or as dithiolated in Au-alkanedithiol-Au single molecule junctions. Previous studies using scanning probe microscopy techniques on SAMs have shown that the geometry of the molecular arrangement and especially the tilt angle of the film with respect to the surface normal greatly influences the conduction through the monolayer of molecules [49, 63, 64]. To characterize the alkane chain, dithiolated molecules in unimolecular junctions which are chemisorbed to both electrodes can be used. Even though this is one of the simplest systems, there is a large uncertainty in the conductance of the alkane chain, *e.g.*, the eight-membered alkane chain (octanedithiol) shows conductance values, both experimentally and theoretically, that varies by more than 1 order of magnitude ($G \sim 1 - 20 \times 10^{-5} G_0$, where G_0 is the conductance quantum). The discrepancy is assigned to microscopically different junctions with, for example, different molecule-electrode bonding or different molecular conformations [54, 65–67].

For real devices, a platform that can be transferred outside the lab and that can be contacted by macroscopic contacts is needed. This can be achieved with a nanoelectrode bridge platform where gold nanoparticles (AuNP) are used to contact single or a few molecules. Here we study a nanoelectrode bridge platform [68] where AuNPs of different size are used to bridge the gap (25-30 nm wide) between the electrodes. This setup is simple enough to test different molecular systems repeatedly with good statistics under ambient conditions, *i.e.*, it is possible to use it in an actual device. In a first setup, large

enough (30nm) AuNP were chosen to bridge the nanogap by one single AuNP to contact films of monothiolated molecule coatings on both electrodes (section 3.1). In a second setup, dithiolated molecules that could chemisorb with both ends were used. This was done to make more stable contacts between the electrodes and molecules and meant functionalization of the AuNP with molecules instead of the electrodes. The molecule coated AuNPs were then trapped in between clean electrodes, making chemical bonds in both ends of the molecule to gold surfaces (section 3.2). The drawback of this setup was that it used smaller (5nm) AuNPs, hence a network of metal-molecule-metal junctions was needed to bridge the 30 nm gap. In the last section (section 3.3) we show, by a combination of DFT-NEGF and a model describing the AuNP-molecule-AuNP network between the electrodes, that it is possible to gather information from IETS measurements about the single molecules and configurations in this network.

3.1 Contact configuration of octanethiol coated gold electrodes
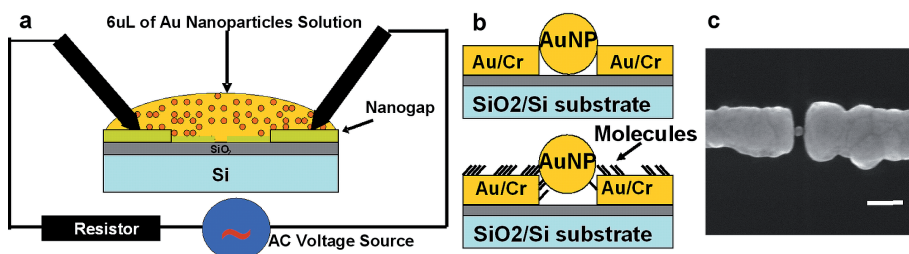
Figure 3.1. a) Schematic of the nanoelectrode setup during a trapping experiment in which probe needles were connected to the contact pads and 6 μL of an aqueous AuNP solution was deposited on top. b) Schematic cross section of a nanogap with one AuNP trapped between non-functionalized electrodes (upper image) and functionalized electrodes (lower image). c) Scanning electron microscope image of a single trapped AuNP in a nanogap. The scale bar is 100 nm

Paper I focuses on the influence of the roughness of the surface on the conduction through a SAM. The setup considered in this section is made up of two nanoelectrodes both coated with a SAM of octanethiol where the gap between the electrodes is bridged by a large AuNP. Figure 3.1 shows schematics of (a) the trapping and (b) the final device. A scanning electron microscope (SEM) image from one of the actual devices is also shown (c). A more detailed description of the platform and the electrophoretic trapping is given in [68] and Paper I, here the focus will be on the theoretical calculations of the junctions.

Measured current-voltage (I-V) characteristics on these junctions show a very large variation in the octanethiol conduction, with estimated resistance from 1 GΩ to 10 TΩ. The large variation in the conduction between different junctions is what we study in this paper, several possible reasons for the variation exist including no well-defined molecular conformations, several molecules in the junction and a very rough gold surface due to the focused ion-beam (FIB) cutting of the gaps.

To model the roughness of the FIB cut electrodes under the film of molecules, we used a gold surface of (110)-symmetry which had undergone reconstruction [69], thus, creating a rough zig-zagged surface with facets of local (111)-symmetry.

To investigate how the experimental I-V curves would be affected by the roughness of the surface we have done transport calculations based on the DFT-NEGF formalism to estimate the zero-bias conductance for different geometries. We considered three different setups in which the opposing electrode surfaces are: *(i)* structurally symmetric but laterally displaced (moved, Figure 3.2a), *(ii)* reconstructed and flat (unreconstructed) (Figures 3.2b and 3.2d), and *(iii)* spatially symmetric (Figure 3.2c). With our setup the Au surface is quite deeply corrugated, yet no artificial patterns were used to model the corrugation. The shortest inter-electrode distance (see Table 3.1) was obtained by minimizing the energy of the simulation cell with respect to electrode separation; all atomic coordinates were additionally relaxed with the electrodes fixed at the chosen distance.

Table 3.1. *Results from DFT and electronic transport calculations*

System name (see Figure 3.2)	a)	b)	c)	d)
Distance between electrodes (Å)[a]	7.76	8.43	8.87	10.29
ΔE (eV)[b]	0	2.20	1.10	8.31
Zero-bias transmission T ($G_0 \times 10^{-3}$)	12.3	4.5	0.65	0.3
Resistance/mol (MΩ)	2.1	5.7	39.7	86

[a] The distance between electrodes is the distance between two nearest Au-atoms from different electrodes.

[b] ΔE is the difference in total energy between the different contact configurations where system a) (moved) has the lowest energy.

To analyze how the effective thickness of the molecular film affects the resistance, we consider the results collected in Table 3.1. It is apparent that only one of the two molecules shown in Figure 3.2c, and especially in Figure 3.2d, is properly connected to the topmost electrode surface. This observation demonstrates that, adsorbed at non-ideal surfaces, molecules experience a larger contact area with the electrode, which, coupled with the fact that they are tilted at an angle of $-52.5°$ [49] with respect to the surface normal, results in a decreased effective length between electrodes and increased

| (a) "moved" | (b) "flat" | (c) "symmetric" | (d) "flat+2Å" |
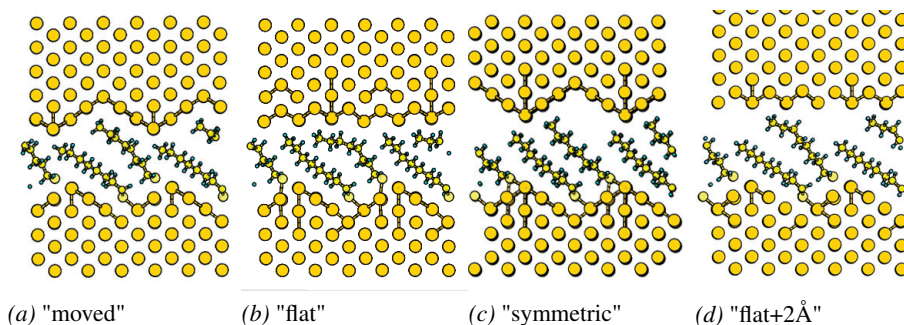
Figure 3.2. Atomic configurations considered in theoretical simulation-side view of the contact area seen along the [$\bar{1}$10] direction. Different structures obtained by moving the top electrode correspond to different inter-electrode separations (see table 3.1). a) Symmetric but laterally displaced electrodes, b) reconstructed and flat surfaces, c) spatially symmetric surfaces and d) same as b), but additionally spaced by 2 Å.

inter-molecular tunneling. Thus, the effective resistance of the molecules is decreased.

To further describe what we mean by the different effective lengths between the molecules we plot the current densities in Figure 3.3. Assuming a small positive bias on the bottom electrode, the currents flowing up through the molecule are plotted, where the cross-section of the arrows is proportional to the magnitude of the current density. We can see that setup (a) and (b) show very similar behavior, where the current flows almost straight through the junction, either tunneling from the top gold atom or via the left anchoring sulphur atom straight to the top of the right molecule (intermolecular tunneling) and to the top gold electrode. Thus, giving the effective length of the current path as the distance from the top gold atom on the bottom electrode to the bottom gold atom on the top electrode. In setup (c) the main current path is along the backbone of the left molecule, and the effective length of the current path has to be measured along the molecule instead, increasing it greatly, hence it has a much lower transmission probability, which is seen in the Table 3.1.

We find that the resistance values calculated for OT molecules attached to different step edges vary by 1-2 orders of magnitude. Therefore, the attachment geometry of the Au-OT-Au junction is an important factor influencing the electron transmission through the electrodes. It should be emphasized that the structures that were calculated (Figure 3.2) use the rearrangements of Au-atoms that achieve the lowest energy configuration, while in the actual experiments the shape of the junction is defined by the shape and relative arrangement of the NP and the electrode.

To conclude this section, we have studied the influence of the roughness of the surface on the conduction through a SAM of octanethiol molecules, where

30

| *(a)* "moved" | *(b)* "flat" | *(c)* "symmetric" |
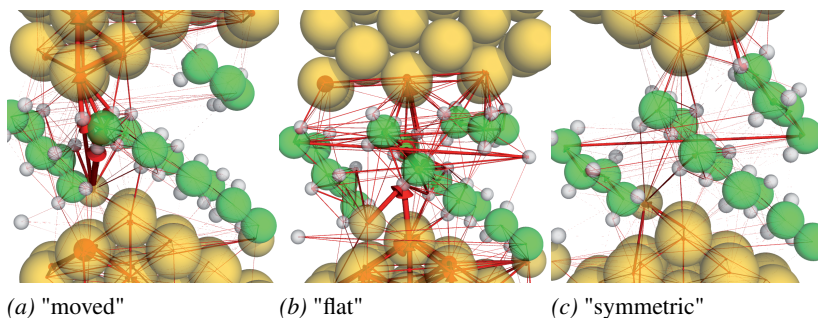
Figure 3.3. Current paths for setups a), b) and c) corresponding to Figure 3.2, showing both intermolecule (a and b) and intramolecule (c) tunneling paths where the cross-sectional area of the arrows is proportional to the current density flowing upwards.

we find a difference of 1-2 orders of magnitude of the conductance through the layers depending on the attachment geometry. Thus, the resistance of the assembled device will largely depend on the amount of well-conducting molecules, which, in turn, is very sensitive to the structure and relative orientation of the surface defects. Nevertheless, in the experiments, the resistances vary by nearly four orders of magnitude and therefore, in addition to the influence of the OT-Au configuration, it is likely that other factors such as pin holes in the OT layer and shape of the NPs, where number of contacted molecules can vary greatly depending on the facetting of the NP, would influence the variation in measured resistances in this SAM based nanoelectrode platform.

3.2 AuNP-networks of protected/deproctected octanedithiol

In paper II, we carry out theoretical calculations to investigate junctions where a network of smaller AuNPs (4-5 nm in diameter) are used to make a covalently bonded organic network between the two nanoelectrodes (see schematic in right panel of Figure 3.4). The focus lies on which atomic configurations are probable in these junctions and to verify that the increase in measured conductivity after the acid treatment is due to deprotection of the molecules and creation of a chemisorbed network.

To enhance the reproducibility of the device, Wallner et al. developed a route to make chemical contacts to both electrodes [70], instead of just one as in the previous section. This meant that the OT molecule needs to be exchanged for octanedithiol (ODT) molecules with functional groups at both ends to be able to chemisorb at two adjacent gold surfaces. Due to the reactivity of the thiol groups, some way to control that they bridge the gap and not only "backbite" to the same surface is necessary. Instead of coating the
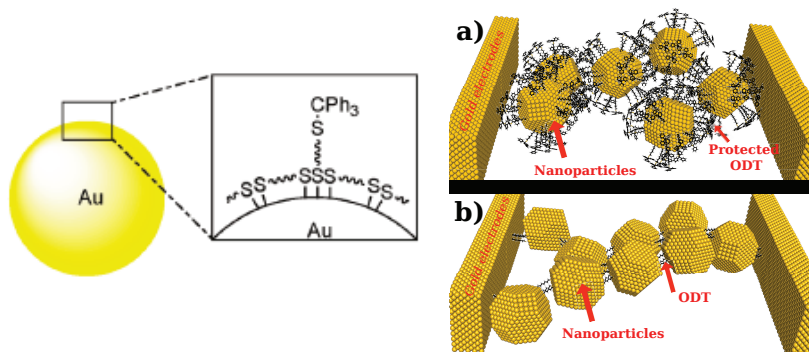
Figure 3.4. **Left**: Schematic figure of thiol-stabilized gold nanoparticles with a coating of free standing protected alkanedithiols. Reproduced from [70]. **Right**: Schematic of how a nanoparticle-molecule-nanoparticle network between two gold electrodes can look: a) nanoparticles with protected molecules. b) nanoparticles with deprotected molecules that have chemisorb to two particles. In both cases stabilizing molecules on the surface are left out for clarity.

electrodes with molecules (as previous), AuNPs are synthesized using stabilizing 1,8-octanedithiol molecules on the surface and with α, ω-alkanedithiols whose outer ω-thiol is protected by a triphenylmethyl (trityl) group reaching out from the surface, a schematic is shown in left panel of Figure 3.4.

Measurements on the protected and deprotected molecules demonstrate high resistance around 325 GΩ and 1 GΩ for protected and deprotected molecule, respectively. During removal of the trityl group, the outer ω-thiol is "free" and in the ideal case can attach to an adjacent AuNP, as shown in Figure 3.4, thus forming the covalently bonded network with more stable junctions. In the measurements, an increase of the conduction with somewhere between 2 to 5 orders of magnitude can be seen (Figure 3.5b), where most of the devices show an increase of a factor 100. It is also found that the junction with protected molecules shows a large spread in the magnitude of the conduction, responsible for the large spread in the change in conduction during deprotection as well, whilst the junction with deprotected molecules shows a spread less than two orders of magnitude indicating that we have a device with stable chemical contacts and high reproducibility.

To get a better understanding of the molecular configurations in the junctions, we have modeled probable atomic configurations as shown in Figure 3.5a, and our obtained results for the transmission for the different setups are shown in Figure 3.5c.

For the single octanedithiol chain linked via the sulfur atoms in both ends to the gold surface (setup I in Figure 3.5a), we have obtained a conductance of $30.5 \times 10^{-5} G_0$, ($G_0 = 2e^2/h$) comparable with other theoretical studies [54]. In the case of ω-trityl protected 1,8-octanedithiol molecules (setup II in Figure 3.5a), we have obtained a single molecule conductance fifteen times lower as
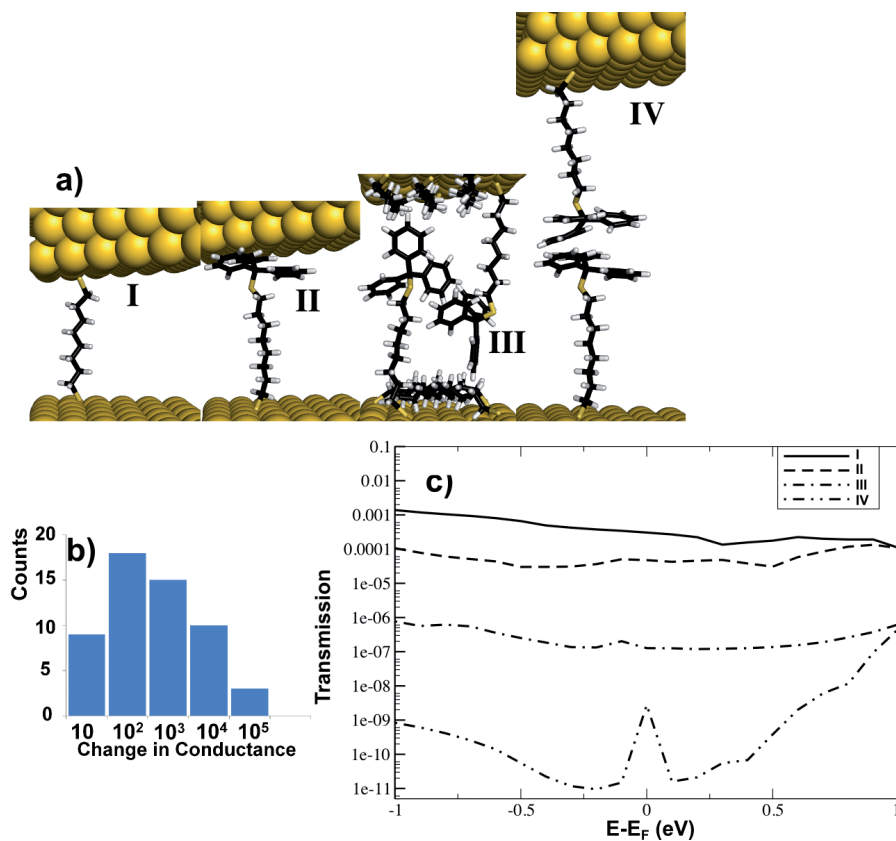
Figure 3.5. **a)** Atomic configuration considered in theoretical simulation I) 1,8-ODT chemisorbed at two nearby gold surfaces, II) ω-trityl protected 1,8-ODT chemisorbed at one end and physisorbed at other end, III) ω-trityl protected 1,8-ODT chemisorbed at one end in presence of surface layer of backbiting 1,8-ODT, IV) ω-trityl protected 1,8-ODT chemisorbed at one end with surface at maximum separation. **b)** Histogram of measured changes in conductance going from ω-trityl protected 1,8-ODT to deprotected 1,8-ODT. **c)** Zero-bias transmission for the four considered setups.

compared with the unprotected molecule. The decrease in conductance found here can be accounted for by the increase in distance between the gold electrodes from 15 Å to 18 Å to accommodate trityl groups. Assuming that the tunneling decay factor of the alkane chain is 0.7 Å^{-1} [17, 63] would result in a decrease in conductance of around 10 times with this increase in distance. This can not explain the increase seen in experiments. Instead we tried the extreme where the protected molecules bind head to head, *i.e.*, setup IV in Figure 3.5a. This configuration has a conductance of roughly 10^{-9} G$_0$, hence about 6 orders of magnitude smaller compared with the deprotected molecule. This increase is also outside what is observed in experiments, thus we have found the two extreme configurations for the protected molecule and the observed configuration should lie somewhere in between.

To investigate the configurations in between, it is necessary to take the back-biting molecules into account since they might affect the distance between the electrodes when the protected molecules are clustering together. The results from this calculation (setup III Figure 3.5a) show a zero-bias conductance of 1.3×10^{-7} G$_0$, *i.e.*, a decrease with three orders of magnitude, compared with the octanedithiol chain. This is in good agreement with the observed change in the measurement.

In conclusion, our results suggest that it is not the protection group itself that is responsible for the experimentally measured decrease in conductance, but the increased distance between gold surfaces due to the size of the protection groups and the extra effective thickness added by the layer of molecules on the surface.

3.3 Vibrational signatures from short octanedithiol-AuNP chains

One of the most convincing signatures of single molecules in charge transport junctions comes from the identification of their vibrational structure [71–73]. The demonstration of IETS spectra is an important step to validate that conduction in a molecular electronic platform occurs through the molecules of interest [74]. In paper III, we show by IETS measurements on the platform investigated in the previous section that the signatures from individual molecules can be identified. When changing from the large AuNP and the coated electrodes in the first section to having smaller AuNPs coated by doubly functionalized molecules, as in the previous section, several AuNPs are needed to bridge the electrode gap, thus, making up a network of molecules. To identify the signatures from vibrational transitions of ODT molecules in these kinds of networks, we have modeled this by DFT-NEGF taking into account the complex network of metal-molecule chains in the junction. A sketch of a possible network and the measured d^2I/dV^2 (IETS) together with our modeled spectra are shown in Figure 3.6.
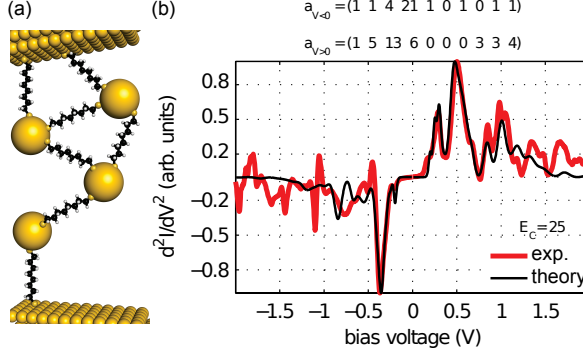
Figure 3.6. Theoretical modeling of the measured IETS spectra. (a) Schematic of one molecular chain in the nanogap. The chain consists of a number N molecular junctions and $N-1$ AuNPs linking the molecules together. (b) Calculated IETS spectra obtained by least squares fitting of the model (see Supporting info of Paper III) using the number of chains with N=4, 5,..., 14 molecular junctions. For the calculations we have used the vibrational modes $\varepsilon_n \in [40, 84, 109, 122, 142 \text{ meV}]$ with corresponding coupling to the tunneling electrons $\varepsilon^2 \in 1.5625 \times [4.4, 3.7, 0.6, 0.5, 0.1]$ in units of the elastic tunnel current. The activation energy is set to $E_C = 25$ meV, while the temperature is set to $T = 20$ K for the sake of broadening. The experimental curve has been Lorentzian-broadened by 10 meV.

To understand the signatures observed in the measured d^2I/dV^2, we have modeled both the elastic and inelastic conductance through the Au-molecule-Au junction. The elastic conductance was calculated as in the previous sections, the inelastic current was calculated through the lowest order expansion (LOE) method described in Section 2.5.3. To apply LOE, the system needs to have a weak electron-phonon coupling and the density of states close to the Fermi energy should vary slowly. This can be justified by the transmission spectra in Figure 3.7 which has no sharp peaks close to the Fermi energy, hence the conductance is almost bias independent. It has also been shown that less than 3% of the electrons undergo inelastic scattering for alkanethiols [75].

The calculated d^2I/dV^2 for an ODT molecule sandwiched between two gold surfaces is shown in Figure 3.8, together with the most important vibrational modes of the molecule. The main vibrational modes are found at $E_{v1} = 40$ meV (Au-S stretch), $E_{v2} = 80$ meV (C-S stretch), $E_{v3} = 109$ meV (CH$_2$ twist), $E_{v4} = 122$ meV and $E_{v5} = 142$ meV (two different modes of C-C stretching). In Figure 3.8 a), the d^2I/dV^2 for the trityl-protected molecule is also shown by the dashed line as a comparison, where it is possible to see that the low-bias peaks appear at similar voltages, hence corresponding to similar modes, but with different intensities. Further, the higher C-H stretch mode ($E_v = 350$ meV) is much more pronounced for the protected molecule, hence it should be possible to separate the two molecules from their signatures. The two lowest modes E_{v1} and E_{v2} have the strongest coupling to the current which
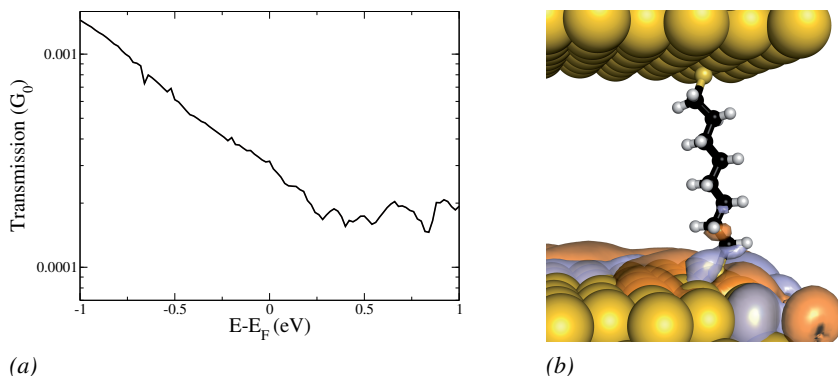
Figure 3.7. (a) Zero-bias transmission for ODT molecule sandwiched between two gold electrodes. (b) The main conduction channel (from bottom electrode to top) for the octanedithiol molecule

is reasonable since those vibrations include the anchoring thiols (shown in Figure 3.8 b and c) which mediate the electronic coupling between the electrodes and the molecule. This can be seen in Figure 3.7b, where the main conduction channel is localized close to the terminal sulfur atom.

The total resistance of a single chain of AuNP-molecules containing N molecules in between two gold electrodes is the sum of the resistances of the N molecules in the chain (Figure 3.6a). Several parallel chains contribute to the current as parallel resistors in a circuit. Geometrically, at least four molecules are needed in the molecule-AuNP chain to bridge the 20 nm gap, thus, in the model we use, the smallest number of allowed molecular junctions is four and the largest is fourteen. The voltage drop U_m in a chain with N molecules is $U_m = U_B/N$. Consequently, a chain with N molecules will contribute to the IETS spectrum with a weight being the number of repetitions of this chain.

To model the actual device, the carrier transport related to the vibrational states of the molecules through a molecule-AuNP chain was simulated taking into account the activation energy related to the Coulomb energy of the AuNP array. As input to the model, the main vibrational modes and their electron-phonon couplings obtained from the DFT-NEGF calculations were used. The linear combination of the IETS spectrum of all chains from the model is then fitted to the experimental IETS spectrum. Due to the asymmetry of the measured curves, fitting of the model is carried out separately for negative and positive bias. The resulting curve is shown in Figure 3.6b, where the numbers of chains with 4-14 junctions needed to obtain the best fit to the experimental spectra are noted above the curves.

For the peaks at low energy, the fits approach well the experimental spectrum. Since the experimental peaks at these low energies are broad , they can contain several vibrational peaks. The E_1 and $E_{1'}$ peaks have a FWHM of

(a) Inelastic spectra

(b) Au-S stretch (40 meV)

(c) C-S stretch (84 meV)

(d) CH2 twist (109 meV)
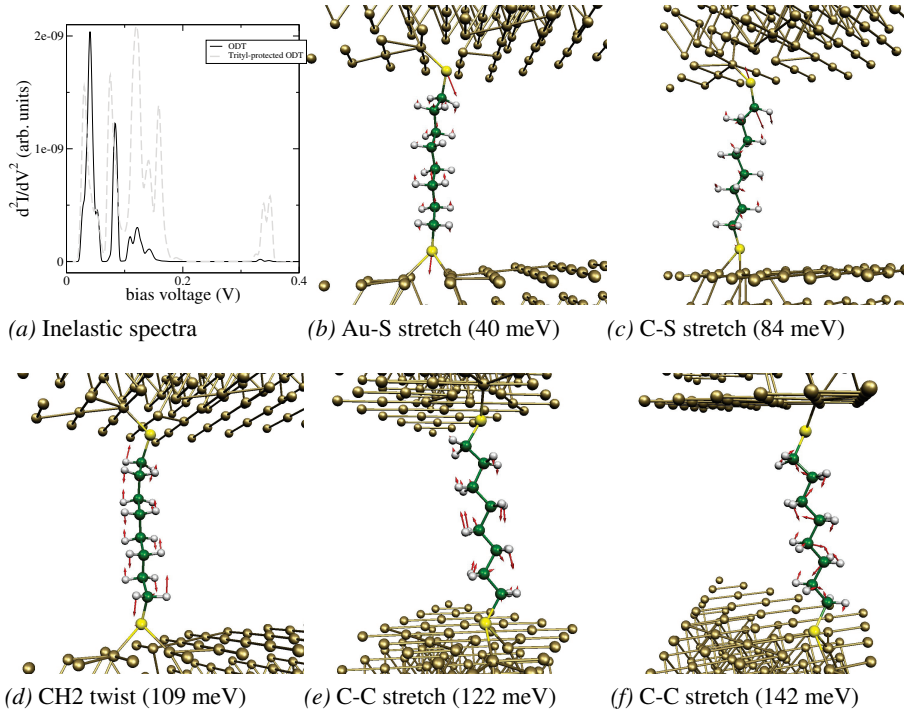
(e) C-C stretch (122 meV)

(f) C-C stretch (142 meV)

Figure 3.8. (a) Inelastic spectra (d^2I/dV^2) for a ODT molecule between gold electrodes. (b)-(f) The main vibrational modes of the molecule. Au-S stretch, C-S stretch, CH_2 twist and two different C-C stretch

80 meV, and from their energy position we can estimate that they can contain the Au-S signal from AuNP-molecule chains containing five, six and seven serial molecular junctions. The E_2 and $E_{2'}$ peaks are 100-140 meV wide and can contain the signal corresponding to the C-S stretching vibration from AuNP-molecule chains containing five, six and seven molecular junctions. These estimations are in agreement with the fit resulting in the strongest contributions to the IETS spectra from AuNP- molecule chains containing five, six and seven junctions. These numbers of AuNPs correspond well to the expected number of AuNPs in AuNP-molecule chains since, physically, at least four NPs resulting in five junctions are needed to bridge the 20 nm NE gap. Thus, the E_1, $E_{1'}$ and E_2, $E_{2'}$ are mainly dominated by the Au-S and the C-S stretching vibrations of the ODT-Au junctions.

In conclusion for this section, we have made a model that can quantitatively explain the observations in the experimental IETS spectra modeled by a series of parallel molecule-AuNP chains that make a network between the nanoelectrodes. Our model takes into account the detailed electronic structure of the molecules in such junctions, and combine it with the complex network struc-

ture and effects from molecular charging and vibrations. Using this model we can identify signatures from the molecules and estimate the number of conducting molecules.

Summarizing this chapter, we have studied a platform that can be used for molecular electronics measurements down to a few molecules. Using large AuNPs (diameter close to the electrode-electrode distance, $\sim 25 - 30$ nm) structural defects on the electrodes and AuNP have great influence on the conductance, changing it by several orders of magnitude. Instead, changing to smaller AuNP (diameter ~ 5 nm) a AuNP-molecule-AuNP network is needed to bridge the gap, but in this case the reproducibility is enhanced and the measured resistance between different junctions are similar. Furthermore, by IETS measurements on the networks using the model developed here it is possible to identify signatures of single molecules.

4. Molecular switches

A molecular conductance switch is a molecule where the conductance, the ease at which a current can be passed through it, can be manipulated by an external stimuli. For the realization of molecular memory or logic devices, molecules that can function as active elements, for example rectifiers and molecular conductance switches, are of great importance [76, 77]. To design such types of molecules usually two steps are necessary. To begin with, a proof of principle study is necessary to show that the novel type of molecular switch is working. Later the molecular structure can be changed (substituents, etc.) to optimize the properties of the switch. In this way it is possible to generate families of molecules based on the same switching principle. Furthermore, in applications a third step is necessary where the designed switches need to be connected to the electrodes which often can lead to loss of functionality in real systems, but this is something we are not studying here [78].

There exist several external stimuli that could be applied to switch a molecule. The switching can be induced by the current running through the molecule, an external field, light or even by temperature. Furthermore, the possibility to switch the same molecule with different stimuli makes systems that build on those molecules even more versatile. Molecular switches can be divided into roughly two categories:

- redox/polarization-switches
- isomerization switches

In the redox/polarization-switches [79–81], the molecule (or part of it) takes up or looses an electron, and to study these kinds of switches the time-dependence of the charging of the molecule must be considered, which is not possible with the methods considered here. Instead, in the following sections we are going to study some different types of isomerization switches [78, 82–88], where the 3D-structure (geometry and/or connectivity) of the molecule is changed. When the molecule is charged, as in the first case, small conformational changes are often introduced, still the distinction in these two classes can be used.

The basic requirements [89] for a molecular reaction to be suitable for switching applications are:

1. A high difference in the magnitude of the conductance in the ON and OFF states, *i.e.*, high switching ratio (SR).
2. The two states need to be stable.
3. There needs to be a sufficiently high barrier between the ON- and the OFF-states to hinder accidental (de-)activation.
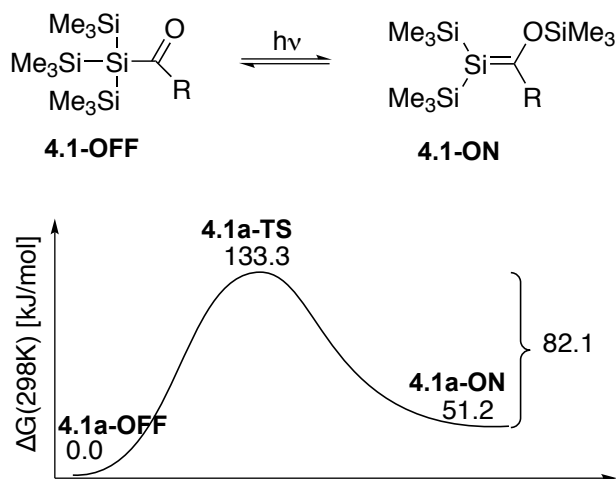
Scheme 4.1: Photochemical [1,3]-silyl shift of acyloligosilanes **4.1-OFF** to their isomeric Brook-silenes **4.1-ON**, and the thermal back-rearrangement (**4.1a** R = *t*-Bu, **4.1b** R = adamantyl [90, 91], and **4.1c** R = Me [92]). Reaction and activation free energies for the thermal processes of **4.1a** computed at B3LYP/6-31G(d) level as reported in paper IV (*vide infra*). Transition state abbreviated as TS.

To fulfill these requirements, the potential energy curve for the reaction should show characteristics as shown in the bottom of Scheme 4.1, and the molecular switch should ideally have an ON state with a conjugated path delocalized over the complete molecule. The compound representing the OFF state, on the other hand, should have a disruption in its conjugation. The disruption could be accomplished in several ways, the two most common are either by a *structural isomerization* where the internal bond connectivity is changed, possible leading to a saturated molecular segment. The second way to achieve switching is by a *stereoisomerization* where the bond connectivity is unchanged, and instead, *e.g.*, a large twist in the molecule decreases the conjugation. At the same time, for a possible use in a solid state device, the length of the molecule should stay essentially the same which has been a major drawback for some of the previously studied molecular photoswitches, *e.g.*, azobenzenes [84–86].

In the first section (section 4.1) we have studied four different families of switches that undergo a structural isomerization activated by light and/or temperature. This is followed in section 4.2 with a family of stereoisomerization switches activated by force that leads to a change in the length and conformation of the molecule.

4.1 Photochromic switches

In this first section we study some different families of switches, where all can be activated by light and in most cases also temperature. These compounds are planar and have π-conjugated paths spanning one of the states, the other state having a disruption in the conjugation introduced by a structural isomerization.

4.1.1 The [1,3]-silyl migration as a light-controlled switch

In paper IV we start by a proof of principle study of the [1,3]-silyl shift as the base for a molecular switch. This structural isomerization reaction (shown in Scheme 4.1) was used by Brook and co-workers to form the first isolable silene in 1981 (Scheme 4.1) [90, 91]. The silene is a compound having a central Si=C double bond, in here connected to π-conjugated substituents, thus, having a π-conjugated path spanning the complete molecule [93–97].
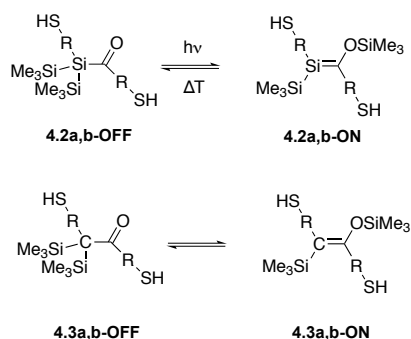
Scheme 4.2: Potential acyloligosilane/Brook-silene switches and their carbon analogues, where R = -CC-C_6H_4- for **a** and R =-C_6H_4- for **b**.

Our initial model reaction for the acylsilane/Brook-silene switches, together with the analog carbon reactions, are displayed in Scheme 4.2. These model silenes have a linearly conjugated path stretching between the two ends of the molecule, whereas the acyloligosilanes have an interruption. We first examine the acyloligosilane/Brook-silenes in their *trans*-conformers with thiol end-groups.

To estimate the switching properties of the acylsilane-to-silene transition we performed first principles DFT-NEGF-calculations for the acetylenic compounds (**4.2a/4.3a**). The current response for different bias voltages are shown in the left panel of Figure 4.1. Looking at trends in the current response, both the OFF and ON states of compounds **4.2a/4.3a** show a similar behavior with linear increase of the current for low voltages and more rapidly increasing current at higher voltages. To investigate their performance as switches we calculate the ON/OFF switching ratio of the current for both the zero-bias limit as well as for a bias of +1 V. Due to the unsymmetric nature of these molecules we also investigate if they have a rectifying property on the current, hence if

Table 4.1. *Current characteristics of 4.2a and 4.3a*

| Compound	SR^a (0 V)	SR^a (1 V)	RR^b
4.2a-OFF	270	39	2.6
4.2a-ON			0.9
4.3a-OFF	31	15	1.4
4.3a-ON			0.9

[a] Conductance ON/OFF switching ratio.
[b] Rectifying ratio, calculated as the ratio between the currents at bias voltages of +1 V and -1 V.

they could function as diodes [13]. These results are shown in Table 4.1. The ON/OFF ratio is higher for compound **4.2a** compared to the all-carbon switch **4.3a**, and from Figure 4.1 it can be seen that this is due to a more conducting OFF-state for **4.3a** while the current response is very similar for the two ON-states. When going to higher biases the switching ratio decreases due to the stronger current-response from the low-conducting acyloligosilanes and ketones.

To explore the physical mechanisms behind the switching, the density of states spatial distribution [98] can be calculated. Shown in the right panels of Figure 4.1 is the number of states/(eV×Å×atom) along the transport direction, where the x-axis is the coordinate along the transport direction and the y-axis shows the energy ($E - E_F$) for the state, where the magnitude of the DOS is indicated by the color, from blue (low) to red (high).

The disruption in the conjugation at the saturated central part is seen for **4.2a-OFF** as a localized state in the center of the molecule about 0.5 eV below the Fermi level (E_F) of the electrodes. Thus, this compound is not so highly conducting. By introducing the linear conjugation via the [1,3]-silyl shift compound **4.2a-ON** (**4.3a-ON**) is formed having a Si=C (C=C) double bond. The conjugation of the molecule shifts the conducting state closer to E_F, and at the same time it is delocalized over the complete molecule, thus, better coupled to both electrodes, making this compound better conducting.

The first part showed that the [1,3]-silyl shift is a promising reaction for a molecular conductance switch, however, compound **4.2a** has a drawback, as it was found to have a large length variation when progressing along the reaction coordinate, especially at the TS, hampering its potential use as a solid state device. To overcome this last issue we propose a cyclic central unit of the molecule (shown in the left panel of Fig. 4.2) reducing the flexibility while at the same time keeping the switching properties of the linear molecules. By changing the migrating group and the acceptor group it is further possible to tune both the thermodynamics and kinetics of the reaction. The thermodynamic and kinetic properties of the investigated cyclic systems are found in Paper IV and Fig. 4.2. The focus has been on three parameters; the nature of the migrating group (silyl or germyl), the steric bulk of the migrating group
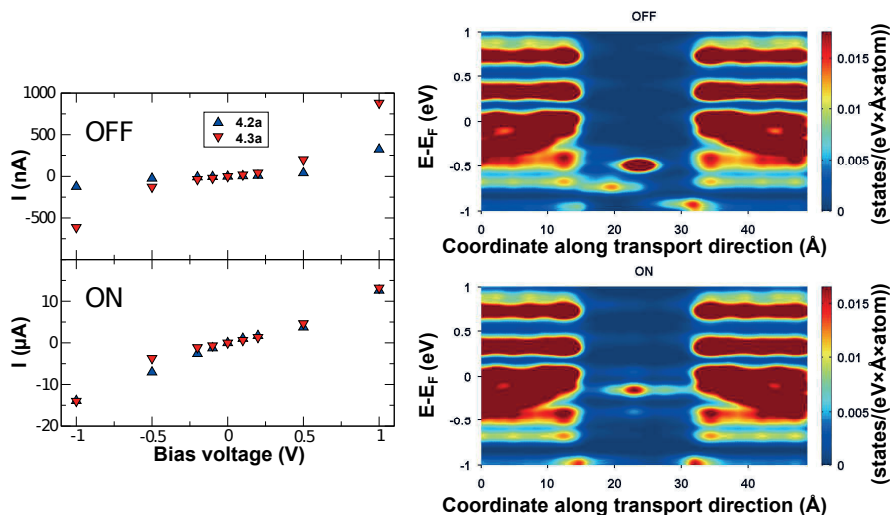
Figure 4.1. **Left**: Calculated current-voltage (I-V) characteristics for OFF and ON state structures of compounds **4.2a** and **4.3a**, respectively. Note the different scales for the calculated currents in the ON and OFF states. **Right**: Space resolved normalized density of states at zero bias for the junctions with compound **4.2a**. The OFF-state is shown in the top panel and the ON-state in the bottom panel. The space resolved density of states have the transport coordinate on the x-axis and the energy of the state on the y-axis. The color scale goes from blue (low density of states) to red (high density of states).

(EMe_3 or E^tBu_2Me, where E = Si or Ge), and the acceptor group (A = O or NMe).

Due to computational cost we have chosen to study the transport characteristics of compounds **4.4**, **4.12** (O-acceptor and trimethylsilyl migrating group), **4.8**, **4.16** (NMe-acceptor and trimethylsilyl migrating group), and **4.17** (NMe-acceptor and $SiMe^tBu_2$ migrating group) using DFT-NEGF here. The current-voltage results and their switching ratios are shown in Figure 4.3 and Table 4.2, respectively. Compared to the previous linear compound we find larger switching ratios at zero bias. By introducing the cyclic unit interference effects, similar to those observed by Solomon et al. in phenyl rings [99], appear in the OFF-compounds lowering their transmission close to E_F. This partly explains the higher switching ratios at low bias. The interference effects can clearly be seen in the transmission spectra where there are several pronounced dips (anti-resonances) for the OFF-compounds with the phenylacetylene group (-CC-Ph) shown in the middle panel of Figure 4.3. For the shorter compounds (**4.4** and **4.8**) transmission in the σ-systems of the molecules can now start to play an important role, and this can hide interference effects in the pπ-system.
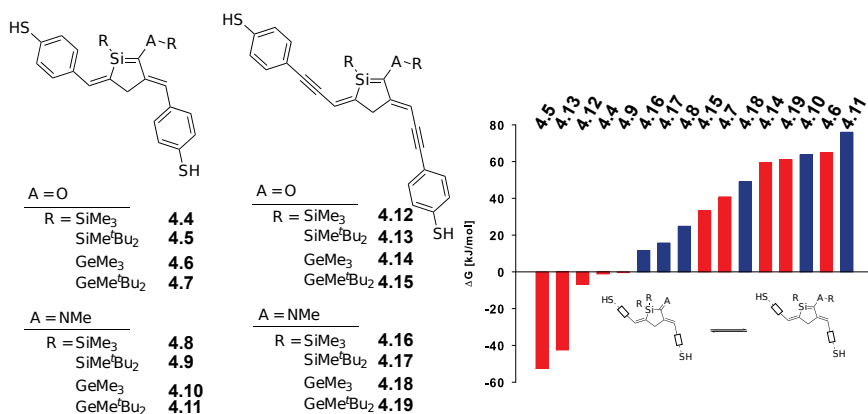
Figure 4.2. **Left**: Suggested cyclic molecular conductance switches with different acceptor moieties and migrating groups. A = NMe or O, and R = $SiMe_3$, Si^tBu_2Me, $GeMe_3$ or Ge^tBu_2Me. **Right**: Relative reaction energies for the extended cyclic silane/silene switches. Blue bars denote N acceptor groups (A= NMe), while red bars denote the oxygen acceptors (A= O).

At higher bias, the switching ratio drops to moderate levels for the cyclic compounds similar to the linear analogues. As in the case of the reaction energies, we see that the NMe acceptor groups (compounds **4.8**, **4.16** and **4.17**) are the most promising candidates with switching ratios on par or higher compared to other compounds studied here and in previous investigations [77, 83, 87, 100]. Introduction of the bulkier migration group ($SiMe^tBu_2$, compound **4.17**) not only will provide higher steric protection and hence higher kinetic stability but will further enhance the switching ratio. The ON-compounds have rectification ratios (RR) close to unity, which is beneficial for practical applications since there will be no directional dependence when running a current through the switch. On the other hand, some of the OFF-compounds have large RR (especially compounds with O-acceptors, **4.4** and **4.12** in Table 4.2), opening the possibility to use them as diodes.

Furthermore, we apply a single-level transport model to investigate the influence of the effective coupling (Γ_L, Γ_R) to the left and the right electrode, and the distance between the closest molecular orbital (E_0) and E_F of the electrodes on the current. For a more in-depth description of the model and the results, refer to Paper IV. The main findings are that the switching occurs due to either a change of the distance between the closest MO and E_F, a change in the coupling between the MO and the electrodes, or a combination of both. However, to have a large SR, the molecule should ideally have both a large change in distance between E_F and the closest MO, and a large change in the coupling between the electrodes and the MO when it is changed between the OFF and the ON-states.
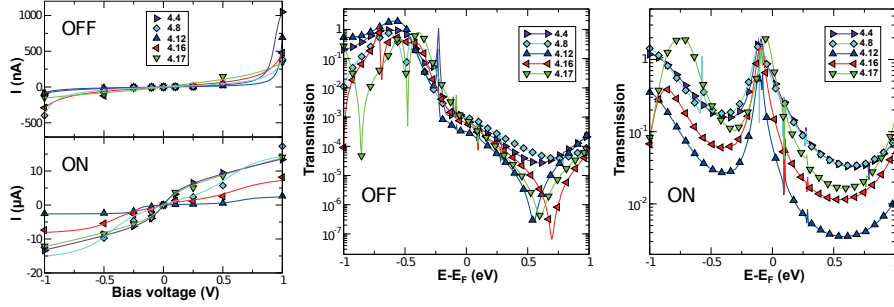
Figure 4.3. **Left**: Current-voltage of cyclic switches and model calculations. Markers denote values obtained from the DFT-NEGF calculations while the full lines are obtained from the model calculations. Note the different scales for the calculated currents in the ON and OFF states. **Middle**: Transmission spectra, at zero bias (V = 0), for the OFF-compounds. **Right**: Transmission spectra, at zero bias (V = 0), for the ON-compounds.

Table 4.2. *Current-voltage characteristics of cyclic compounds*

Compound	DFT-NEGF calculations			Model calculations				
	SR^a (0 V)	SR^a (1 V)	RR^b	$E_0{}^c$ (eV)	Γ^d $(= \sqrt{\Gamma_R\Gamma_L})$	(meV)	ε_- $(\varepsilon_+)^e$	$\Gamma_R/\Gamma_L{}^f$
4.4-OFF	718	13	11.8	0.46	5.5		7.5 (104.3)	13.9
4.4-ON			1.0	0.08	55.0		2.4 (2.4)	1.0
4.8-OFF	503	45	1.0	0.50	7.7		24.5 (24.5)	1.0
4.8-ON			1.4	0.16	36.9		7.2 (5.0)	0.7
4.12-OFF	203	4	8.7	0.49	4.3		12.8 (74.2)	5.8
4.12-ON			1.1	0.06	5.7		4.3 (2.5)	0.6
4.16-OFF	314	17	1.6	0.54	10.1		16.7 (43.4)	2.6
4.16-ON			1.1	0.09	18.7		3.4 (2.8)	0.8
4.17-OFF	1157	41	2.3	0.52	13.9		3.6 (7.6)	2.1
4.17-ON			1.2	0.08	50.0		2.5 (2.6)	1.1

[a] Conductance ON/OFF switching ratio.

[b] Rectifying ratio, calculated as the ratio between the current at bias voltage +1 V and -1 V.

[c] Distance between the most conducting level and E_F (V=0).

[d] Effective coupling between the most conducting level and the electrodes.

[e] Proportionality factor for movement of the conducting level under bias ($\tilde{E}_0 = E_0 \pm \frac{V}{\varepsilon_\pm}$ for $\pm V$, $\varepsilon_+ = \varepsilon_- \Gamma_R/\Gamma_L$)

[f] A measure of the unsymmetry of the effective coupling to the electrodes.

To conclude this section, we have studied the [1,3]-silyl shift as a base for molecular conductance switch. We have found that the proposed switches fulfill the criteria for a useful reversible molecular switch, as given in the beginning of the chapter, *i.e.*, a high ON/OFF conductance ratio, high enough barrier separating the two states, and small length variations in between the OFF and ON-states (and at the transition states). The switching process can be explained by off and on-resonant transport by our single-level model where for a high switching ratio a large change in both the effective coupling and in the distance between E_F and the closest MO is desirable.

4.1.2 Switches exploiting Baird's rule on excited state aromaticity and antiaromaticity

In chemistry the concept of aromaticity is well-known with the benzene ring as the archetype aromatic species with six π-electrons in the ring. Whether a compound is aromatic or antiaromatic in the ground state is determined by what is called Hückel's rule [101], where a cyclic fully π-conjugated hydrocarbon (annulene) with 4n+2 π-electrons (n = 0, 1, 2, ...) is aromatic while an annulene with 4n π-electrons is antiaromatic. Even though the concepts of aromaticity and antiaromaticity ((anti)aromaticity) are essentially applied exclusively for the ground state, Colin Baird, showed in 1972 by usage of perturbation molecular orbital (PMO) theory, that the concepts can be applied also in the lowest $\pi\pi^*$ excited triplet states (T_1 states) of simple annulenes [102, 103], where it was found that the character of the T_1 state is the reversal of Hückel's rule for S_0 state. Recently, it has been shown that Baird's rule is also applicable to the S_1 state [104–106].

New families of molecular conductance switches could be found by designing compounds that are aromatic in their ground (S_0) states, thus, by excitation to the S_1 and T_1 states they will be antiaromatic, a destabilizing feature that the compounds may diminish through structural rearrangements. Such structural rearrangements could in our view be useful as bases for optical conductance switches, provided the molecules can be designed so that the rearrangement leads from a less conducting to a highly conducting isomer. Thus, it should be possible to switch some common and readily available compounds between two different isomers (an ON and an OFF state) opening up the possibility for a molecular conductance switch. For example, the indigo dye, 2,2'-*bis*(2,3-dihydro-3-oxoindolyliden), can be switched between two isomers through a double hydrogen shift; one planar isomer with linearly π-conjugated paths and one isomer with a partly cross-conjugated connectivity.

In Paper V we investigate transport properties of the three different families of reactions opening up the possibility for these kinds of optical molecular switches and one "antifuse". The proposed molecular switches are shown in Scheme 4.3, where **4.20**-**4.22** are based on photochemical hydrogen shifts and
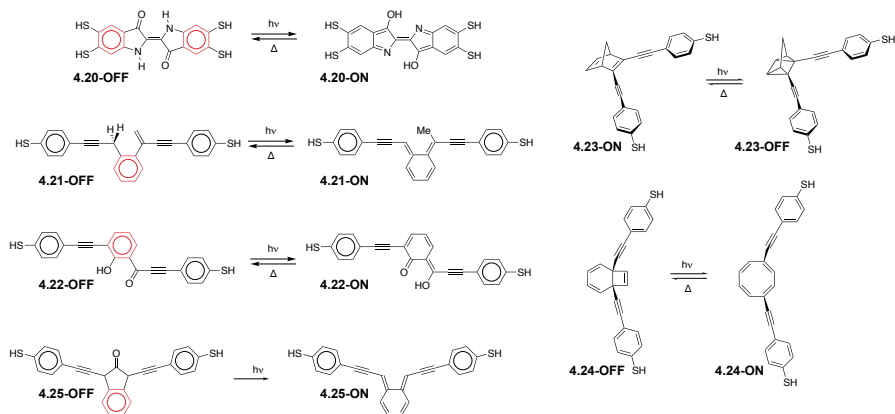
Scheme 4.3: Potential molecular conductance switches where **4.20**-**4.22** are based on photochemical hydrogen shifts, **4.23**-**4.24** are based on photochemical pericyclic reactions and the antifuse, **4.25**, is based on the Norrish Type I reaction, all in which S_1 state aromaticity is gained or S_1 state antiaromaticity is diminished through the photoreaction. For compounds **4.20**-**4.21** and **4.25** the benzene ring which is the core of the photorearrangement of the OFF-state is shown in red.

4.23-**4.24** are based on pericyclic reactions. Furthermore, the antifuse, **4.25**, is based on the Norrish Type I reaction. Here it should be noted that the presently investigated switching systems represent templates for further design and not the final switches. *E.g.*, modes for increasing the thermal stability in the ON-states of switch candidates **4.20** - **4.22** with *ortho*-xylylene fragments need to be addressed.

The two isomers for each compound were attached to gold electrodes and the transport characteristics were calculated in the framework of DFT. In Fig. 4.4 the zero-bias transmission for the OFF (left panel) and ON (right panel) states of the different proposed switches are shown. The results for the zero-bias conductance together with switching ratios (SR) at $V = 0$ and the length of the compounds (S$\cdots$S distance) are collected in Table 4.3.

Comparing the hydrogen shift with the pericyclic reaction, the higher SRs are found in the first one, where especially **4.21** and **4.22** have high SRs. The high SRs for these compounds can be explained by, when introducing conjugation for the ON-state, now the HOMO is shifted closer to E_F and in the same time the HOMO-LUMO gap is decreased to give high transmission over the whole considered energy range. For the OFF-states of **4.21** and **4.22** the HOMO-level is about 0.5 eV below E_F and localized to the cross-conjugated segments with a very weak connection through the central part of the molecule. On the other hand for the ON-state, the HOMO is shifted closer to E_F and the conjugation delocalizes the orbital over the complete molecule

Table 4.3. *Conductance characteristics of switches*

Compound	Conductance[a] (G_0)	SR[b]	S$\cdots$S distance[c]
4.20-ON	8.7×10^{-1}	27	13.5
4.20-OFF	3.4×10^{-2}		13.5
4.21-ON	3.4×10^{-1}	1175	20.6
4.21-OFF	2.9×10^{-4}		20.7
4.22-ON	6.6×10^{-2}	548	20.9
4.22-OFF	1.2×10^{-4}		20.8
4.23-ON	2.8×10^{-1}	47	12.0
4.23-OFF	6.1×10^{-3}		11.7
4.24-ON	5.9×10^{-3}	5	11.4
4.24-OFF	1.1×10^{-3}		12.2
4.25-ON	2.8×10^{-1}	623	20.40
cis-**4.25-OFF**	4.5×10^{-4}		19.42
4.25-OFF	6.3×10^{-4}	450	19.42

[b] Conductance at zero bias (0 V).
[b] Conductance ON/OFF switching ratio at zero bias (0 V).
[c] Distance between thiol end-groups [Å] .

and the LUMO-level is now also closer about 1 eV above E_F. Thus, for **4.21** and **4.22** we have both a shift of the most conducting level closer to E_F and a delocalization of the level over the complete molecule when going from the OFF-state to the ON-state which was seen in the previous section to give a high switching ratio. The overall conductance of both the OFF and ON-states of **4.22** is lower compared to the corresponding states of **4.21**, and it is known that *meta*-substituted benzene as in compound **4.22-OFF** has a lower transmission compared to *ortho*-substituted [107]. This is due to interference effects, here seen in **4.22-OFF** as a deep antiresonance about 1 eV above E_F. For **4.22-ON** the lower conductance can be explained by the cross-conjugated segment disrupting the linear conjugation through the *ortho*-xylylene unit. This can be seen in Figure 4.5 where the local currents in **4.21-ON** and **4.22-ON** are shown. For **4.21-ON** there are two well-conducting linear conjugated paths through the central *ortho*-xylylene unit, while for **4.22-ON** the shorter path is disrupted and the current follows the longer conjugated path.

The third switch based on hydrogen-transfer is **4.20**, here the central unit is different and it is anchored with two thiols group on each side to the gold electrodes. The transmission of the ON-state shows a much more intricate behavior compared to previous compounds, where interference effects from multiple current paths through the molecule both from doubly anchoring it, as well as from the cross-conjugation in the OFF-state. In the ON-state the strong coupling between the HOMO and the electron states in the electrodes gives a broad peak in the density of states (DOS) in resonance with E_F, thus, giving
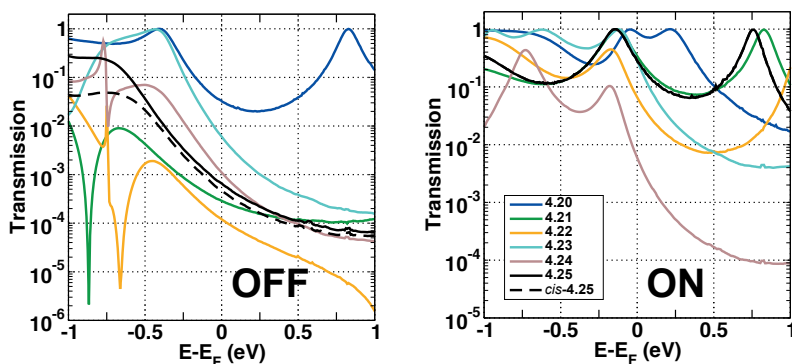
Figure 4.4. Transmission spectra (V=0) for all switches in OFF (left) isomers and ON (right) isomers.

close to ballistic transport. The small dip in the transmission at energies just above E_F corresponds to the small HOMO-LUMO gap. The HOMO-LUMO gap for **4.20-OFF** is larger, but still small compared to the other compounds (~ 0.9 eV), furthermore the delocalization of the orbitals and the coupling to the electrodes is not changed compared to **4.21-ON**, resulting in a high transmission also for the OFF-state, giving this switch a moderate ON/OFF ratio of thirty.

Both switches based on the pericyclic reaction (**4.23** and **4.24**) show similar characteristics with a broad peak in the DOS from the HOMO, close to the Fermi level, E_F, and only with a small shift compared to the OFF-state, thus giving similar transmission for both the ON and OFF states. Thus, the small shift of the HOMO together with a moderate change in the coupling between the level and the electrodes results in low SRs for both **4.23** (SR=47) and **4.24** (SR=5).

The last considered compound, **4.25**, is not a switch but could more be considered as an antifuse. Here the OFF-state is a molecule with the current path disrupted by two sp^3 hybridized C atoms. The photoinitiated decarbonylation leading to the conducting **4.25-ON** state can be viewed as a result of two photochemical processes; (*i*) the double α-cleavage (Norrish Type I) of the C-C bonds adjacent to the carbonyl group, and (*ii*) a way for the S_1 and T_1 state antiaromatic benzene ring to alleviate its destabilizing antiaromaticity.The linear conjugation introduced in **4.25-ON** increases the transmission, and the results is very close to **4.21-ON**, except that without the methyl substituent at one of the C atoms of the exocyclic C=C bonds, LUMO is shifted minutely closer to E_F. Depending on whether one considers the *cis-* or the *trans*-isomer of **4.25-OFF**, the ON/OFF ratio is either about six-hundred or four-hundred fifty. The *cis*-**4.25-OFF** isomer is the least conducting according to our calcula-
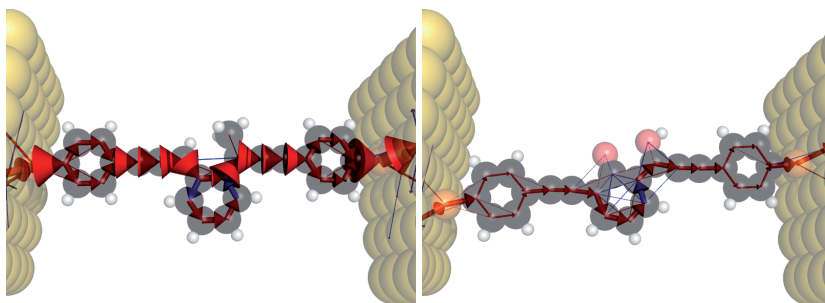
Figure 4.5. Local currents in **4.21-ON** (left) and **4.22-ON** (right), where the cross-sectional area of the cylinder is proportional to the current density. Red currents represent positive transport direction, and blue currents represent negative direction. The currents are calculated at the Fermi energy $((\mu_L + \mu_R)/2)$, but a small positive bias voltage is assumed for computational purposes. For a full derivation see Okabayashi et al.[108] and Paulsson and Brandbyge[109]. In order to become visible, the local currents in **4.22-ON** is magnified, two times compared to **4.21-ON**.

tions. Herein, we considered both the *cis-* and *trans-*isomers of **4.25-OFF** as it is unclear whether the decarbonylation will progress stepwise or concerted.

To conclude this section we have studied several types of molecular conductance switches, where the switching is induced by exciting the molecule and changing the aromaticity, which induce a rearrangement. Overall, the switches based on hydrogen shifts are preferable over the switches based on pericyclic reactions, where for the ON-states, **4.24-ON** is by far the worst conductor. Depending on the wanted characteristics of the switch, different compounds would be the choice, if a high ON-current is the most important **4.20** would ideal but with the drawback of rather moderate ON/OFF-ratio. If instead a high ON/OFF-ratio is wanted **4.21** is the best choice, with good characteristics both with a rather high ON-current and with a low leakage current in the OFF-state. On the other hand, to minimize the leakage-current **4.22** would be better but coming with lower ON-current and ON/OFF-ratio compared to **4.21**.

4.2 Mechanically controlled switches

In the last section we investigate a family of stereoisomerization switches that under elongation, without breaking or changing any bonds, change their conductance.

These switches belong to the mechanochemistry area where chemical manipulations occur by exerting mechanical force on a chemical structure [110, 111]. Earlier mechanochemical studies have focused either on the breaking of covalent bonds [112–114] or on the tuning of molecular levels in a static

chair(eq,eq)
A,A' = eq, eq
B,B' = ax, ax
horizontally long structure

twist
A,A' = eq, ax
B,B' = ax, eq

chair(ax,ax)
A,A' = ax, ax
B,B' = eq, eq
horizontally short structure
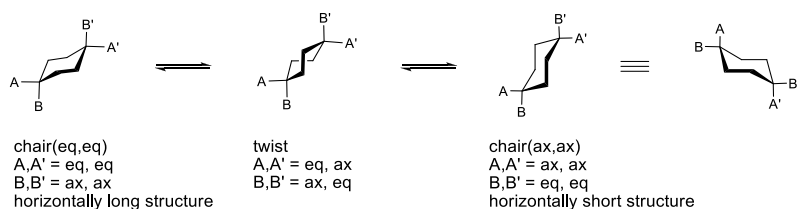
Figure 4.6. The conformational change of a cyclohexane ring (pseudorotation) going from the chair conformer with substituents A and A' in equatorial positions, passing a twist conformer, leading to the chair conformer with the substituents A and A' in axial positions. Going from left to right, the pseudorotation leads from a horizontally long structure to a horizontally short one.

molecule by changing the contact geometry between the molecule and the electrode [115–117].
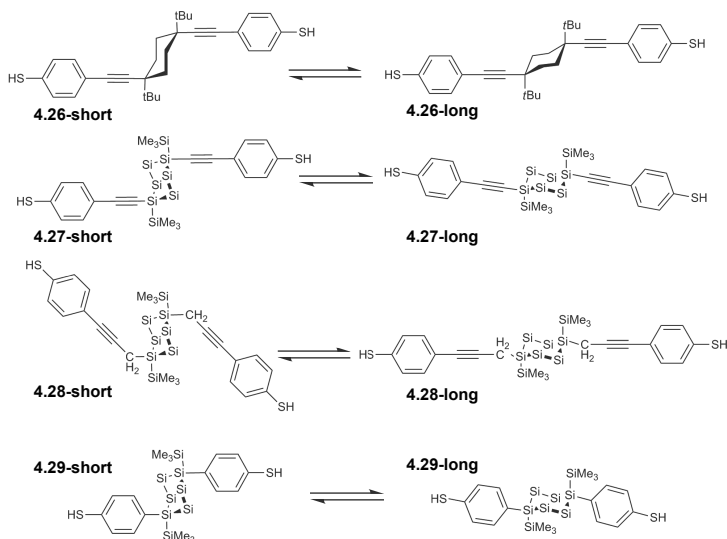
Scheme 4.4: Potential molecular conductance mechanoswitches.

In Paper VI we have investigated compounds with cyclohexa(sila)ne cores, that would constitute a new mechanochemical functionality since this core can be interchanged between short and long structural states without breaking bonds (see Fig. 4.6). Cyclohexasilanes are "heavy" cyclohexanes with the six carbon atoms exchanged to silicon. These compounds are saturated similar as the cyclohexanes, but because of the σ-conjugation within the Si-framework [118, 119] as well as the smaller energy differences between the cyclohexasilane frontier-orbitals and the π-orbitals of unsaturated substituents, the configurational and conformational electronic structure variations could be larger than in analogous cyclohexanes.

51

In this paper we have investigated both the isolated properties as well as transport through the cyclohexasilanes when connected to gold electrodes. The compounds we have considered for transport calculations are shown in Scheme 4.4 as their long and short structural states, where the different systems are connected to the gold electrode surfaces via thiophenol substituents. A full discussion of the properties for the isolated cyclohexa(sila)nes are given in Paper VI.
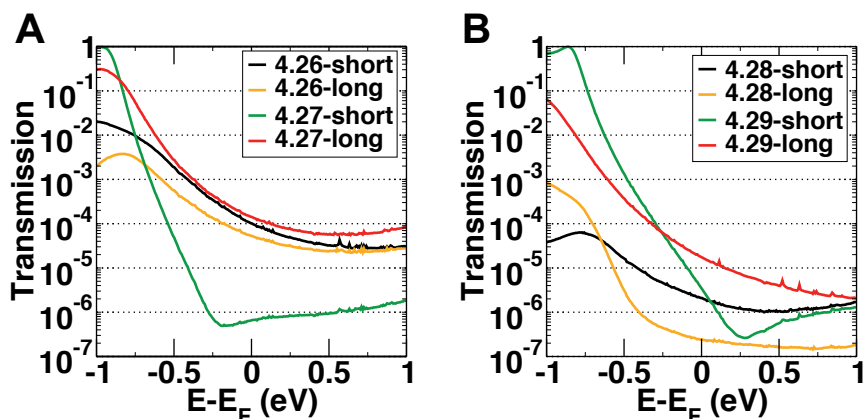
Figure 4.7. Calculated transmission spectra (at V = 0), left panel (**A**) showing results for the different conformers of **4.26** - **1** and right panel (**B**) showing results for the different conformers of **4.28** and **4.29**.

Table 4.4. *Calculated single-molecule conductance (at V = 0), the* $S\cdots S$ *distance and the conductance ratio between the long and the short conformers (ON/OFF) for the thiophenol-gold connected molecules (see Scheme 4.4).*

	$r(S\cdots S)$ (Å)	Transmission (V=0) $[G_0 \times 10^{-4}]$	ON/OFF (long/short)
4.26-short	18.1	1.01	0.52
4.26-long	19.3	0.53	
4.27-short	19.1	0.0066	215
4.27-long	21.7	1.42	
4.28-short	22.2	0.020	0.1
4.28-long	22.8	0.0024	
4.29-short	14.8	0.035	5.1
4.29-long	17.1	0.18	

To investigate the difference when going from cyclohexanes to cyclohexasilanes we compare the conductance characteristics (Figure 4.7) of compound **4.26** and **4.27**, where we find a significant difference. In the case of **4.26**, the
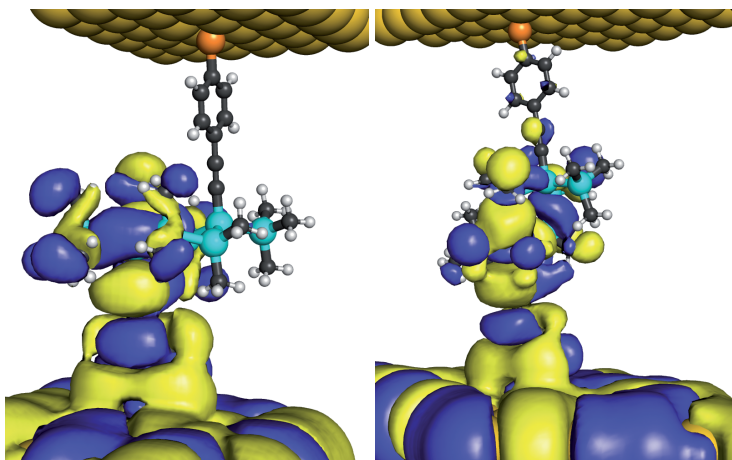
Figure 4.8. Visualization of the most transmitting eigenchannel wave function (incoming from the bottom electrode) at the Fermi energy the short (left) and long (right) conformer of **4.27**. The isosurfaces of the eigenchannel wave function are colored according to phase and sign, the positive/negative real part being colored in blue/yellow (the imaginary part is below the cutoff value and not visible), both junctions plotted with the same isovalue to be comparable.

shorter conformer, **4.26-short** is somewhat more conducting than the longer **4.26-long**. This is as expected based on the fact that ε_{HOMO} did not vary between the conformers, thus, the small difference in conductance can be assigned to altered tunneling length. In contrast, for cyclohexasilane **4.27** we find that the **4.27-long** conformer is substantially more conducting than the shorter **4.27-short** (Figure 4.7A). This increase in conductance is counterintuitive if one assumes that the tunneling length dominates the conductance strength, as for **4.26**. It can be assumed that the orbitals which are most important for transport are those located on both the central ring and the π-substituents, and indeed, in the study of the isolated compounds an increase in the frontier orbitals onto the phenyl groups when elongating the molecule from **4.27-short** to **4.27-long** was found. This is also seen in the most transmitting eigenchannel for the two conformers shown in Figure 4.8. For **4.27-short** (left panel) it is found that chair(ax,ax) structure of the central ring introduces a disruption in the conduction path and the incoming wave is mostly reflected in the central part. On the other hand, for **4.27-long** there is no such disruption and the transmission channel has a lot of density on the whole ring-structure as well as on the substituents on the other side. Thus, a good communication between the central σ-conjugated system and the two π-conjugated substituents are important for high conductance.

To disrupt the interaction between σ- and π-conjugated segments of **4.27** we inserted methylene moieties, leading to **4.28**, and this reduced the conductance dramatically. Additionally, it reverses the ON/OFF ratio making the

shorter conformer the more conducting one (Figure 4.7B), *i.e*, the tunneling length now determines. The communication between the σ- and π-conjugated segments can also be decreased by removing the ethynyl units and connecting phenyl groups directly to the ring (**4.29**). Although, the longer conformer of **4.29** is more conducting (still better coupling between σ- and π-conjugated segments when elongated), the ratio between the conformers is reduced.
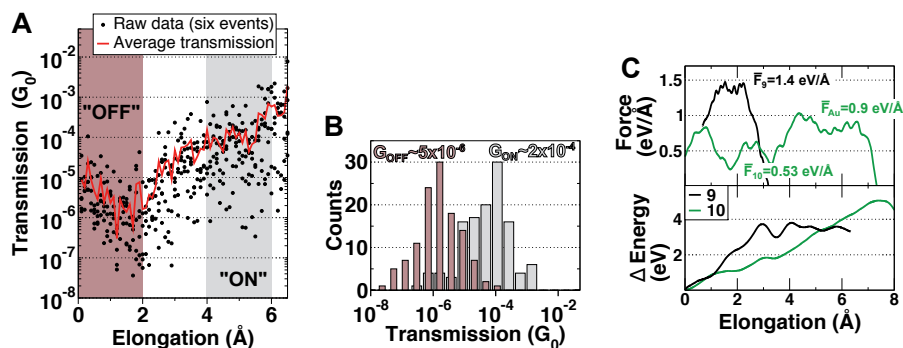
Figure 4.9. Calculated dynamical properties of compounds **4.26** and **4.27**. **A**: Transmission of **4.27**, when elongated in the MD-simulations, black dots show results from six different stretching events and full red line shows average transmission. The "OFF" (brown) and the "ON" (grey) regions define the two different states for a possible mechanoswitch, pseudorotation from *trans*-**4.27**-chair(ax,ax) to *trans*-**4.27**-chair(eq,eq) occurs at about 3 Å. **B**: Histogram with collection of transmission values for the "ON" and "OFF" states of the mechanoswitch defined in **A**. **C**: Force (top panel) and change in energy (bottom panel) when elongating the junctions with **4.26** and **4.27**.

To access the long conformers of the switches **4.26**-**4.29**, mechanical force is necessary, thus to access them in an experiment the MCBJ could be used. The process of MCBJ can be simulated (by the method proposed in Sec. 2.6) resulting in conductance traces as shown in Figure 4.9A for **4.27**, where the dots represent different stretching events. The conductance when stretching the junction is a highly dynamic process with variations of up to 2-3 orders of magnitude. Still, the mean value (full line) of the different stretching events shows a smooth steady increase under elongation, revealing that **4.27** can act as a mechanically controlled switch when attached to gold electrodes. By defining the OFF-state as a less than 2 Å stretched structure and the ON-state as a more than 4 Å stretched structure one can gather conductance values in histograms (Figure 4.9B). The histogram shows a clear distinction of the conductance between the ON ($\sim 5 \times 10^{-6} G_0$) and the OFF ($\sim 2 \times 10^{-4} G_0$) states with a small overlap. From the MD-simulations the force necessary to flip the molecules between different conformers can be estimated as the slope of the energy increase when elongating the junction (Figure 4.9C). When stretching

4.27 two regions in the force is seen, elongation of 2-3 Å requires a force of 0.53 eV/Å (pseudorotation) and elongation more than 3 Å requires a force of 0.9 eV/Å (extraction of gold atoms from the electrode). In contrast, for the more rigid all-carbon species **4.26** the gold-gold bonds break first. However, by constraining the thiol-anchors to the gold electrodes it is possible to estimate that a force of 1.4 eV/Å (0.9 nN) is necessary for pseudorotation of **4.26**. Thus, the longer Si-Si bonds making the cyclohexasilane more flexible, in combination with its rich electronic structure variation between the short and long conformer makes it an interesting compound for applications in mechanochemistry.

To conclude this section we have studied a set of molecules that under a conformational change (without altering the bond structure) changes their conductance. Interestingly, we find that for the cyclohexasilane core the conductance is increased when the molecule is elongated. This can be explain by a delocalization of the conducting orbital from the core in the short conformer to both the core and the substituents connecting the core to the electrodes for the longer conformer. In the case of the more commonly studied cyclohexane this delocalization of the orbital is not seen and the shorter conformer is more conducting compared to the elongated as expected.

In summary, in this chapter we have studied five different families of molecular conductance switches. The switches in the four first families can be activated by light and/or temperature while the last family is activated by mechanical force. In general, we find that to have a high switching ratio, the transition from the OFF to the ON-state should induce a shift of the most conducting molecular orbital closer to E_F, and in the same time increase the effective coupling between the electrodes and the orbital. This can be achieved by having a disruption in the π/σ-conjugation in the OFF-state while in the ON-state having a conjugated path spanning the complete molecule.

5. Molecular cords and spacers

In the preceding chapters a platform for molecular electronics measurements and molecular switches that could act as active elements in devices have been investigated. The missing part now is molecular cords that could wire the switches to the nanoelectrodes in the platform. Despite that an enormous number of differently conjugated molecules and polymers have been synthesized and investigated there is so far no conformationally flexible conjugated molecule with a conjugation which is invariant with conformation [118, 120, 121]. If molecules of such type would be designed they could behave as molecular electrical cords displaying (nearly) the same conductance whichever conformation they adopt.

In microelectronics silicon is still dominating, however, in the field of molecular electronics other types of conjugated molecules are dominating, but conductance through single small oligosilane molecules has recently been explored, both experimentally and computationally [122, 123]. Experiments using the STM break junction technique Klausen et al. revealed that linear oligosilanes show a slow decay of conductance with length, comparable to that of π-conjugated polyacetylene fragments. However, the results also pointed to a strong conformational dependence of the conductance because the investigated pentasilane chain was somewhat less conducting than extrapolated from the decay constants β of the shorter chains.

In this chapter we are going to investigate two routes to decrease the dependence of the conductance on the conformation. In Sec. 5.1 (Paper VII), we study a series of rigid [2.2.2]bicyclic carbosilanes, these are not flexible to act as cords, but could instead be used as rigid molecular spacers with a well-defined conductance. Furthermore, in Sec. 5.2 (Paper VIII) we study oligomers of 1,4-disila/germa/stannacyclohexa-2,5-diene units which are connected via the E atoms (E = Si, Ge, Sn) which could act as molecular wires as the changes in conductance are small when the conformation of the oligomer is changed.

5.1 Influence of number of parallel molecular chains

In this section we are interested to find out how the differences in the electronic and geometric structures of [2.2.2]bicyclic carbosilanes are reflected in the calculated conductances through these molecules (for discussion of the isolated compounds see Ref. [124]). Due to their central cavelike structure, these compounds will in the following be referred to as cages or cage molecules.
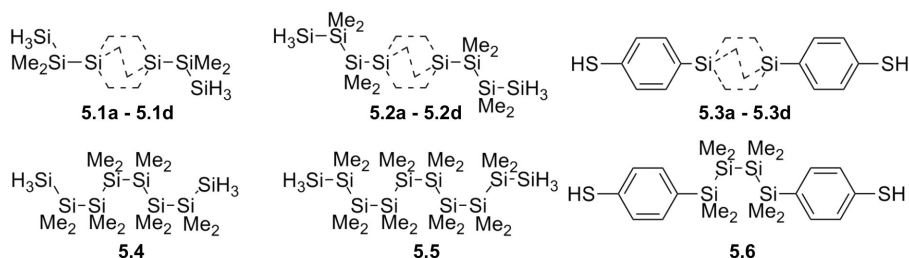
Figure 5.1. Investigated compounds. Compounds labelled **a-d** contain in total three bridges (dashed bond lines), with three (**a**), two (**b**), one (**c**) or zero (**d**) -SiMe$_2$SiMe$_2$- bridges, the others being -CH$_2$CH$_2$-.

To compare the characteristics of the different cages, each cage molecule was anchored to gold electrodes and the conductance was calculated using DFT combined with NEGF. The investigated cage molecules **5.1** - **5.3** and their open-chain analogs **5.4** - **5.6** are shown in Fig. 5.1. We consider the compounds to be anchored to the gold electrodes either via silyl (SiH$_3$) groups (**5.1a** - **5.1d**, **5.2a** - **5.2d**, **5.4** and **5.5**), which allow for direct contact between the σ-bonded silicon framework and the Au electrodes, or via traditional thiophenols (**5.3a** - **5.3d** and **5.6**), which have a mismatch between the conjugation topologies of the terminal and the central molecular segments (π- versus σ- conjugation).

Now, a question is how the existence of one, two and three disilanylene (-SiMe$_2$SiMe$_2$-) bridges, the others being ethanylene (-CH$_2$CH$_2$-), influences the conductance of these cages? Using standard circuit theory, *i.e.*, Kirchoff's law, the net conductance from parallel paths equals the sum of the individual conductances. However, interference effects have long been noticed in transport through molecules with parallel paths [99, 125], *e.g.*, in bicyclo[2.2.2]octa-2,5,7-triene (barrelene) [126]. Several studies have found constructive interference when multiple paths are available through the junction, for example Reuter et al. have studied cross-talk between two molecular wires and found an increased conductance, more than what was expected by summing up the conductance of the two [127]. Thus, is the general trend in single-molecule junctions always that constructive interference increases the conductance non-linearly when additional current paths are made available?

We start by comparing the conductance for the analogous cage compounds having different types of anchoring groups, where it is found that the transmission for the compound with the σ-conjugated silyl anchors (**5.1a**) is about two orders of magnitude larger than the compound with π-conjugated thiophenol anchors (**5.3a**). This manifests the need for proper match between the orbital character of the anchoring groups and the conjugation type of the main part of the molecule for high conductance [122, 128]. Thus, because of the poor
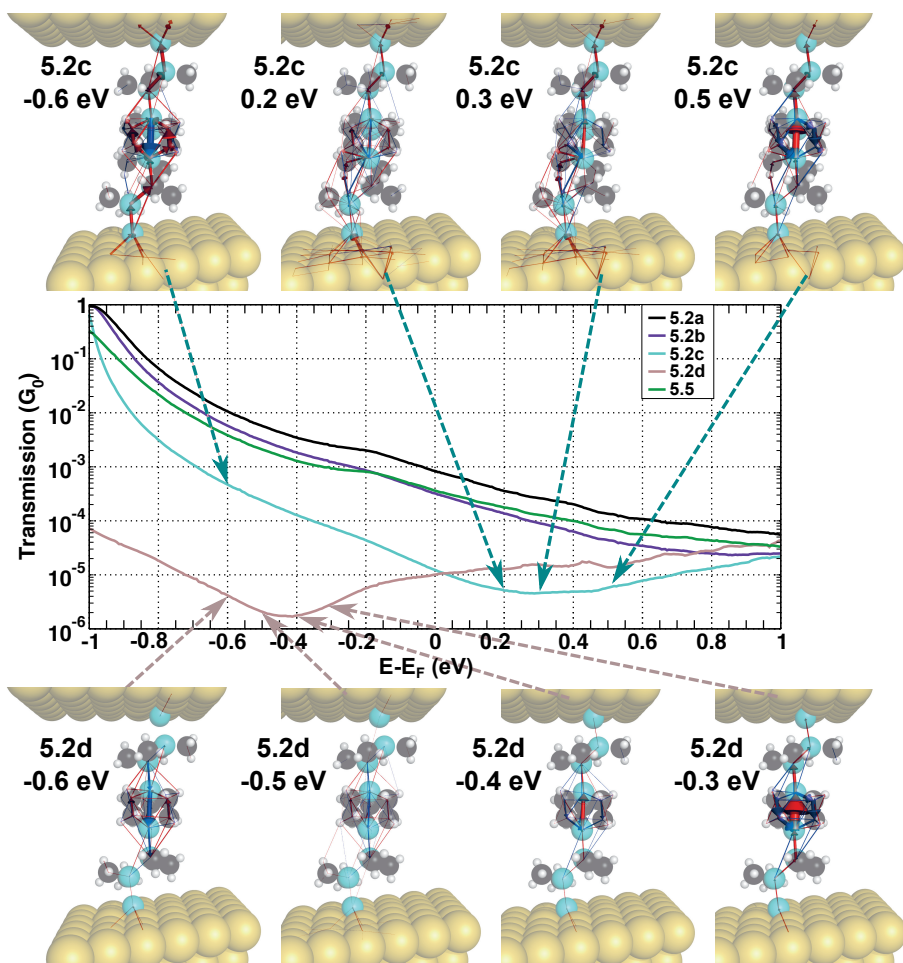
Figure 5.2. Transmission spectra (V = 0) for cage compounds with H_3Si-$SiMe_2$-$SiMe_2$ anchoring (**5.2a**-**5.2d** and **5.5**), together with local currents in compounds **5.2c** and **5.2d** plotted at different energies. The energy at which the currents are plotted is given at each plot and marked in the transmission spectra with a dashed line. Note the reversal of the ring currents in the central part going from 0.2 eV to 0.3 eV for **5.2c**, at 0.25 eV the currents in the central part almost vanish. For **5.2d** the reversal of the ring currents in the central part occurs when going from -0.5 eV to -0.4 eV.

performance of the thiophenol anchored carbosilanes, we concentrated on the compounds with silyl anchor groups. This also places the focus on the central topic of this study, *i.e.*, the differences in conductance between the four cages

Furthermore, the twist of the cage, due to the shorter -CH_2CH_2- than -$SiMe_2SiMe_2$- bridges in **5.1b** and **5.1c**, opens up for injection of electrons directly from the electrode to the bridge. Hence, the current does not go through the anchor groups as for **5.1a** and **5.1d**, respectively, and as a consequence, the effective tunneling length is shorter lowering the resistance of **5.1c**.

In order to overcome the problem with injection of electrons directly from the electrodes to the central bridge we inserted an extra $SiMe_2$ segment as spacer on each side of the cage so as to increase the distance between the cage and the electrodes (**5.2a**-**5.2d**).

Considering the values of the transmission of **5.2a**-**5.2d** and **5.5** (Figure 5.2), the carbosilane cage with three -$SiMe_2SiMe_2$- bridges is the most conducting, as expected. However, if **5.2a** could be described as three resistors in parallel it would be three times as conducting compared to the oligosilane-chain, **5.5**, but it is roughly twice more conducting. Thus, there is destructive interference in the cage lowering the total conductance. Furthermore, one would expect **5.5** and the cage **5.2c**, with only one -$SiMe_2SiMe_2$- bridge, to have similar conductances. But, as seen in Fig. 5.2 the transmission of the cage compound is a factor thirty lower compared to the open-chain compound, and it is barely higher than the all-carbon cage **5.2d**. Hence, having more than one bridge, and especially if they are of different types, introduces destructive interference in the cage which can give large modification to the total transmission.
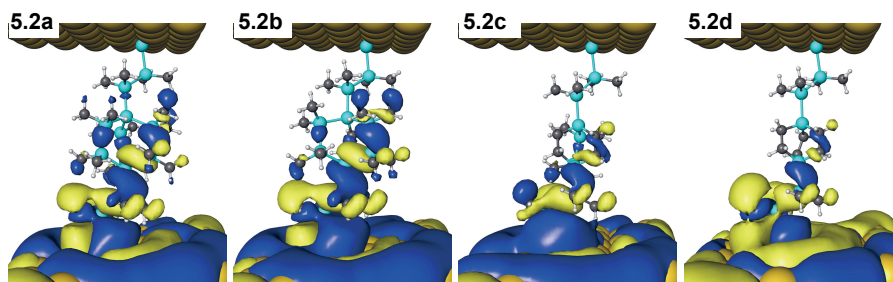
Figure 5.3. Visualization of the most transmitting eigenchannel wave function (incoming from the bottom electrode) at the Fermi energy for the different compounds (**5.2a**-**5.2d**). The isosurfaces of the eigenchannel wave function are colored according to phase and sign, the positive/negative real part being colored in blue/yellow (the imaginary part is below the cutoff value and not visible), and all junctions plotted with the same isovalue to be comparable.

With regard to the eigenchannels (Fig. 5.3), all four channels are similar although there is one large difference because for **5.2a** and **5.2b** the main lobes of the most conducting channel are located on one of the -$SiMe_2SiMe_2$-

bridges while for **5.2c** and **5.2d** the main lobes are located on one of the -CH_2CH_2- bridges. When comparing this to the electronic structure described earlier for the isolated carbosilane cage molecules, the most conducting channels of **5.2a** and **5.2b** and **5.2d** show clear resemblance with the HOMO of the systems. In contrast, for **5.2c** the most conducting channels goes through HOMO-2. Neither the orbitals of the isolated molecules nor the most conducting channels are distributed equally over the three bridge segments, and there is significant communication between the various bridges resulting in destructive interference in the cage molecules. As a result, the different bridges can not be regarded as independent current paths, and it is not possible to view the cages as composed of three equal resistors in parallel.

In conclusion, we have investigated the electronic structure and transport properties of a set of compounds containing central silicon cage segments, and their carbon analogues. In general, we find that when the central part of the molecule is σ-conjugated, having σ-bonded anchoring groups gives higher total conductance when compared to π-conjugated anchor groups. Furthermore, we find that the three bridges can not be seen as independent current paths, instead we find significant destructive interference lowering the total conductance. In the case of **5.2a**, the three tetrasilane segments provides only about a factor two increase in the conductance when compared to the corresponding linear oligosilane **5.5** with one tetrasilane segment. However, since the investigated carbosilane cage molecules have less flexible structures, they may still show a potential as rigid molecular spacers.

5.2 Conformer-independent molecular wires

Macroscopic electrical cords conduct equally well at every "conformation" they can adopt. For a molecule to behave as a cord there should be only a minute change in the frontier orbitals (both in spatial distributions and orbital energies) as one rotates about the single bonds of this molecule and as the molecule is compressed or stretched[1]. Here we propose that the conformational variations in the orbitals can be reduced by connecting 1,4-disilacyclohexa-2,5-diene units via the Si atoms as this leads to conformationally flexible oligomers with large primary hyperconjugative overlap between local adjacent σ(Si-Si) and π(C=C) orbitals, but small secondary orbital overlap between non-adjacent local orbitals on different monomer units. If this interaction is strong it leads to linearly hyperconjugated paths which stretch from one end of the molecule to the other.

---

[1]Here it should be noted that there is, however, not a one-to-one correspondence between macroscopic electrical cords and our molecular electrical cords as a macroscopic cord, besides a high structural flexibility and a "conformer-independent" conductance, is composed of two parallel wires insulated from each other.

R = Me $n = 0$ **5.7a**   R = SiH$_3$ $n = 0$ **5.7b**
        $n = 1$ **5.8a** $n = 1$ **5.8b**
        $n = 2$ **5.9a** $n = 2$ **5.9b**

R = SiMe$_3$ $n = 0$ **5.7c**
            $n = 1$ **5.8c**
            $n = 2$ **5.9c**

E = Ge **5.10**
E = Sn **5.11**

Figure 5.4.   The investigated oligomers of 1,4-disila/germa/stanna/cyclohexa-2,5-dienes with methyl (**5.7a** - **5.9a**), silyl (**5.7b** - **5.9b**), and TMS (**5.7c** - **5.9c**) groups as the substituents R at 1- and 4-positions of the monomers.

The geometries and ground state potential energy surface of dimers, trimers and tetramers of 1,4-disilacyclohexa-2,5-dienes (**1** - **3**), having different substituents R at the 1- and 4-positions of the monomers (R = Me, (**a**), SiH$_3$ (**b**) and SiMe$_3$ (TMS) (**c**)), as well as a few 1,4-digerma- and 1,4-distannacyclohexa-2,5-dienes with TMS substituents (**5.10** and **5.11**) were investigated by computational means (Figure 5.4). Discussions about the ground state potential energy surfaces, geometries and variations in frontier orbital energies are given in Paper VIII, here the focus will be on the conductance properties of these suggested cords. As was shown in the previous section (and Paper VII), matching the conductance between the central part of the molecule and the anchoring group is important for high conductance, thus, we use the silyl-group again for anchoring the cords to gold electrodes, this time with two silyl-groups on each side.

The calculated zero-bias conductance of **5.9a** (Figure 5.5A) shows a small variation between the three stable conformers obtained in the ground-state calculation, where the $a_\pm a_\pm a_\pm$[2] conformer has the highest conductance. The $a_\pm g_\pm a_\pm$ and the $g_\pm g_\pm g_\pm$ conformers are, respectively, factors four and twenty

---

[2]For the nomenclature used see: Michl, J.; West, R. Conformations of Linear Chains. Systematics and Suggestions for Nomenclature. Acc. Chem. Res. **2000**, 33, 821-823. In brief, the conformations (Si-Si-Si-Si dihedral angles in parentheses) are called *anti* ($\sim 180°$), *transoid* ($\sim \pm165°$), *deviant* ($\sim \pm150°$), *eclipsed* ($\sim \pm120°$), *ortho* ($\sim \pm90°$), *gauche* ($\sim \pm60°$), *cisoid* ($\sim \pm40°$), and *syn* ($\sim 0°$).
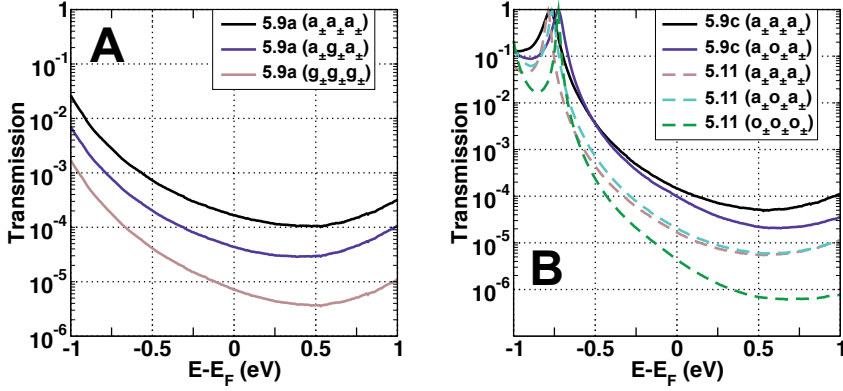
*Figure 5.5.* Transmission spectra (V = 0) for the tetramers **5.9a** (A) and **5.9c** and **5.11** (B).

less conducting than the all-*anti*-conformer. Even though the gold electrode-electrode distance is shorter for the two conformers with *gauche* kinks, the actual lengths of the current paths in the chains are similar in all three conformers. Thus, the difference in conductance between the conformers should be due to weakened conjugation as a result of *gauche* conformers. The zero-bias conductance of **5.9c** (Figure 5.5B) differs less between the two calculated conformers $a_\pm a_\pm a_\pm$ and $a_\pm o_\pm a_\pm$, with that of the $a_\pm o_\pm a_\pm$ conformer somewhat lower. Here only two conformers are calculated due to the high rotational barrier away from the all-*anti*-conformer due to steric bulk of the TMS-groups.

To decrease the steric hindrance the central Si-atoms are exchanged for Sn (elongating the bonds between each unit) in **5.11**. Here a similar behavior to that of **5.9c** (Figure 5.5B) is found with the conductances of the two $a_\pm a_\pm a_\pm$ and $a_\pm o_\pm a_\pm$ conformers being very similar despite that they have a difference in electrode-electrode distance of 4 Å. The less steric bulk in **5.11** makes it also possible to calculate the $o_\pm o_\pm o_\pm$ conformer and it has roughly a factor four lower conductance than the two other conformers. When comparing the two TMS-substituted tetramers it is noteworthy that the conductance of the $a_\pm a_\pm a_\pm$ conformer of **5.11** is about a factor eight lower than the value of the corresponding conformer of **5.9c**.

To probe if these oligomers are suitable as cords, the dynamical behavior during stretching or compression is important. So far we have only considered transport through the relaxed conformers. To investigate how the oligomers would act under thermal fluctuations around the ground state we used the method proposed in Section 2.6 to compute the conductance for the dynamic cord. Here we are only interested in the behavior of the oligomers, thus, the atoms in the gold electrodes as well as the four anchoring Si-atoms are kept

fixed during the simulations so as to remove the effects of changes in the Au-Si interaction.

First we consider the junction with static electrode-electrode distance where the conductance is calculated under 6 ps, saving the conductance value every 60 fs (in total 100 points), for **5.9a** and **5.9c**. The conductance is rapidly fluctuating with the conformation of the chain, and for **5.9a** we obtain a mean conductance of 1.44×10^{-4} G_0 with a standard deviation (σ) of 1.04×10^{-4} G_0, the magnitude difference between the calculated max and min values is approximately a factor thirty. For **5.9c**, we obtain in the same way a mean conductance of 1.21×10^{-4} G_0 with a σ of 1.13×10^{-4} G_0. However, here the max and min conductances differ by about a factor 100.
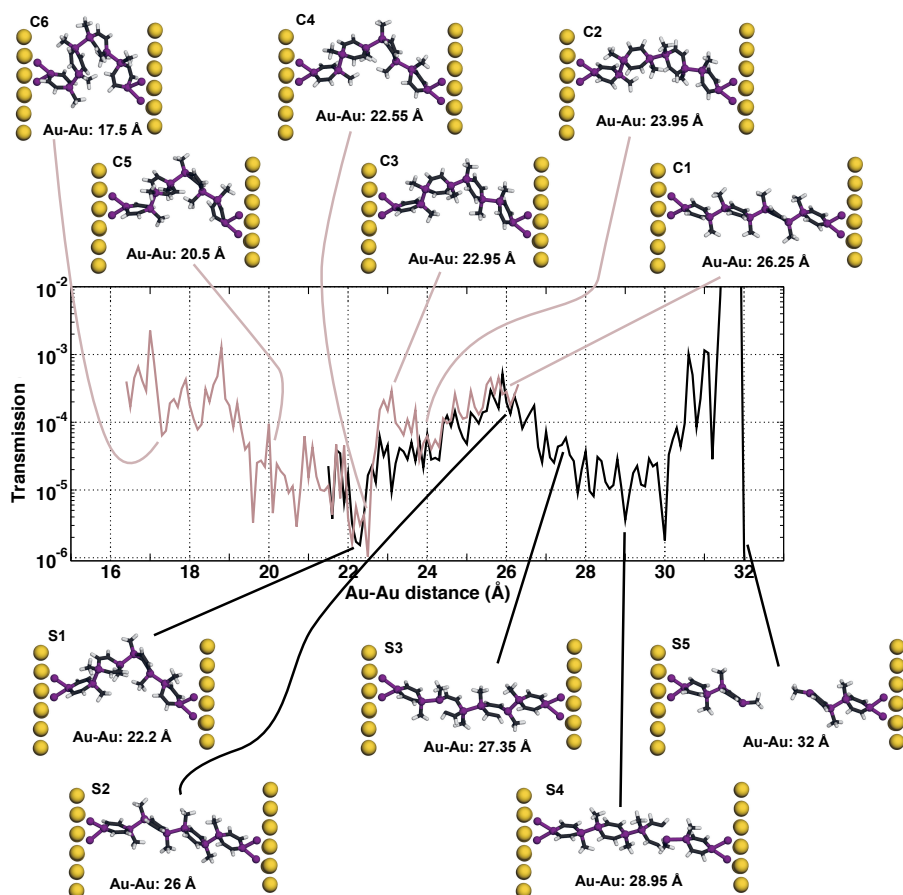
Figure 5.6. Calculated zero-bias conductance when compressing (brown lines) or stretching (black lines) the junction with **5.9a** together with snapshots of the geometry in the molecular junction simulated using DFT-based molecular dynamics.

64

Furthermore, when we stretch or compress the junctions we find that the conductance of **5.9c** is reasonably stable for a wide range of Au-Au distances ($\sim 21 - 29$ Å), where a ratio of 34 is obtained between the max and min conductance values. The variation here is smaller compared to the case with the static junction of **5.9c**, this is due to that a smaller configurational space is explored in the stretching/compressing process. Thus, larger fluctuations can be expected here as well, but the mean conductance is almost constant over the whole considered range. For **5.9a** the conductance drops about a factor ten when moving away from the optimal geometry of the $a_{\pm}a_{\pm}a_{\pm}$ conformer, both by compression and stretching. Here, the mean conductance can be seen as stable in a much smaller range of Au-Au distances ($\sim 23 - 27$ Å), where the ratio between the max and the min conductance is about 60. For a more detailed analysis of **5.9a**, the conductance trace when stretching and compressing the junction together with some snapshots from the geometries obtained are shown in Figure 5.6.

The compression starts from the relaxed geometry in an all-*anti* conformation, and the first snapshot after 120 fs (C1) is very close to this geometry. When the junction is further compressed the central rings are rotated decreasing the conductance, and in C2 a $t_{\pm}t_{\pm}a_{\pm}$ conformer is obtained. Compressing further there is a sudden jump in the conductance between C3 and C4 going from the $a_{\pm}e_{\pm}t_{\pm}$ ($e_{\pm} = 133°$) conformer to a $t_{\pm}e_{\pm}d_{\pm}$ ($e_{\pm} = 117°$), showing that small rotations away from the all-*anti* conformer can have great impact on the conductance. When compressing further, the conductance starts to increase again, and as seen in C5 and C6 there is an increased overlap between the π-orbitals on adjacent rings. The stretching starts from a slightly compressed geometry, and as seen the first snapshot from the stretching (S1) is very close to C4. Stretching further, the Au-Au distance of S2 is close to the relaxed Au-Au distance and here the geometry is very close to the all-*anti* conformer, showing the reproducibility. Stretching beyond this point, at first it is the C-Si bonds inside the ring that are strained (S3, S4), but at last it is the central Si-Si bond that breaks (S5).

In conclusion, we have studied the conductance of some different compounds that may have potential to act as molecular coords. The conductance of the relaxed structures shows conductance variations up to a factor twenty. Using MD-simulations obtaining structures further away from the relaxed structures increases the conductance fluctuations somewhat, still **5.9c** shows a stable mean conductance over a difference of 9 Å in electrode-electrode distance. Although the compounds reported herein are not ideal for molecular electrical cords the results point to a direction for future molecular design.

In this chapter we have studied two different compound classes that may function either as rigid molecular spacers with a well-defined conductance or as molecular cords. In both cases we find that it is of great importance to match the conjugation of the anchoring groups with the molecular backbone for high

conductance. For the cage compounds we have a molecular structure with three pathways for conduction, and opposite to what could be expected from Kirchoff's law for conventional electronic devices, we only see an increase in conductance by a factor two when compared to similar molecules with a single conduction pathway. For the proposed molecular cords we find conductance variations in the range of a factor 50-100, and that the mean conductance is reasonable stable over almost 9 Å of different electrode-electrode distances.

6. Diamond electronic devices

Diamond has many properties that make it an advantageous alternative to more conventional group IV, III−V and II−VI semiconductors in many high performance electronic applications. Examples of such attractive material properties include: the highest thermal conductivity, the highest electrical breakdown field and high carrier mobilities. In addition, diamond exhibits unique mechanical, chemical and optical properties, including exceptional hardness, chemical stability and a wide electromagnetic radiation transparency range, ranging from deep UV to the far infrared. Although the development is still at a very early stage, these properties together with recent advances in chemical vapour deposition (CVD) diamond growth have enabled the demonstration of some devices with promising future prospects, *e.g.*: high voltage [129] and high temperature [130] diodes, x-ray sensors [131] transfer-doped [132, 133] and delta-doped [134] field effect transistors. Furthmore, spin states in diamond defects or the valley degree of freedom, both of which could be used as a basis for quantum computing [18, 21], are topics that have recently attracted strong attention.

The aim of this part was to model scattering at impurities and/or doping atoms using first principles transport methods, and to correlate these nanoscale properties with macroscopic measurable quantities such as the carrier mobility or resistivity of diamond samples. Due to the large band gap of diamond (5.48 eV), for applications the crystal needs to be doped for example with nitrogen (n-type) or boron (p-type). The doping levels in diamond are in the range of $10^{-15} - 10^{-21}$ cm^{-3}, thus, systems consisting of several thousands of atoms are necessary to model this, which is outside the range of present first principles methods.

In a first attempt, we investigated the carrier effective masses in diamond (Paper IX). These are of great interest for estimating mobility and diffusion in the samples, and particularly the conduction band effective masses are difficult to obtain in experiments due to the low activation of n-type dopants in diamond. Almost 20 years back, an estimation of effective masses based on the linear muffin-tin orbital method (LMTO) using the LDA [135] was made, but in Paper IX we extend the calculations to more accurate methods. To calculate ground-state properties, DFT is a powerful method. Despite the shortcomings of DFT in calculating excitation energies, the Kohn-Sham eigenvalues are often used for discussion of the spectras of solids, even though in the LDA the band-gap is typically underestimated by 30-50%. To overcome these difficulties, we use a dynamically screened interaction, or what is
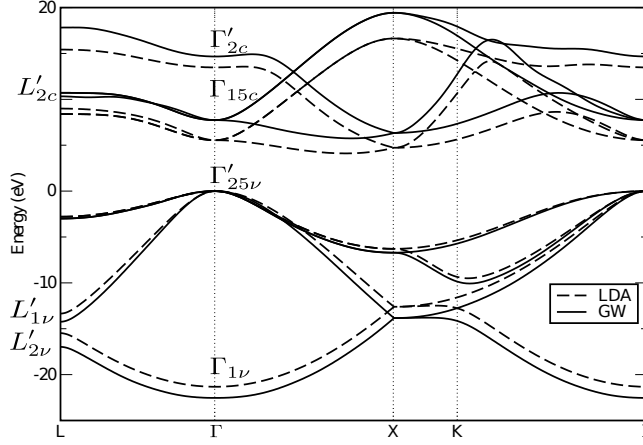
Figure 6.1. Band structure of diamond as calculated from the G_0W_0 calculation (solid line), and standard DFT-LDA including SO-coupling (dashed line).

called the *GW*-approximation [136–138], where the interacting electrons are treated as independent particles responding to an "effective potential". Thus, each electron together with its screening cloud makes up a quasi-particle, and solving for the quasi-particle energies instead gives a better estimate of the band-gaps of solids. The band structure of diamond calculated within the G_0W_0-approximation including the full frequency dependence of the screening using numerical integration (NI), is shown in Fig. 6.1. The band structure from DFT-LDA including spin-orbit (SO)-coupling (PPs parametrized in the HGH-form [139]) is shown as a dashed line to illustrate the bandgap opening.

The effective masses are determined by the curvature of the bands which is affected by including the electron correlations in the GW-approximation. Here we calculate both the masses for conduction electrons at the conduction band minima, located in the BZ at $\frac{2\pi}{a}(0.76, 0, 0)$, and holes in different direction at the valence band maximum at the Γ-point. The results for the effective masses are shown in Table 6.1 where also the previous LMTO(ASA-LDA)-effective-masses by Willatzen et al. are given. The masses calculated via the LMTO-method are consistently larger. For the longitudinal conduction mass the uncertainty is larger due to the strong non-parabolic dispersion along the band at the conduction band minimum. Experimental results for the effective masses have long been lacking due to the difficulties to measure those experimentally but recently, Naka et al. found in experiments using cyclotron resonance values of $1.56m_0$ and $0.280m_0$ for m_l respectively m_t [140]. Furthermore, we expect a ratio of the effective conduction electron masses as $m_l^*/m_t^* = 5.2 \pm 0.1$ [141], which is in agreement with our results.

Accurate effective masses are of great importance for the study of transport in diamond. The effective masses obtained here we use in Paper X where we present theoretical results for the Seebeck coefficient together with other

Table 6.1. *Effective masses in Diamond (in units of the electron mass, m_0)*

	LDA	G_0W_0 (PP)	G_0W_0 (NI)	QSGW	LMTO (ASA-LDA) [135]
$m_{hh}^{(111)}$	0.56	0.67	0.65	0.65	0.778
$m_{hh}^{(100)}$	0.40	0.36	0.36	0.32	0.366
$m_{hh}^{(110)}$	1.34	1.48	1.39	1.64	1.783
$m_{lh}^{(111)}$	0.53	0.67	0.66	0.49	0.778
$m_{lh}^{(100)}$	0.23	0.26	0.26	0.28	0.366
$m_{lh}^{(110)}$	0.23	0.23	0.23	0.29	0.366
$m_{so}^{(111)}$	0.15	0.14	0.14	0.15	0.198
$m_{so}^{(100)}$	0.25	0.23	0.23	0.24	0.466
$m_{so}^{(110)}$	0.18	0.16	0.16	0.16	0.232
m_l	1.3	1.1	1.1	1.2	1.5
m_t	0.25	0.22	0.22	0.22	0.34

transport coefficients in boron doped diamond, to investigate the possibility of diamond-based electronic devices.

To estimate the transport properties we have used the Boltzmann theory [142]. The expression for an electric current, j, in an electric (E) and magnetic (B) field together with a thermal gradient (∇T) can be written in terms of the conductivity tensors as

$$j_i = \sigma_{ij}E_j + \sigma_{ijk}E_jB_k + v_{ij}\nabla_jT + \cdots. \qquad (6.1)$$

From this expression the Hall coefficient, R_H, and Seebeck coefficient, S, can be calculated as

$$R_{ijk} = \frac{E_j^{ind}}{j_i^{appl}B_k^{appl}} = (\tilde{\sigma}^{-1})_{\alpha j}\tilde{\sigma}_{\alpha\beta k}(\tilde{\sigma}^{-1})_{i\beta} \qquad (6.2)$$

$$S_{ij} = E_i(\nabla_jT)^{-1} = (\tilde{\sigma}^{-1})_{\alpha i}\tilde{v}_{\alpha j}, \qquad (6.3)$$

where $\tilde{\sigma}_{\alpha\beta}, \tilde{\sigma}_{\alpha\beta\gamma}$ and $\tilde{v}_{\alpha\beta}$ are the transport tensors which are calculated in the BoltzTraP code as integrals of the different conductivity tensors over the Fermi surface obtained from the electronic structure calculations (a full derivation of the integrals, the conductivity and the transport tensors is found Ref. [143]). The Hall coefficient, R_H, and the Seebeck coefficient, S, are very weakly dependent on scattering in the samples if the relaxation time is isotropic. Thus, in the following we are treating the relaxation time as isotropic but not constant. The relaxation time approximation (RTA) is used where the two main contributions for temperatures below 350 K for p-doped diamond are acoustic phonon (ac) scattering and ionized impurity (ii) scattering. The contribution
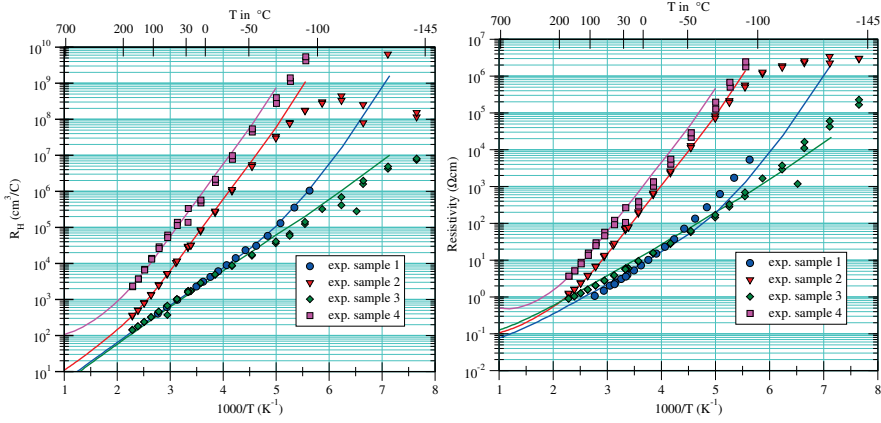
Figure 6.2. Hall coefficient (left) and resistivity (right) versus reciprocal temperature for the four different samples. Measured values are shown with symbols and the theoretical results are shown with full lines. Parameters for the calculations are given in Paper X.

of neutral impurity (ni) scattering has not been included, since good fits to data could be obtained neglecting this mechanism. For ac-scattering we use the expression given in Ref. [144] and for ii-scattering we use the Brooks-Herring [145] expression.

The electronic band structure used as input is calculated for undoped diamond, and to calculate the properties for boron-doped diamond we use the rigid band approximation (RBA) where it is assumed that the electronic properties remain unchanged in the doped regions, which has been validated for diamond [146]. Different doping levels are obtained by shifting the chemical potential, thus, changing the number of free carriers which can be matched to the hole concentration in a p-type semiconductor by the expression given in Ref. [147], if the acceptor (N_A) and compensating donor (N_D) concentrations are known.

The calculated Hall coefficients for different temperatures are shown in the left panel of Fig. 6.2 together with measurements from earlier work [147], and we can see an excellent agreement both when comparing shape and absolute values. The Hall coefficient, R_H, is very weakly dependent on the scattering in the samples and the only parameters used here are the donor (N_D) and acceptor (N_A) concentrations. The obtained values for N_A and N_D for the different samples are close to the measured values, showing that this method combined with the RBA is a valid approximation for all diamond samples considered here. For sample 2 the results deviate at lower temperature due to a transition from impurity band conduction to hopping conduction which is not captured in our models.

The resistivity in the samples, on the other hand, is highly dependent on scattering. This can be used to test different scattering mechanisms in the RTA,
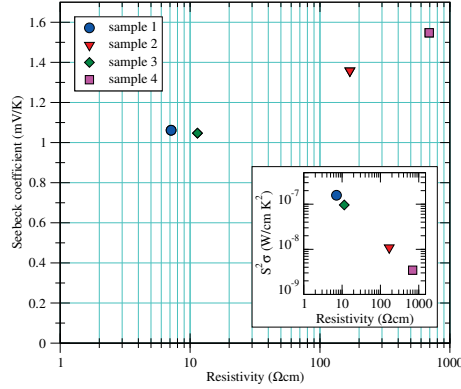
Figure 6.3. Seebeck coefficient and power factor (inset) versus resistivity at room temperature. Only theoretical calculations with parameters given in Paper X.

since everything else is calculated *ab initio* and the doping concentrations are fixed from the Hall coefficient calculations. Our calculated results for the resistivity are shown in the right panel of Fig. 6.2 together with experimental results [147]. For the low doped samples, we find that the ac scattering dominates over the whole temperature range with a small correction by the ii scattering at low temperatures. For the higher doped samples ($> 10^{18}$ cm^{-3}) our model with only ac and ii scattering still reproduces the experimental measurements. This finding is in contrast to the findings of Pernot and coworkers[144], who predicted the effects from scattering by neutral impurities to dominate at room temperature at these doping concentrations. Even the results for the very low compensated ($< 0.01\%$) samples are well reproduced just considering ac scattering. The boron acceptor level, $E_A \sim 0.37$ eV, is deep in the gap and most boron acceptors can be expected to be neutral at room temperature and below, but still the essential results are captured without considering scattering of holes on neutral impurities.

The thermoelectric properties of the four different samples have been theoretically estimated and Fig. 6.3 shows the dependence on the resistivity for the Seebeck coefficient in the samples. All values of the Seebeck coefficient are positive which should be expected from a *p*-type conduction mechanism, here due to the boron acceptors. We find that for single-crystal diamond the thermoelectric power increases with higher resistivity, opposite what the measurements on polycrystalline diamond show. In the inset of Fig. 6.3, the power factor ($S^2\sigma$) at room temperature is shown where we find values in the range 0.004-0.16 μW/cmK^2 for the different samples with decreasing power factor for increasing resistivity. The values are close to these of other good thermoelectric materials, but due to the very large thermal conductivity of diamond, the figure of merit, ZT, will be very low. Still, due to the high mobility in diamond and the possibility to grow low resistivity crystals, diamond is a possible thermoelectric material for applications in harsh environments.

In conclusion, we have accurately calculated the band structure and effective masses for single-crystal diamond. Furthermore, these results have been used in a semi-classical way to calculate some transport properties of boron-doped diamond, such as the Hall coefficient, the resistivity and the Seebeck coefficient. The aim to treat scattering in doped diamond on the nanoscale in a fully *ab initio* way, is still outside the presently used methods.

7. Conclusions and outlook

The field of molecular electronics has rapidly evolved the last 20 years, and is now a highly interdisciplinary endeavour. Still, the long-term starting goal of building computers from molecules seems to be farfetched. As long as the silicon CMOS technology is economically superior the electronics industry will stick to it, and a transition to other technologies seems to be at least 10 years in the future. However, the top-down fabrication methods used for transistors have an inevitable limit of miniaturization when quantum effects become important, and for this molecules can, in principle, provide a more precise spatial control compared to ordinary methods.

In this thesis, we study electron transport in different systems that could be used in molecular electronics devices. To model the electron transport we have used the nonequilibrium Green's function method (NEGF) combined with density functional theory (DFT), which together open the possibility to describe the system *ab initio* or without parameters.

One of the main challenges in molecular electronics is how to control the metal-molecule interface and how to achieve efficient coupling between the electrodes and the molecules. Still, due to variability between different setups, there are no exact values for the conductance of simple molecules, only statistical results are available which could be good enough for fundamental studies but not for applications. Here we study both how these fluctuations affect the measured conductance as well as how the variability between different junctions can be decreased in a nanoelectrode bridge platform. To have a reproducible conductance between different junctions we find that it is necessary to have chemisorbed contacts at both ends of the studied molecule. Another route to minimize the fluctuations in the conductance is to find a more suitable anchor group compared to the thiols which are known to switch stochastically between different bonding sites resulting in large variability in the measured conductance. Here, we propose that one could use silyl-groups (R-SiH$_3$), which coordinate more strongly to gold compared to thiols, thus giving fewer fluctuations in the conductance. Furthermore, due to the σ-bonding of this anchor-group, the resulting conductance when the core of the molecule is σ-conjugated is higher compared to thiols.

Another challenge has been to go "beyond silicon", and to replace the CMOS with a molecular transistor. Simply replacing silicon with molecules that function in the way silicon operates today has more or less turned out to be a dead end, mostly because molecules can do so much more. With molecules come quantum effects and hence functional molecules, such as switches, can

show characteristics even at ambient temperature that common solid-state devices can not. Here we have studied five different families of molecular conductance switches, of which four can be operated by light and/or temperature. By tuning the substituents on the molecules we can obtain high switching ratios for these switches and at the same time keep the distance between the two ends constant, thus, opening up the possibility to use them in devices. The last family of switches are so called mechanoswitches which are activated by a mechanical force elongating the molecules, which could operate as sensors. In general, we find that to have a high switching ratio, the transition from the OFF to the ON-state should induce a shift of the most conducting molecular orbital closer to the Fermi level, and at the same time increase the effective coupling between the electrodes and the orbital. This can be achieved by having a disruption in the π/σ-conjugation in the OFF-state while in the ON-state having a conjugated path spanning the complete molecule.

Furthermore, we have studied two different classes of compounds that may function either as rigid molecular spacers with a well-defined conductance or as molecular cords. In both cases we find that it is of great importance to match the conjugation of the anchoring groups with the molecular backbone for high conductance. For the cage compounds we have a molecular structure with three pathways for conduction and, contrary to what could be expected from Kirchoff's law for conventional electronic devices, we only see an increase in conductance by a factor two when compared to similar molecules with a single conduction pathway. For the proposed molecular cords we find conductance variations in the range of a factor of 50-100, and that the mean conductance is reasonable stable over almost 9 Å of different electrode-electrode distances.

Another interesting semiconductor material that could replace today's technology in certain applications is diamond. In this thesis we had the aim to treat scattering in doped diamond on the nanoscale in a fully *ab initio* way, which turned out to be outside the used methods herewithin. Still, we have accurately calculated the band structure and effective masses for single-crystal diamond. Furthermore, these results have been used, in a semi-classical way, to calculate some important transport properties of boron-doped diamond, such as the Hall coefficient, the resistivity and the Seebeck coefficient.

Acknowledgement

First of all I would like to thank my supervisor Prof. Rajeev Ahuja who made it possible for me to start my PhD studies in the Division of Materials Theory, a truly outstanding research group. Secondly I would like to thank Prof. Jan Isberg, my co-supervisor who has introduced me to the very interesting field of diamond electronics.

I am also most grateful to Anton Grigoriev, who has been my guide through the field of molecular electronics and the methods used here. And also for his help reading and revising manuscripts and this thesis.

Another special thanks goes to Henrik Ottosson, the coordinator of the Uppsala University Unimolecular Electronics Center (U3MEC) for throwing all kinds of interesting projects on me, and the help in reading and revising manuscripts and this thesis. Also I am mostly grateful to Henrik and Rikard Emanuelsson to put up with all my chemistry questions and explaining these concepts for me in a understandable way. Furthermore, I would like to thank my coworkers on the nanoparticle platform project, Klaus Leifer, Jonas Fransson, Hassan Jafri, Tobias Blom, Andreas Wallner, Maria Strømme and Ken Welch. And the coworkers on the switches and wires, Andreas Orthaber, Burkhard Jahn, Alvi Rouf, Rikard Emanuelsson, Sascha Ott, Jun Zhu, Djawed Nauroozi, Judith Baumgartner and Christoph Marschner. Also many thanks to Magnus Paulsson for the introduction and help both using and extending the Inelastica code. And for sharing the first version of the MD+NEGF code, without your help the projects based on the MD simulations would never have seen the daylight. I would also like to thank all other people involved in the U3MEC for interesting discussions during our meetings. And Olle Eriksson the head of the Division of Material Theory and all people working there for making us an outstanding research group, and especially Oscar, Jonas, Peter, Lisa, Anders, Petros, Kristoffer, Annica et. al for all interesting lunch table discussions. Thanks also to the proofreading group, Ross Smith, Henrik Ottosson, Anton Grigoriev and Oscar Grånäs.

Living in Uppsala would not been as pleasant as it has been without all the friends in OK Linné and Upsala IF. Thanks for being the best orienteering club in the world, for all the fun trainings and taking me around the globe to compete and train on the most distant and strange places.

Finally I would like to thank my family, most of all Elin and Algot, for their love and always being there for me.

Svensk sammanfattning

Nanoteknologi har de senaste årtionden vuxit lavinartat och är idag ett av de hetaste vetenskapsområdena. Området i sig är mycket brett och växelverkar ofta med andra områden, t.ex. materialvetenskap och elektronik. Mycket av intresset i nanoteknologi kan härledas till att tillämpningar som bygger på "nano" kan visa upp helt nya egenskaper. Nano syftar på prefixet som betyder 10^{-9} och i det här fallet nanometer (nm), vilken är längdskalan man jobbar med. En nanometer är en miljarddels meter, vilket kan jämföras med t.ex. ett hårstrå som är ca 50 000 nm brett.

När man kommer ner på de här längdskalorna kan ett materials egenskaper ändras drastiskt jämfört med vad vi upplever annars. En metall som leder ström i normala fall kan bli en isolator när den rumsliga utsträckningen krymps i en eller flera riktningar.

De effekter som uppstår när man gör saker mindre kan även förväntas sätta gränsen för hur små elektronikkomponenter man kan bygga med dagens teknik. Om utveckling fortsätter i samma takt som idag kommer man inom några år att nå gränsen för när kvantmekaniken inte tillåter att man krymper komponenterna mer. I en transistor finns en barriär mellan de olika kanalerna och om man fortsätter krympa transistorns storlek kommer barriären till slut att bli så tunn att elektroner kvantmekanisk kan tunnla igenom den vilket gör transistorn obrukbar. Detta är ett rent kvantmekaniskt fenomen som endast uppträder när man kommer ner på atomnivå.

Ett förslag för att kringgå problemet med tunneleffekter i transistorer är att använda molekyler istället. Molekyler är intressanta eftersom de endast består av ett begränsat antal atomer och således är bland de minsta "bygg-klossar" man kan använda. Att använda molekyler som byggklossar i dagens elektronik eller helt ersätta vissa elektroniska komponenter med molekyler har utvecklats till ett delområde inom nanoteknologin som kallas "Molekylär elektronik".

Molekylär elektronik ligger i gränslandet mellan fysik, kemi och materialvetenskap. Detta innebär att det behövs tvärvetenskapliga samarbeten för att lösa de utmaningar som området står inför. Ett av de första problemen man stöter på är att fysikaliskt beskriva hur en ström flyter genom en molekyl. Andra mer ingenjörsmässiga problem som finns är hur man kopplar en makroskopisk mätutrustning till en molekyl som är ungefär 1 nm lång. Till sist handlar det om att kemiskt tillverka molekyler med de önskade egenskaperna, och framförallt hur man optimerar molekylerna för att fungera så bra som möjligt i en makroskopisk mätutrustning.

Den här avhandlingen syftar till att tillföra mer kunskap i de här frågorna genom att modellera transport av elektroner i olika nanosystem. De använda

teoretiska metoderna finns beskrivna i kapitel 2 och bygger på täthetsfunktionalteori tillsammans med greenfunktioner för icke-jämviktssystem, vilka kan beskriva elektrontransport i de här systemen utan parametrar.

I kapitel 3 studerar vi en plattform som kan användas för att mäta elektriska egenskaper hos molekyler. De flesta metoder för att mäta på molekyler, precis som denna plattform, har inneboende problem vad gäller reproducerbarhet. Det beror dels på att det är omöjligt att på atomnivå kontrollera gränsskiktet mellan metallen i elektroderna och molekylerna. Även molekylens exakta utseende mellan de två elektroderna är okänt. Här studerar vi med hjälp av teoretiska metoder hur strömmen varierar beroende på hur gränsskiktet ser ut. För att minska variationerna i mätningar är det fördelaktigt att ha molekyler som binder kemiskt med båda ändarna till de närliggande metallytorna. Nackdelen med att använda sådana molekyler i den här plattformen är att eftersom avståndet mellan elektroderna är ca 30 nm och en molekyl är ca 1 nm, måste man ha flera molekyler ihopkopplade via nanopartiklar av guld för att nå mellan elektroderna. Det skapas då ett komplext nätverk av nanopartiklar och molekyler mellan elektroderna. Här visar vi att även fast vi har ett nätverk av flera molekyler och nanopartiklar så kan vi från experiment gjorda med oelastisk elektrontunnlingsspektroskopi identifiera signaler från enstaka molekyler och på så sätt få information om hut molekylerna sitter i nätverket.

Att bygga aktiva komponenter av molekyler har många fördelar, deras ringa storlek ger inte bara kvantmekaniska effekter som kan användas, t.ex. inom spinntronik (där elektronens spinn istället för laddningen används som informationsbärare), utan de blir även väldigt strömsnåla. I kapitel 4 studerar vi olika typer av molekyler som kan fungera som molekylära strömbrytare, d.v.s. med hjälp av en extern påverkan (elektriska fält, ljus, värme, etc.) kan man antingen slå på eller slå av strömmen som går igenom molekylen. Här studerar vi först molekyler som med hjälp av ljus eller värme kan omstruktureras från en form med sämre ledningsförmåga ("av") till en annan form med bättre ledningsförmåga ("på"), och tillbaka. Denna typ av komponent är viktig om man vill bygga t.ex. minneskretsar med molekyler. För att kunna användas i t.ex. SSD-minnen (från eng. solid state drive) är det viktigt att molekylerna är fasta (solida) d.v.s. inte ändrar längd under själva transformationen. Vi har designat ett antal olika molekyler för dessa tillämpningar och vi visar även att genom att optimera sidogrupperna på molekylen så går det att få en stor skillnad i ledningsförmågan mellan av- och påläge samtidigt som molekylen är statisk under ändringen. Vi studerar även en annan typ av molekyl som ändrar sin ledningsförmåga när man applicerar en kraft och sträcker ut den. Motsatt vad man kan förvänta sig, leder den ström bättre när den blir längre. Dessa mekaniska strömställare skulle kunna användas som känsliga sensorer för längdändringar på nanonivå.

I den makroskopiska världen är elektriska sladdar oumbärliga för det dagliga livet, att hitta motsvarande komponenter inom nanovärlden har visat sig vara svårare. Hittills är det få undersökta molekyler som visar liknande egenskaper,

istället är ledningsförmågan hos de flesta molekylkedjor starkt beroende på om kedjan är böjd eller rak. Så kallade hyperkonjugerade molekyler som består av kedjor ihoplänkade med antigen kisel, germanium eller tenn som vi studerar i kapitel 5 kan visa egenskaper liknande sladdar. Våra resultat visar att det går att rotera delar av molekylkedjan utan att ledningsförmågan ändras mer än faktor 20, vilket i det här fallet är en ganska liten ändring. Vi har även i den här avhandlingen utvecklat en metod för att räkna ut ledningsförmågan som tar hänsyn till molekylens rörelse (molekylär dynamik). Det här ger möjlighet att studera t.ex. hur temperaturen (vibrationer i systemet) påverkar, här kan vi även studera vad som händer om man trycker ihop eller sträcker ut den molekylära "sladden". Förändringen av ledningsförmågan blir större då man trycker ihop eller sträcker ut molekylen, i båda fallen ungefär en faktor 100. Detta är dock fortfarande en liten ändring jämfört med andra liknande molekyler. I kapitlet studerar vi även några andra kiselbaserade molekyler. Dessa är inte flexibla och kan därför inte fungera som sladdar, istället är det låsta i en speciell form och kan därför kanske fungera som elektriska ledare med en väldefinierad ledningsförmåga.

I det sista kapitlet lämnar vi molekylerna och studerar istället diamant, ett material som kan vara intressant som halvledare i tillämpningar under tuffa förhållanden. Förhoppningen var att kunna studera ledningsförmågan av diamant på mikroskopisk nivå med samma metoder som tidigare utvecklats för nanosystemen. Då diamant har ett väldigt stort bandgap d.v.s. skillnad mellan de fyllda elektronbanden och ledningsbanden måste man dopa materialet för att kunna använda det som halvledare. Här har vi har framförallt studerat diamant dopat med bor. Då koncentrationerna av dopning är låg i systemen, måste tusentals atomer användas i modellerna vilket inte ligger inom räckvidden för de metoder vi använt tidigare. Istället har vi beräknat den effektiva massan av laddningsbärarna i diamant, en egenskap som är mycket viktig för ledningsförmågan av materialet. De beräknade effektiva massorna har sedan använts för att beräkna resistiviteten av diamant med olika koncentrationer av bor, samt att uppskatta Hall och termoelektrisk effekt i dessa prov.

80

Bibliography

[1] Transistor Scaling is Innovative Technology for Mobile Devices. `http://www.intel.com/content/www/us/en/silicon-innovations/silicon-technology-leadership-presentation.html`, (accessed 2013-10-03).

[2] Moore, G. E. Progress in digital integrated electronics. *Elec. Dev. Meet., 1975 Int.* **1975**, *21*, 11–13.

[3] Moore, G. E. Cramming more components onto integrated circuits. *Electronics* **1965**, *38*, 114.

[4] Moore's Law Inspires Intel Innovation. `http://www.intel.com/content/www/us/en/silicon-innovations/moores-law-technology.html`, (accessed 2013-10-03).

[5] Kanellos, M. Intel scientists find wall for Moore's Law. `http://news.cnet.com/2100-1008-5112061.html`, 2003; (accessed 2013-10-03).

[6] Moore's Law: "We See No End in Sight," Says Intel's Pat Gelsinger. `http://java.sys-con.com/node/557154`, (accessed 2013-10-03).

[7] Lörtscher, E. Wiring molecules into circuits. *Nat. Nanotechnol.* **2013**, *8*, 381–384.

[8] Heath, J. R.; Ratner, M. A. Molecular electronics. *Phys. Today* **2003**, *56*, 43–49.

[9] Heath, J. R. Molecular Electronics. *Annu. Rev. Mater. Res.* **2009**, *39*, 1–23.

[10] Does molecular electronics compute? [Editorial]. *Nat. Nanotechnol.* **2013**, *8*, 377–377.

[11] Visions for a molecular future. *Nat. Nanotechnol.* **2013**, *8*, 385–389.

[12] Ratner, M. A brief history of molecular electronics. *Nat. Nanotechnol.* **2013**, *8*, 378–381.

[13] Aviram, A.; Ratner, M. A. Molecular rectifiers. *Chem. Phys. Lett.* **1974**, *29*, 277–283.

[14] Reed, M. A. Conductance of a Molecular Junction. *Science* **1997**, *278*, 252–254.

[15] Xue, Y.; Datta, S.; Ratner, M. A. First-principles based matrix Green's function approach to molecular electronic devices: general formalism. *Chem. Phys.* **2002**, *281*, 151–170.

[16] Di Ventra, M. *Electrical Transport in Nanoscale Systems*; Cambridge University Press: Cambridge, 2008.

[17] Akkerman, H. B.; de Boer, B. Electrical conduction through single molecules and self-assembled monolayers. *J. Phys.: Condens. Matter.* **2007**, *20*, 013001.

[18] Dutt, M. V. G.; Childress, L.; Jiang, L.; Togan, E.; Maze, J.; Jelezko, F.; Zibrov, A. S.; Hemmer, P. R.; Lukin, M. D. Quantum Register Based on Individual Electronic and Nuclear Spin Qubits in Diamond. *Science* **2007**, *316*, 1312–1316.

[19] Sanvito, S. Molecular spintronics. *Chem. Soc. Rev.* **2011**, *40*, 3336–3355.

[20] "Valleytronics" - a new type of electronics in diamond. `http://www.uu.se/en/research/news/article/?id=2740&area=2, 10,16&typ=artikel&na=&lang=en`, 2013; (accessed 2013-10-03).

[21] Isberg, J.; Gabrysch, M.; Hammersberg, J.; Majdi, S.; Kovi, K. K.; Twitchen, D. J. Generation, transport and detection of valley-polarized electrons in diamond. *Nat. Mat.* **2013**, *12*, 760–764.

[22] Born, M.; Oppenheimer, R. Zur Quantentheorie der Molekeln. *Annalen der Physik* **1927**, *389*, 457–484.

[23] Hohenberg, P.; Kohn, W. Inhomogeneous electron gas. *Phys. Rev.* **1964**, *136*, B864.

[24] Kohn, W.; Sham, L. J. Self-Consistent Equations Including Exchange and Correlation Effects. *Phys. Rev.* **1965**, *140*, 1133–1138.

[25] Perdew, J. P.; Wang, Y. Accurate and simple analytic representation of the electron-gas correlation energy. *Phys. Rev. B* **1992**, *45*, 13244–13249.

[26] Perdew, J. P.; Burke, K.; Ernzerhof, M. Generalized Gradient Approximation Made Simple. *Phys. Rev. Lett.* **1996**, *77*, 3865–3868.

[27] Soler, J. M.; Artacho, E.; Gale, J. D.; Garcia, A.; Junquera, J.; Ordejon, P.; Sánchez-Portal, D. The SIESTA method for *ab initio* order-*N* materials simulation. *J. Phys.: Condens. Matter* **2002**, *14*, 2745–2779.

[28] Artacho, E. et al. The SIESTA method; developments and applicability. *J. Phys.: Condens. Matter* **2008**, *20*, 064208.

[29] Gonze, X. et al. A brief introduction to the ABINIT software package. *Z. Kristallogr.* **2005**, *220*, 558–562.

[30] Gonze, X. et al. ABINIT: First-principles approach to material and nanosystem properties. *Comput. Phys. Comm.* **2009**, *180*, 2582–2615.

[31] Troullier, N.; Martins, J. L. Efficient pseudopotentials for plane-wave calculations. *Phys. Rev. B* **1991**, *43*, 1993–2006.

[32] Hamann, D. R.; Schlüter, M.; Chiang, C. Norm-conserving pseudopotentials. *Phys. Rev. Lett.* **1979**, *43*, 1494–1497.

[33] Kleinman, L.; Bylander, D. M. Efficacious form for model pseudopotentials. *Phys. Rev. Lett.* **1982**, *48*, 1425–1428.

[34] Junquera, J.; Paz, Ó.; Sánchez-Portal, D.; Artacho, E. Numerical atomic orbitals for linear-scaling calculations. *Phys. Rev. B* **2001**, *64*, 235111.

[35] Anglada, E.; Soler, J. M.; Junquera, J.; Artacho, E. Systematic generation of finite-range atomic basis sets for linear-scaling calculations. *Phys. Rev. B* **2002**, *66*, 205101.

[36] Artacho, E.; Sanchez-Portal, D.; Ordejon, P.; García, A.; Soler, J. M. Linear-Scaling ab-initio Calculations for Large and Complex Systems. *phys. stat. sol. (b)* **1999**, *215*, 809–817.

[37] Baroni, S.; de Gironcoli, S.; Dal Corso, A. Phonons and related crystal properties from density-functional perturbation theory. *Rev. Mod. Phys.* **2001**, *73*, 515–562.

[38] Frederiksen, T.; Paulsson, M.; Brandbyge, M.; Jauho, A. P. Inelastic transport theory from first principles: Methodology and application to nanoscale devices. *Phys. Rev. B* **2007**, *75*, 205413.

[39] Brandbyge, M.; Mozos, J.-L.; Ordejón, P.; Taylor, J.; Stokbro, K. Density-functional method for nonequilibrium electron transport. *Phys. Rev. B* **2002**, *65*, 165401.

[40] Frederiksen, T.; Brandbyge, M.; Lorente, N.; Jauho, A. P. Inelastic Scattering and Local Heating in Atomic Gold Wires. *Phys. Rev. Lett.* **2004**, *93*, 256601.

[41] Frederiksen, T.; Brandbyge, M.; Jauho, A.-P.; Lorente, N. Modeling of Inelastic Transport in One-Dimensional Metallic Atomic Wires. *J. Comput. Elec.* **2004**, *3*, 423–427.

[42] Paulsson, M.; Frederiksen, T.; Brandbyge, M. Phonon scattering in nanoscale systems: lowest order expansion of the current and power expressions. *J. of Phys.: Conf. Ser.* **2006**, *35*, 247.

[43] Paulsson, M.; Frederiksen, T.; Brandbyge, M. Modeling inelastic phonon scattering in atomic-and molecular-wire junctions. *Phys. Rev. B* **2005**, *72*, 201101.

[44] Paulsson, M.; Frederiksen, T.; Brandbyge, M. Inelastic Transport through Molecules: Comparing First-Principles Calculations to Experiments. *Nano Letters* **2006**, *6*, 258–262.

[45] Frederiksen, T.; Lorente, N.; Paulsson, M.; Brandbyge, M. From tunneling to contact: Inelastic signals in an atomic gold junction from first principles. *Phys. Rev. B* **2007**, *75*, 235441.

[46] Venkataraman, L.; Klare, J. E.; Nuckolls, C.; Hybertsen, M. S.; Steigerwald, M. L. Dependence of single-molecule junction conductance on molecular conformation. *Nature* **2006**, *442*, 904–907.

[47] Ulrich, J.; Esrail, D.; Pontius, W.; Venkataraman, L.; Millar, D.; Doerrer, L. H. Variability of Conductance in Molecular Junctions. *J. Phys. Chem. B* **2006**, *110*, 2462–2466.

[48] Andrews, D. Q.; Van Duyne, R. P.; Ratner, M. A. Stochastic Modulation in Molecular Electronic Transport Junctions: Molecular Dynamics Coupled with Charge Transport Calculations. *Nano Lett.* **2008**, *8*, 1120–1126.

[49] Frederiksen, T.; Munuera, C.; Ocal, C.; Brandbyge, M.; Paulsson, M.; Sanchez-Portal, D.; Arnau, A. Exploring the Tilt-Angle Dependence of Electron Tunneling across Molecular Junctions of Self-Assembled Alkanethiols. *ACS Nano* **2009**, *3*, 2073–2080.

[50] Mishchenko, A. et al. Influence of Conformation on Conductance of Biphenyl-Dithiol Single-Molecule Contacts. *Nano Letters* **2010**, *10*, 156–163.

[51] Makk, P.; Visontai, D.; Oroszlány, L.; Manrique, D. Z.; Csonka, S.; Cserti, J.; Lambert, C.; Halbritter, A. Advanced Simulation of Conductance Histograms Validated through Channel-Sensitive Experiments on Indium Nanojunctions. *Phys. Rev. Lett.* **2011**, *107*, 276801.

[52] Pontes, R. B.; Rocha, A. R.; Sanvito, S.; Fazzio, A.; da Silva, A. J. R. *Ab Initio* Calculations of Structural Evolution and Conductance of Benzene-1,4-dithiol on Gold Leads. *ACS Nano* **2011**, *5*, 795–804.

[53] Makk, P.; Tomaszewski, D.; Martinek, J.; Balogh, Z.; Csonka, S.; Wawrzyniak, M.; Frei, M.; Venkataraman, L.; Halbritter, A. Correlation analysis of atomic and single-molecule junction conductance. *ACS Nano* **2012**, *6*, 3411–3423.

[54] Paulsson, M.; Krag, C.; Frederiksen, T.; Brandbyge, M. Conductance of Alkanedithiol Single-Molecule Junctions: A Molecular Dynamics Study. *Nano Lett.* **2009**, *9*, 117–121.

[55] Strange, M.; Rostgaard, C.; Häkkinen, H.; Thygesen, K. S. Self-consistent GW calculations of electronic transport in thiol-and amine-linked molecular junctions. *Phys. Rev. B* **2011**, *83*, 115108.

[56] Toher, C.; Sanvito, S. Efficient atomic self-interaction correction scheme for nonequilibrium quantum transport. *Phys. Rev. Lett.* **2007**, *99*, 056801.

[57] Toher, C.; Filippetti, A.; Sanvito, S.; Burke, K. Self-Interaction Errors in Density-Functional Calculations of Electronic Transport. *Phys. Rev. Lett.* **2005**, *95*, 146402.

[58] Rocha, A. R.; García-suárez, V. M.; Bailey, S. W.; Lambert, C. J.; Ferrer, J.; Sanvito, S. Towards molecular spintronics. *Nat. Mat.* **2005**, *4*, 335–339.

[59] Strange, M.; Kristensen, I. S.; Thygesen, K. S.; Jacobsen, K. W. Benchmark density functional theory calculations for nanoscale conductance. *J. Chem. Phys.* **2008**, *128*, 114714.

[60] Ke, S.-H.; Baranger, H. U.; Yang, W. Electron transport through single conjugated organic molecules: Basis set effects in *ab initio* calculations. *J. Chem. Phys.* **2007**, *127*, 144107.

[61] Herrmann, C.; Solomon, G. C.; Subotnik, J. E.; Mujica, V.; Ratner, M. A. Ghost transmission: How large basis sets can make electron transport calculations worse. *J. Chem. Phys.* **2010**, *132*, 024103.

[62] Xiang, D.; Jeong, H.; Lee, T.; Mayer, D. Mechanically Controllable Break Junctions for Molecular Electronics. *Adv. Mat.* **2013**, *25*, 4845–4867.

[63] Wang, W.; Lee, T. In *Introducing Molecular Electronics*; Cunberti, G., Fagas, G., Richter, K., Eds.; Springer, 2005; p 275.

[64] Smaali, K.; Clément, N.; Patriarche, G.; Vuillaume, D. Conductance statistics from a large array of sub-10 nm molecular junctions. *ACS Nano* **2012**, *6*, 4639–4647.

[65] Li, C.; Pobelov, I.; Wandlowski, T.; Bagrets, A.; Arnold, A.; Evers, F. Charge Transport in Single Au | Alkanedithiol | Au Junctions: Coordination Geometries and Conformational Degrees of Freedom. *J. Am. Chem. Soc.* **2008**, *130*, 318–326.

[66] Kim, Y.; Hellmuth, T. J.; Bürkle, M.; Pauly, F.; Scheer, E. Characteristics of Amine-Ended and Thiol-Ended Alkane Single-Molecule Junctions Revealed by Inelastic Electron Tunneling Spectroscopy. *ACS Nano* **2011**, *5*, 4104–4111.

[67] Sen, A.; Kaun, C.-c. Effect of Electrode Orientations on Charge Transport in Alkanedithiol Single-Molecule Junctions. *ACS Nano* **2010**, *4*, 6404–6408.

[68] Blom, T.; Welch, K.; Strømme, M.; Coronel, E.; Leifer, K. Fabrication and characterization of highly reproducible, high resistance nanogaps made by focused ion beam milling. *Nanotechnol.* **2007**, *18*, 285301.

[69] Binnig, G.; Rohrer, H.; Gerber, C.; Weibel, E. (111) facets as the origin of reconstructed Au (110) surfaces. *Surface Science Letters* **1983**, *131*, L379–L384.

[70] Wallner, A.; Jafri, S. H. M.; Blom, T.; Gogoll, A.; Leifer, K.; Baumgartner, J.; Ottosson, H. Formation and NMR Spectroscopy of ω-Thiol Protected α,ω-Alkanedithiol-Coated Gold Nanoparticles and Their Usage in Molecular

Charge Transport Junctions. *Langmuir* **2011**, *27*, 9057–9067.

[71] Kushmerick, J. G.; Lazorcik, J.; Patterson, C. H.; Shashidhar, R.; Seferos, D. S.; Bazan, G. C. Vibronic Contributions to Charge Transport Across Molecular Junctions. *Nano Lett.* **2004**, *4*, 639–642.

[72] Lambe, J.; Jaklevic, R. Molecular Vibration Spectra by Inelastic Electron Tunneling. *Phys. Rev.* **1968**, *165*, 821–832.

[73] Reed, M. A. Inelastic electron tunneling spectroscopy. *Mater. Today* **2008**, *11*, 46–50.

[74] Dash, L. K.; Ness, H.; Verstraete, M. J.; Godby, R. W. Functionality in single-molecule devices: Model calculations and applications of the inelastic electron tunneling signal in molecular junctions. *J. Chem. Phys.* **2012**, *136*, 064708.

[75] Okabayashi, N.; Konda, Y.; Komeda, T. Inelastic Electron Tunneling Spectroscopy of an Alkanethiol Self-Assembled Monolayer Using Scanning Tunneling Microscopy. *Phys. Rev. Lett.* **2008**, *100*, 217801.

[76] Song, H.; Reed, M. A.; Lee, T. Single Molecule Electronic Devices. *Adv. Mater.* **2011**, *23*, 1583–1608.

[77] van der Molen, S. J.; Liljeroth, P. Charge transport through molecular switches. *J. Phys.: Condens. Matter* **2010**, *22*, 133001.

[78] van der Molen, S. J.; Liao, J.; Kudernac, T.; Agustsson, J. S.; Bernard, L.; Calame, M.; van Wees, B. J.; Feringa, B. L.; Schönenberger, C. Light-Controlled Conductance Switching of Ordered Metal-Molecule-Metal Devices. *Nano Lett.* **2009**, *9*, 76–80.

[79] Liao, J. et al. Cyclic Conductance Switching in Networks of Redox-Active Molecular Junctions. *Nano Lett.* **2010**, *10*, 759–764.

[80] Chen, F.; He, J.; Nuckolls, C.; Roberts, T.; Klare, J. E.; Lindsay, S. A Molecular Switch Based on Potential-Induced Changes of Oxidation State. *Nano Lett.* **2005**, *5*, 503–506.

[81] Bogani, L.; Wernsdorfer, W. Molecular spintronics using single-molecule magnets. *Nat. Mat.* **2008**, *7*, 179–186.

[82] Benesch, C.; Rode, M. F.; Čížek, M.; Härtle, R.; Rubio-Pons, O.; Thoss, M.; Sobolewski, A. L. Switching the Conductance of a Single Molecule by Photoinduced Hydrogen Transfer. *J. Phys. Chem. C* **2009**, *113*, 10315–10318.

[83] Kim, Y. et al. Charge transport characteristics of Diarylethene photoswitching single-molecule junctions. *Nano Lett.* **2012**, *12*, 3736–3742.

[84] Choi, B.-Y.; Kahng, S.-J.; Kim, S.; Kim, H.; Kim, H.; Song, Y.; Ihm, J.; Kuk, Y. Conformational Molecular Switch of the Azobenzene Molecule: A Scanning Tunneling Microscopy Study. *Phys. Rev. Lett.* **2006**, *96*, 156106.

[85] Alemani, M.; Peters, M. V.; Hecht, S.; Rieder, K.-H.; Moresco, F.; Grill, L. Electric Field-Induced Isomerization of Azobenzene by STM. *J. Am. Chem. Soc.* **2006**, *128*, 14446–14447.

[86] Smaali, K.; Lenfant, S.; Karpe, S.; Oçafrain, M.; Blanchard, P.; Deresmes, D.; Godey, S.; Rochefort, A.; Roncali, J.; Vuillaume, D. High On-Off Conductance Switching Ratio in Optically-Driven Self-Assembled Conjugated Molecular Systems. *ACS Nano* **2010**, *4*, 2411–2421.

[87] Kim, Y.; Garcia-Lekue, A.; Sysoiev, D.; Frederiksen, T.; Groth, U.; Scheer, E. Charge Transport in Azobenzene-Based Single-Molecule Junctions. *Phys. Rev.*

Lett. **2012**, *109*, 226801.

[88] Lara-Avila, S.; Danilov, A. V.; Kubatkin, S. E.; Broman, S. L.; Parker, C. R.; Nielsen, M. B. Light-Triggered Conductance Switching in Single-Molecule Dihydroazulene/Vinylheptafulvene Junctions. *J. Phys. Chem. C* **2011**, *115*, 18372–18377.

[89] Fuentes, N.; Martín-Lasanta, A.; Álvarez de Cienfuegos, L.; Ribagorda, M.; Parra, A.; Cuerva, J. M. Organic-based molecular switches for molecular electronics. *Nanoscale* **2011**, *3*, 4003.

[90] Brook, A. G.; Abdesaken, F.; Gutekunst, B.; Gutekunst, G.; Kallury, R. K. A solid silaethene: isolation and characterization. *J. Chem. Soc., Chem. Commun.* **1981**, 191–192.

[91] Brook, A. G.; Nyburg, S. C.; Abdesaken, F.; Gutekunst, B.; Gutekunst, G.; Krishna, R.; Kallury, M. R.; Poon, Y. C.; Chang, Y. M.; Winnie, W. N. Stable solid silaethylenes. *J. Am. Chem. Soc.* **1982**, *104*, 5667–5672.

[92] Eklöf, A. M.; Guliashvili, T.; Ottosson, H. Relation between the π-Contribution to Reversed Si=C Bond Polarization and the Reaction Profile for the Thermolytic Formation of Silenes. *Organometallics* **2008**, *27*, 5203–5211.

[93] Morkin, T. L.; Leigh, W. J. Substituent effects on the reactivity of the silicon-carbon double bond. *Acc. Chem. Res.* **2001**, *34*, 129–136.

[94] West, R. Multiple bonds to silicon: 20 years later. *Polyhedron* **2002**, *21*, 467–472.

[95] Gusel'nikov, L. E. Hetero-π-systems from 2+2 cycloreversions. Part 1. Gusel'nikov–Flowers route to silenes and origination of the chemistry of doubly bonded silicon. *Coord. Chem. Rev.* **2003**, *244*, 149–240.

[96] Ottosson, H. H.; Steel, P. G. Silylenes, silenes, and disilenes: novel silicon-based reagents for organic synthesis? *Chem. - Eur. J.* **2006**, *12*, 1576–1585.

[97] Ottosson, H.; Eklöf, A. M. Silenes: Connectors between classical alkenes and nonclassical heavy alkenes. *Coord. Chem. Rev.* **2008**, *252*, 1287–1314.

[98] Schiessling, J.; Grigoriev, A.; Stener, M.; Kjeldgaard, L.; Balasubramanian, T.; Decleva, P.; Ahuja, R.; Nordgren, J.; Brühwiler, P. A. The Role of Charge-Charge Correlations and Covalent Bonding in the Electronic Structure of Adsorbed C 60: C 60/Al. *J. Phys. Chem. C* **2010**, *114*, 18686–18692.

[99] Solomon, G. C.; Herrmann, C.; Hansen, T.; Mujica, V.; Ratner, M. A. Exploring local currents in molecular junctions. *Nat. Chem.* **2010**, *2*, 223–228.

[100] Odell, A.; Delin, A.; Johansson, B.; Rungger, I.; Sanvito, S. Investigation of the Conducting Properties of a Photoswitching Dithienylethene Molecule. *ACS Nano* **2010**, *4*, 2635–2642.

[101] Hückel, E. *Grundzüge der Theorie Ungesättiger und aromatischer Verbindungen*; Verlag Chemie GmbH: Berlin, 1938.

[102] Baird, N. C. Quantum organic photochemistry. II. Resonance and aromaticity in the lowest 3.pi..pi.* state of cyclic hydrocarbons. *J. Am. Chem. Soc.* **1972**, *94*, 4941–4948.

[103] Ottosson, H. Organic photochemistry: Exciting excited-state aromaticity. *Nat. Chem.* **2012**, *4*, 969–971.

[104] Karadakov, P. B. Aromaticity and Antiaromaticity in the Low-Lying Electronic States of Cyclooctatetraene. *J. Phys. Chem. A* **2008**, *112*, 12707–12713.

[105] Karadakov, P. B. Ground- and Excited-State Aromaticity and Antiaromaticity in Benzene and Cyclobutadiene. *J. Phys. Chem. A* **2008**, *112*, 7303–7309.

[106] Feixas, F.; Vandenbussche, J.; Bultinck, P.; Matito, E.; Solà, M. Electron delocalization and aromaticity in low-lying excited states of archetypal organic compounds. *Phys. Chem. Chem. Phys.* **2011**, *13*, 20690–20703.

[107] Hansen, T.; Solomon, G. C.; Andrews, D. Q.; Ratner, M. A. Interfering pathways in benzene: An analytical treatment. *J. Chem. Phys.* **2009**, *131*, 194704.

[108] Okabayashi, N.; Paulsson, M.; Ueba, H.; Konda, Y.; Komeda, T. Inelastic Tunneling Spectroscopy of Alkanethiol Molecules: High-Resolution Spectroscopy and Theoretical Simulations. *Phys. Rev. Lett.* **2010**, *104*, 077801.

[109] Paulsson, M.; Brandbyge, M. Transmission eigenchannels from nonequilibrium Green's functions. *Phys. Rev. B* **2007**, *76*, 115117.

[110] Beyer, M. K.; Clausen-Schaumann, H. Mechanochemistry: The Mechanical Activation of Covalent Bonds. *Chem. Rev.* **2005**, *105*, 2921–2948.

[111] Caruso, M. M.; Davis, D. A.; Shen, Q.; Odom, S. A.; Sottos, N. R.; White, S. R.; Moore, J. S. Mechanically-Induced Chemical Changes in Polymeric Materials. *Chem. Rev.* **2009**, *109*, 5755–5798.

[112] Hickenboth, C. R.; Moore, J. S.; White, S. R.; Sottos, N. R.; Baudry, J.; Wilson, S. R. Biasing reaction pathways with mechanical force. *Nature* **2007**, *446*, 423–427.

[113] Davis, D. A. et al. Force-induced activation of covalent bonds in mechanoresponsive polymeric materials. *Nature* **2009**, *459*, 68–72.

[114] Dopieralski, P.; Ribas-Arino, J.; Anjukandi, P.; Krupicka, M.; Kiss, J.; Marx, D. The Janus-faced role of external forces in mechanochemical disulfide bond cleavage. *Nat. Chem.* **2013**, *5*, 685–691.

[115] Quek, S. Y.; Kamenetska, M.; Steigerwald, M. L.; Choi, H. J.; Louie, S. G.; Hybertsen, M. S.; Neaton, J. B.; Venkataraman, L. Mechanically controlled binary conductance switching of a single-molecule junction. *Nat. Nanotechnol.* **2009**, *4*, 230–234.

[116] Bruot, C.; Hihath, J.; Tao, N. Mechanically controlled molecular orbital alignment in single molecule junctions. *Nat. Nanotechnol.* **2011**, *7*, 35–40.

[117] Perrin, M. L.; Verzijl, C. J. O.; Martin, C. A.; Shaikh, A. J.; Eelkema, R.; van Esch, J. H.; van Ruitenbeek, J. M.; Thijssen, J. M.; van der Zant, H. S. J.; Dulić, D. Large tunable image-charge effects in single-molecule junctions. *Nat. Nanotechnol.* **2013**, *8*, 282–287.

[118] Miller, R. D.; Michl, J. Polysilane high polymers. *Chem. Rev.* **1989**, *89*, 1359–1410.

[119] Michl, J.; West, R. In *Silicon-Containing Polymers*; Jones, R. G., Ando, W., Chojnowski, J., Eds.; Kluwer Academic Publishers: Dordrecht, 2000.

[120] Hoffmann, R.; Janiak, C.; Kollmar, C. A chemical approach to the orbitals of organic polymers. *Macromolecules* **1991**, *24*, 3725–3746.

[121] Schleyer, P. v. R. Introduction: Delocalization Pi and Sigma. *Chem. Rev.* **2005**, *105*, 3433–3435.

[122] Klausen, R. S.; Widawsky, J. R.; Steigerwald, M. L.; Venkataraman, L.; Nuckolls, C. Conductive Molecular Silicon. *J. Am. Chem. Soc.* **2012**, *134*, 4541–4544.

[123] George, C. B.; Ratner, M. A.; Lambert, J. B. Strong Conductance Variation in Conformationally Constrained Oligosilane Tunnel Junctions. *J. Phys. Chem. A* **2009**, *113*, 3876–3880.

[124] Wallner, A.; Emanuelsson, R.; Baumgartner, J.; Marschner, C.; Ottosson, H. Coupling of Disilane and Trisilane Segments Through Zero, One, Two, and Three Disilanyl Bridges in Cyclic and Bicyclic Saturated Carbosilanes. *Organometallics* **2013**, 130115150934007.

[125] Ernzerhof, M.; Bahmann, H.; Goyer, F.; Zhuang, M.; Rocheleau, P. Electron Transmission through Aromatic Molecules. *J. Chem. Theory. Comput.* **2006**, *2*, 1291–1297.

[126] Grigoriev, A.; Sköldberg, J.; Wendin, G.; Crljen, Ž. Critical roles of metal-molecule contacts in electron transport through molecular-wire junctions. *Phys. Rev. B* **2006**, *74*, 045401.

[127] Reuter, M. G.; Solomon, G. C.; Hansen, T.; Seideman, T.; Ratner, M. A. Understanding and Controlling Crosstalk between Parallel Molecular Wires. *J. Phys. Chem. Lett.* **2011**, *2*, 1667–1671.

[128] Cheng, Z. L.; Skouta, R.; Vazquez, H.; Widawsky, J. R.; Schneebeli, S.; Chen, W.; Hybertsen, M. S.; Breslow, R.; Venkataraman, L. *In situ* formation of highly conducting covalent Au-C contacts for single-molecule junctions. *Nat. Nanotechnol.* **2011**, *6*, 353–357.

[129] Twitchen, D. J.; Whitehead, A. J.; Coe, S. E.; Isberg, J.; Hammersberg, J.; Wikstrom, T.; Johansson, E. High-voltage single-crystal diamond diodes. *IEEE Trans. Electron Dev.* **2004**, *51*, 826–828.

[130] Vescan, A.; Daumiller, I.; Gluche, P.; Ebert, W.; Kohn, E. Very high temperature operation of diamond Schottky diode. *IEEE Electron Dev. Lett.* **1997**, *18*, 556–558.

[131] Sellin, P. J.; Galbiati, A. Performance of a diamond x-ray sensor fabricated with metal-less graphitic contacts. *Appl. Phys. Lett.* **2005**, *87*, 093502.

[132] Gi, R. S.; Mizumasa, T.; Akiba, Y.; Hirose, Y.; Kurosu, T.; Iida, M. Formation Mechanism of p-Type Surface Conductive Layer on Deposited Diamond Films. *Jap. J. of Appl. Phys.* **1995**, *34*, 5550–5555.

[133] Maier, F.; Riedel, M.; Mantel, B.; Ristein, J.; Ley, L. Origin of Surface Conductivity in Diamond. *Phys. Rev. Lett.* **2000**, *85*, 3472–3475.

[134] Balmer, R. et al. Unlocking diamond's potential as an electronic material. *Philos. T. Roy. Soc. A* **2008**, *366*, 251–265.

[135] Willatzen, M.; Cardona, M.; Christensen, N. E. Linear muffin-tin-orbital and k· p calculations of effective masses and band structure of semiconducting diamond. *Phys. Rev. B* **1994**, *50*, 18054–18059.

[136] Hybertsen, M. S.; Louie, S. G. Electron correlation in semiconductors and insulators: Band gaps and quasiparticle energies. *Phys. Rev. B* **1986**, *34*, 5390.

[137] Faleev, S. V.; van Schilfgaarde, M.; Kotani, T. All-Electron Self-Consistent *GW* Approximation: Application to Si, MnO, and NiO. *Phys. Rev. Lett.* **2004**, *93*, 126406.

[138] Bruneval, F.; Vast, N.; Reining, L. Effect of self-consistency on quasiparticles in solids. *Phys. Rev. B* **2006**, *74*, 045102.

[139] Hartwigsen, C.; Goedecker, S.; Hutter, J. Relativistic separable dual-space Gaussian pseudopotentials from H to Rn. *Phys. Rev. B* **1998**, *58*, 3641–3662.

[140] Naka, N.; Fukai, K.; Handa, Y.; Akimoto, I. Direct measurement via cyclotron resonance of the carrier effective masses in pristine diamond. *Phys. Rev. B* **2013**, *88*, 035205.

[141] Isberg, J.; Gabrysch, M.; Majdi, S.; Twitchen, D. J. Negative electron mobility in diamond. *Appl. Phys. Lett.* **2012**, *100*, 172103.

[142] Ashcroft, N. W.; Mermin, D. N. *Solid State Physics*, 1st ed.; Thomson Learning: Toronto, 1976.

[143] Madsen, G. K. H.; Singh, D. J. BoltzTraP. A code for calculating band-structure dependent quantities. *Comput. Phys. Comm.* **2006**, *175*, 67–71.

[144] Pernot, J.; Volpe, P. N.; Omnès, F.; Muret, P.; Mortet, V.; Haenen, K.; Teraji, T. Hall hole mobility in boron-doped homoepitaxial diamond. *Phys. Rev. B* **2010**, *81*, 205203.

[145] Brooks, H. *Advances in Electronics and Electron Physics*; Elsevier, 1955.

[146] Blase, X.; Adessi, C.; Connétable, D. Role of the Dopant in the Superconductivity of Diamond. *Phys. Rev. Lett.* **2004**, *93*, 237004.

[147] Gabrysch, M.; Majdi, S.; Hallén, A.; Linnarsson, M.; Schöner, A.; Twitchen, D.; Isberg, J. Compensation in boron-doped CVD diamond. *phys. stat. sol. (a)* **2008**, *205*, 2190–2194.

Acta Universitatis Upsaliensis

Digital Comprehensive Summaries of Uppsala Dissertations
from the Faculty of Science and Technology 1090

Editor: The Dean of the Faculty of Science and Technology

ACTA
UNIVERSITATIS
UPSALIENSIS
UPPSALA
2013